UC Berkeley

UC Berkeley Electronic Theses and Dissertations

Title

Multi-scale Pull-out Behaviors of Fiber and Steel Reinforcing Bar in Hybrid Fiber Reinforced Concrete

Permalink

https://escholarship.org/uc/item/3cm9847g

Author

Lin, Alexander

Publication Date

2017

Peer reviewed|Thesis/dissertation

Multi-scale Pull-out Behaviors of Fiber and Steel Reinforcing Bar in Hybrid Fiber Reinforced Concrete

By

Alexander Lin

A dissertation submitted in partial satisfaction of the

requirements for the degree of

Doctor of Philosophy

in

Engineering – Civil and Environmental Engineering

in the

Graduate Division

of the

University of California, Berkeley

Committee in charge:

Professor Claudia P. Ostertag, Chair
Professor Paulo J. M. Monteiro
Professor Fai Ma

Fall 2017

Abstract

Multi-scale Pull-out Behaviors of Fiber and Steel Reinforcing Bar in Hybrid Fiber Reinforced
Concrete

by
Alexander Lin

Doctor of Philosophy in Engineering – Civil and Environmental Engineering
University of California, Berkeley
Professor Claudia P. Ostertag, Chair

For a reinforced concrete structural member, sufficient bond between steel reinforcing bar and
concrete guarantees a steel/concrete composite behavior, which is essential for a good overall
member performance. Under severe loading, high slippage between rebar and concrete leads to
matrix cracking and crushing in the bond region followed by degradation of the rebar/matrix
bond. Fiber reinforcement provides a fiber bridging mechanism to resist such cracking behavior
by modifying the tensile properties of the matrix. This thesis investigated a deflection hardening
hybrid fiber reinforced concrete (HyFRC) with micro/macro fiber hybridization and recommends
it as a matrix to enhance the rebar/matrix bond by utilizing its superior crack resisting ability.

In the experimental phase, the rebar bond behaviors in ordinary concrete (OC), HyFRC
without/with high volume fly ash and Engineered Cementitious Composites (ECC), another type
of fiber reinforced cement-based composite (FRCC) with hardening behavior, were studied. The
experimental program consists of monotonic and cyclic rebar pull-out test series and was
supported by digital image correlation (DIC) and vibration test techniques. Different specimens
were made by varying some conditions such as rebar size (no. 4 and no. 8) and absence/presence
of transverse reinforcement (spiral) so the effect of such conditions in regards to bond between
rebar and different matrices can also be studied. In addition to experiments, Finite element
models were developed to further investigate the mechanical behavior of the HyFRC matrix
during rebar pull-out and to examine how a transverse steel reinforcement affects such behavior.

The experimental results showed that HyFRC can improve the rebar pull-out behavior by
changing the failure mode from brittle splitting failure to a more ductile frictional pull-out failure
compared to the OC material. The HyFRC material without fly ash provided better rebar bond
performance compared to OC with spiral reinforcement and other type of FRCC under

investigation. Compared to the monotonic rebar pull-out behavior, only minimal amount of additional damage was induced in such HyFRC material by repeated loading and unloading process from cyclic loading protocol.

DIC measurement indicated that the width of the splitting cracks that form in HyFRC matrices due to rebar pull-out could be further reduced when such specimens were confined by spirals. The finer the splitting cracks, the higher the rebar gripping stress and hence the higher the rebar pull-out resistance. The DIC measurement was consistent with the results from finite element analysis because both of them showed that confining the HyFRC matrix with transverse steel reinforcement led to a more uniform distribution of the splitting crack width during rebar pull-out. The vibration test showed that rebar pull-out induced similar degree of damage in the bond regions of HyFRC with and without transverse reinforcement.

If severe macrofiber pull-out occurs within the cracks induced by rebar pull-out, the macrofibers become less effective in resisting such cracks. Therefore, good macrofiber pull-out resistance in HyFRC is essential for an improved rebar pull-out performance. To investigate the macrofiber pull-out behavior and how it is affected by the presence of PVA microfibers in HyFRC, single fiber pull-out tests were conducted for various mortar mixtures. In some of these mortars, the cement was replaced by industrial by-products, such as fly ash and slag. In addition, macrofiber pull-out behavior in an ultra-high strength concrete with and without steel microfiber reinforcement was also studied.

The results of the single fiber pull-out tests revealed that the presence of PVA microfibers in a mortar mixture designed based on the HyFRC mixture enhances the steel macrofiber pull-out resistance. This synergy between micro and macrofibers provided a more effective control of the splitting cracks and was responsible for the superior rebar bond performance. Hence, the research revealed a multi-scale bond enhancement in a HyFRC member reinforced by steel rebar. The macrofiber pull-out behaviors from mortars in which 45% and 15% of cement were replaced by slag and fly ash, respectively, showed that slag densified the steel macrofiber/matrix interface and hence, improved the pull-out resistance for the macrofiber. On the other hand, test results of fiber pull-out specimens in which 55% of cement was replaced by fly ash showed that increasing curing age made the PVA microfiber reinforcement less effective in resisting steel macrofiber pull-out. Such characteristic showed how high-volume fly ash weakened the PVA fiber/matrix bond. This mechanism induced by fly ash made PVA fibers in HyFRC less effective in improving steel macrofiber pull-out resistance and hence, reduced the micro/macro fiber synergy, which is beneficial for the rebar bond behavior. Therefore, using high volume fly ash decreased the rebar

pull-out resistance in HyFRC. When steel macrofibers were pulled out from extremely strong matrices, almost no microcracks formed around macrofibers and the steel microfiber reinforcement didn't affect the macrofiber pull-out behavior because such microfibers function by bridging the microcracks.

Contents

List of figures

List of tables

Acknowledgements

1   Introduction

The bond behavior between reinforcing bars and concrete matrix plays an important role in allowing steel/concrete composite behavior, which is essential for good performance of reinforced concrete structures. A superior rebar/matrix bond behavior provides an additional safeguard for human life by enhancing ductility/toughness and preventing abrupt failure of structural member under severe loading such as earthquake loading.

In conventional reinforced concrete structures, transverse reinforcements such as spirals and stirrups confine the longitudinal reinforcement to guarantee sufficient bond behavior between longitudinal rebar and concrete. Fiber reinforcement provides another way to enhance the rebar/matrix bond by modifying the matrix tensile properties. In conventional fiber reinforced concrete (FRC), the fibers enhanced the softening behavior of the matrix after cracking and hence, improved the rebar bond performance. On the other hand, a high-performance fiber reinforced cement-based composite (HPFRCC), which exhibits strain/deflection hardening behavior rather than softening behavior exhibited by conventional FRC, improves the rebar pull-out behavior in a more significant manner. When bond failure occurs via splitting cracks, the fibers in HPFRCC bridge such cracks, providing load transfers across the cracks and maintaining the integrity of the matrix. Such a mechanism redistributes the stresses from cracked regions to uncracked regions and leads to more homogeneous damage in the matrix rather than a localized one. Crack opening processes lead to energy dissipations from fiber pull-out, which enhance the ductility of bond failure.

In the literature, experiments were conducted to investigate the rebar bond behaviors in cementitious matrices and study how such behavior affect the rebar/matrix composite behavior. Tension tests (also called tension stiffening tests) were conducted for cementitious prism matrices reinforced by longitudinal rebars to investigate how local rebar/matrix bond interaction and cracking behavior of matrix affect the overall performance of such composite specimens [1-6]. The bond interactions between rebars and matrices were investigated by rebar pull-out tests for plain concrete/mortar matrices without and with various amounts of transverse steel reinforcement [7-20]. Rebar pull-out tests were also performed for fiber reinforced cement-based composite (FRCC) matrices [21-32] but not yet for high performance hybrid fiber reinforced concrete (HyFRC) which was developed at the University of California, Berkeley (UC Berkeley) by utilizing micro/macro fiber hybridization. In order to develop guidelines for modeling and designing HyFRC structure reinforced with mild steel, a rebar pull-out test program was carried

out in this thesis and the rebar bond performance in HyFRC was investigated. The experimental program was supported by digital image correlation (DIC) and vibration test techniques.

In this thesis, single fiber pull-out tests were also performed to investigate the macrofiber bond behaviors and how such bond performances are improved by microfibers. Such investigation for the mechanical behavior of the fiber reinforced matrix is essential to understand the rebar bond mechanism in HyFRC. In the literature, single fiber pull-out test is commonly used to study the bond behavior between fiber and cementitious matrix around it [33-36].

Fly ash and slag, which are by-products from the industry, can be used as supplementary materials to replace cement to decrease the environmental impact of a concrete mixture [37]. Such type of replacement was applied to some mixtures used for rebar pull-out and fiber pull-out specimens. The HyFRC specimens for rebar pull-out tests were made without and with high volume fly ash replacement. The rebar bond behavior in the HyFRC without fly ash is the main research topic in this report and the HyFRC with fly ash is used as a comparison to study the effect of fly ash. For convenience, the term HyFRC represents the HyFRC material without fly ash in the following text unless otherwise specified.

In addition to the experimental programs mentioned above, finite element (FE) models were developed for further studying the rebar bond behavior in HyFRC and the effect of transverse steel reinforcement in such behavior. The analysis results from the model show how the HyFRC matrices in the rebar bond regions behave during rebar pull-out.

The results of rebar/matrix bond experiments are presented in Chapter 2. The effects of different parameters (such as matrix material, rebar size, absence/presence of transverse steel spiral reinforcement, monotonic/cyclic loading protocol) to rebar bond behavior were investigated by conventional rebar pull-out test without DIC. The rebar bond behaviors within unconfined and spiral-confined HyFRC were further investigated by applying DIC measurement to modified rebar pull-out tests and performing vibration tests. During rebar pull-out, the DIC continuously monitored the strain and crack development on matrix surface. On the other hand, vibration test indicated the degree of bond damage around the rebar embedment region inside the matrix.

Chapter 3 presents the results of single fiber pull-out tests, which were performed by pulling out a hooked end steel macrofiber from a cementitious matrix with and without microfiber reinforcement. The results not only strongly correlated to the rebar pull-out behavior in HyFRC observed in Chapter 2 but also indicated the effect of matrix compositions, fiber contents and

curing ages in regards to the bond behavior of macrofiber and effectiveness of microfiber reinforcement.

The finite element analysis (FEA) results for the simulation of rebar bond behaviors in HyFRC with/without transverse steel reinforcement are presented in Chapter 4. The FE model utilized line interface elements with cohesive crack law to simulate the behavior of splitting cracks bridged by fibers. The FEA results are compared with the results from rebar/HyFRC bond experiments and support the observation based on such experimental program.

Chapter 5 summarizes the results presented in this thesis and provides concluding remarks. The results indicated that HyFRC can be used in structural members where rebar bond performance is more critical. The rebar pull-out test results provide guidelines for developing building code for various HPFRCC materials. Some suggestions were made for future research related to the study in this thesis.

1.1 Hybrid fiber reinforced concrete (HyFRC)

A HyFRC was developed at UC Berkeley with performance based optimization of micro polyvinyl alcohol (PVA) and macro hook end steel fiber proportions [38]. A superior crack resisting ability was provided by a multiscale fiber bridging behavior from micro and macro fibers. Therefore, deflection hardening was achieved in the HyFRC with a lower fiber volume fraction (1.5%) [38] compared to the typical fiber dosages (higher than 2%) to guarantee a hardening behavior in a HPFRCC utilizing single type of fibers. The low fiber content in HyFRC leads to a good workability for construction practice. With the deflection hardening behavior, the HyFRC matrix exhibits superior tensile capacity and toughness. Such characteristics for HyFRC provide a viable way to improve the performance of a reinforced concrete structure.

In a broad sense, HyFRC is categorized as a high-performance fiber reinforced cement-based composite (HPFRCC). As Figure 1 indicates, the strain and deflection hardening behavior of the HPFRCC make such a material different from a conventional fiber reinforced concrete (FRC), which exhibits strain and deflection softening behaviors [39].

In the stress-strain curve plot, σ_{cc} is the cracking stress corresponding to first crack formation in a specimen under uniaxial tension. Once the first crack forms at such stress level in a conventional fiber reinforced concrete (FRC), the fiber pull-out occurs at the crack region

because the stress carrying capacities of the fibers are lower than σ_{cc}. In this case, the localized crack keeps widening and strain-softening behavior occurs simultaneously. On the other hand, the stress capacities from fiber bridging that are higher than σ_{cc} can be achieved in HPFRCC by incorporating a higher fiber dosage or modifying the fiber geometries and/or mechanical properties. Once the first crack forms in HPFRCC at σ_{cc}, the fibers at the crack carry the full tensile load without being pulled out considerably. Such characteristic leads to strain hardening behavior accompanied by multiple tensile crack formations from σ_{cc} to maximum post cracking stress (σ_{pc}) corresponding to significant fiber pull-out in one dominant crack.
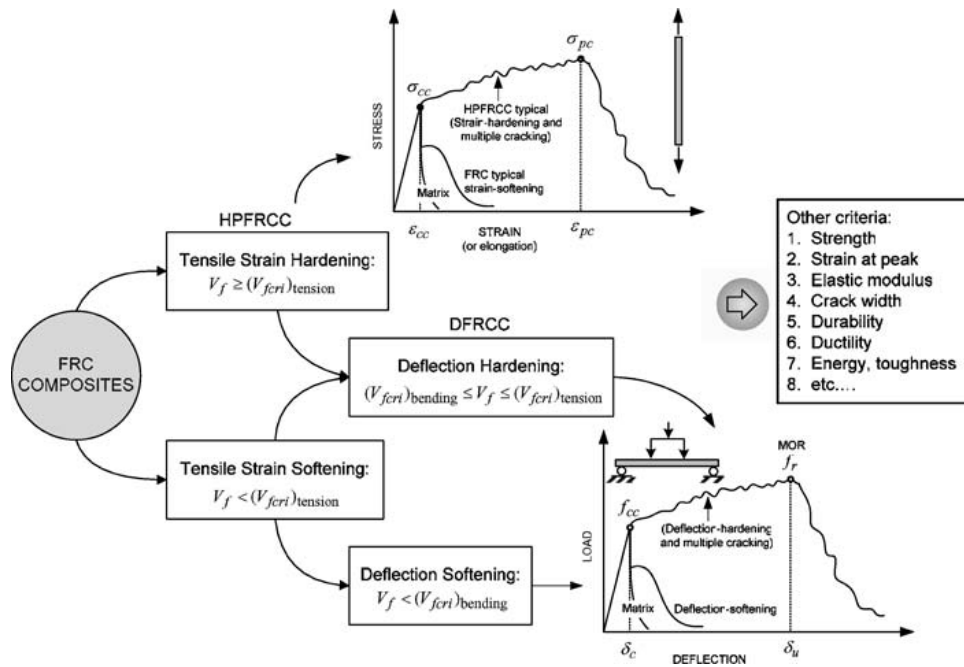
Figure 1: Classification for FRC and HPFRCC [39]

With an optimized micro/macro fiber proportion, hardening behavior can be achieved by HyFRC with lower fiber content, compared to other types of HPFRCC with single types of fibers. Such a characteristic can be explained by a multi-scale crack control mechanism in HyFRC. In this case, the PVA fibers resist the micro cracks at the crack initiation phase, and after the cracks develop and become wider, the macro steel fibers bridge the macro cracks. In addition, a micro/macro fiber synergy mechanism in HyFRC makes the macro fiber bridging more effective because the bond resistance of the macro fiber is improved by the micro fiber reinforced matrix [40]. In the literature, a similar fiber synergy between micro and macro steel fibers was confirmed by single fiber pull-out tests [33]. The authors observed micro cracks in the matrix surrounding the steel macrofiber induced by macrofiber pull-out as shown in Figure 2. They claimed that the steel microfibers improved the matrix/macrofiber bond by resisting such cracks.
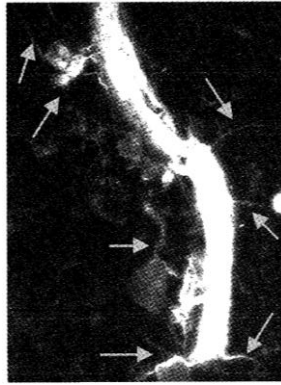
Figure 2: Micro crack induced by macro steel fiber pull-out [33]

1.2 Different rebar bond behavior under various reinforcement condition

To understand the importance of rebar bond improvement provided by the high-performance HyFRC, it is essential to be familiar with rebar pull-out behaviors in cementitious materials without and with different types of reinforcement. Herein, a review of the rebar bond mechanism in OC will be provided and the effect of using transverse reinforcements and conventional FRC matrices will be introduced. Then, the rebar bond behavior in HPFRCC will be discussed and compared with other types of reinforcements.

1.2.1 Rebar bond mechanism for ordinary concrete without/with transverse reinforcement

The bond behavior between concrete and embedded steel rebar determines if sufficient steel/concrete composite behavior occurs in a reinforced concrete member. When a rebar is under tension, the surrounding matrix needs to provide sufficient bond resistance to prevent the rebar from being pulled out of the matrix. In this case, the rebar/matrix bond performances under different reinforcement conditions can be evaluated by rebar pull-out tests. A typical specimen geometry and a set-up for such tests were provided by Eligehausen et al. as shown in Figure 3 [10]. The specimen, which consists of a longitudinal rebar encased in a cementitious matrix, was embedded in an apparatus to pull-out the rebar. The bond stress (τ) around the rebar can be calculated from the measured load and the relative rebar slippage (s) was measured by linear variable differential transformers (LVDT). A typical way to visualize the bond performance is by plotting a bond stress-rebar slippage (τ-s) curve as shown in Figure 4. Herein, the bond mechanism corresponding to such a curve will be introduced according to the explanation provided by Eligehausen et al. [10]. During rebar pull-out, rebar slippage is mainly caused by

5

crushing and shearing of matrix in front of rebar ribs. At point A in the figure, the rebar/concrete adhesive bond is broken. Further pull-out resistance is provided by the inclined bearing force from rebar ribs/matrix interlock as shown in Figure 5. In addition, the friction at rebar/concrete interface provides another important source of bond resistance. After the bond stress reaches point B, intense inclined bearing forces lead to inclined bond cracks which correspond to the nonlinearity after point B. Such crack was observed in Goto's experiment [1].
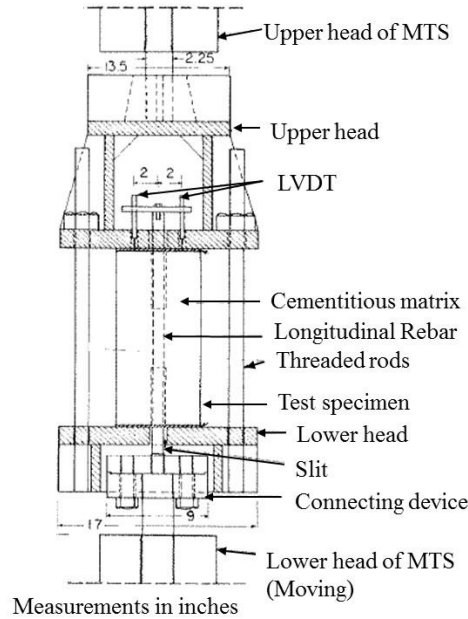
Figure 3: Typical rebar pull-out test set-up [10]
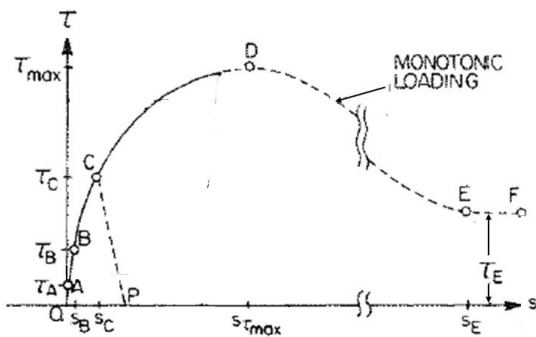
Figure 4: Typical relationship between bond stress (τ) and slip (s) for rebar pull-out [10]
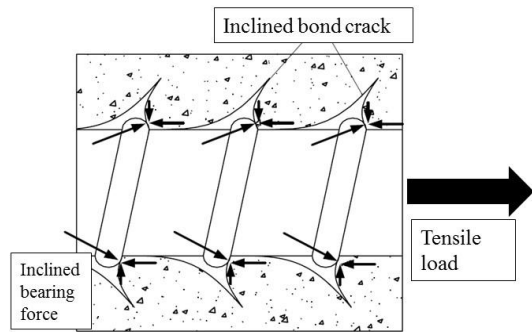
Figure 5: Interlock mechanism between rebar ribs and concrete [1]

When the bond stress develops, the radial component of inclined bearing force leads to ring tension stress field in the matrix around the rebar as shown in Figure 6 [41-43]. At point C of the bond stress-rebar slippage curve in Figure 4, such tension ring is intense enough to crack the matrix in radial directions. If there is no transverse reinforcement for the concrete, the radial splitting cracks propagate outward from rebar/matrix interface, become fully developed and lead to rebar/matrix detachment as shown in Figure 7. In this case, the bond stress is completely lost after such a splitting failure so the curve in Figure 4 drops from point C to point P immediately. On the other hand, if transverse reinforcement such as steel spiral is present, it resists the opening of the splitting crack by clamping the matrix as shown in Figure 8. With maintained matrix integrity, the bond resistance from the surrounding matrix allows the bond stress to increase further and leads to ascending branch from point C to D. Approaching point D, further non-linearity of the curve is caused by widening of restrained splitting cracks and initiation of shear cracks in the concrete keys between the rebar ribs. After point D, more and more concrete between the ribs are affected by such shear failures. Simultaneously, the rebar and concrete keys between rebar ribs were slipped out against the exterior matrix. The concrete keys are completely sheared off at point E and the remained bond resistance is provided by the mechanical interlock and frictional resistance from the exterior matrix. Such a failure mode is referred as frictional pull-out, which leads to a higher peak bond stress and afterwards, provides a ductile softening branch from point D to F rather than losing bond resistance completely.
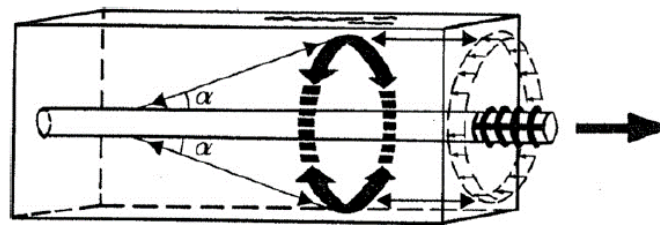
Figure 6: Tension ring stress field induced by radial components of rebar rib bearing force during rebar pull-out [41, 42]
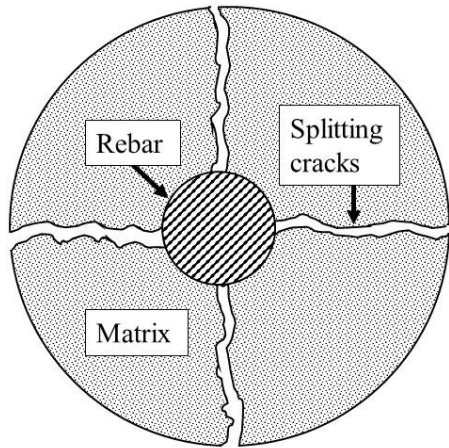
Figure 7: Splitting failure for unconfined ordinary concrete
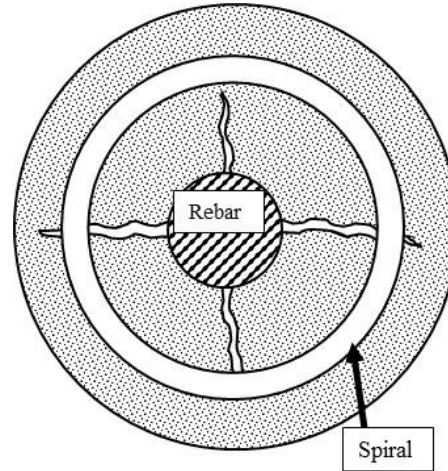
Figure 8: Frictional pull-out failure for spiral confined ordinary concrete

1.2.2   Rebar bond behavior for conventional fiber reinforced concrete (FRC) composite

Rebar pull-out experiments were conducted for conventional FRC composite (reinforced by polypropylene or steel fibers) which exhibit strain and deflection softening behavior [21-23]. According to the rebar bond behavior in conventional FRC matrix and their control matrix without fiber reinforcement, the bond strengths and failure modes are independent to absence/presence of fiber reinforcement and only depend on the matrix strengths and specimen dimensions such as rebar sizes and concrete cover thickness. Figure 9 and 10 show different bond stress-slippage curves for matrices with/without fiber reinforcements under splitting failures and frictional pull-outs respectively. When splitting failure occurs, the fiber reinforcement in the FRC with softening behavior is not able to overcome the cracking stress at the splitting cracks so the fibers are pulled out and the crack becomes fully developed. In this case, the FRC matrix is not able to improve the peak bond stress by preventing the splitting failure and only provides higher post-peak bond resistance, which leads to a smoother softening branch, by delaying the matrix/rebar detachment. The conventional FRC is less effective compared to conventional transverse reinforcement in regards to improving rebar bond performance.

Occurrence of frictional pull-out failure mode can be guaranteed by appropriate specimen dimension parameters, such as a high ratio between concrete cover and rebar diameter. In this case, FRC specimen shows identical bond stress-rebar slippage curve as OC. The fiber reinforcement doesn't make a difference because the concrete sheared and crushed by rebar ribs

8

is too close to the rebar to provide enough space for fibers to develop enough embedment strength at the rebar side of a crack.
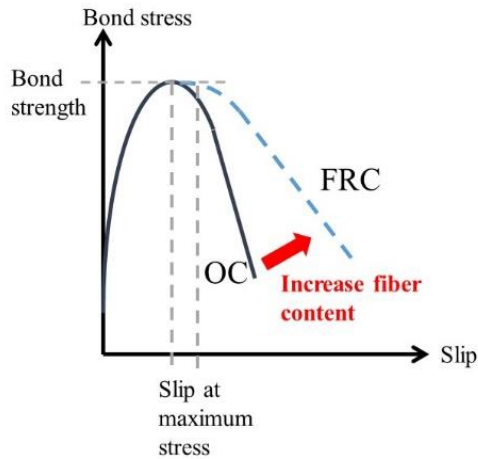
Figure 9: Bond stress-slippage curves for OC and conventional FRC with splitting failure
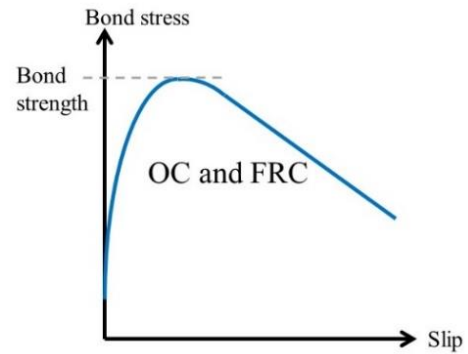
Figure 10: Bond stress-slippage curves for OC and conventional FRC with frictional pull-out

1.2.3 Rebar bond behavior for high performance fiber reinforced cement-based composite (HPFRCC)

Rebar bond test for strain/deflection hardened HPFRCC were performed to test if such a material improves the rebar pull-out performance in a more significant manner compared to a conventional FRC. In [26, 27], a series of rebar pull-out tests was performed to compare the rebar bond behavior in HPFRCC and OC without/with spiral reinforcement. The authors observed that by using a HPFRCC matrix instead of OC the failure mode changes from splitting to frictional pull-out. Such an improvement only exists in HPFRCC but not in conventional FRC because the HPFRCC provides a more effective fiber bridging mechanism at the splitting crack induced by rebar slippage.

Instead of having severe fiber pull-outs accompanied by stress relaxation within a splitting crack, the fibers in HPFRCC develop firm anchorages in the matrix and during crack opening, the continuously increased stressing and stretching of fibers lead to a hardening behavior at a cracked region. Such a hardening behavior resists splitting crack to open so rebar/matrix detachment is prevented. In this case, the specimen keeps providing bond stresses higher than the stress corresponding to splitting failure. With crushing and shearing off the concrete keys between rebar ribs, frictional pull-out occurs to HPFRCC in a similar manner as that for previous

confined OC case and leads to peak/residual bond stress increments compared to a splitting failure.

In [26], the rebar pull-out behavior in unconfined OC is compared with SIFCON, a HPFRCC with 9.6% volume fraction of steel fiber. The SIFCON matrix significantly improves the peak and post-peak bond stresses for rebar. By modifying the mechanical and geometrical properties of fibers, other types of HPFRCCs which also exhibit hardening behavior can be made with fiber volume fractions as low as 2% and such HPFRCCs improve the bond behavior in similar manner but with different degree compared to SIFCON [27]. Enhancement of bond strength and rebar pull-out ductility in HPFRCC were also observed by Krstulovic-Opara et al. [25] who performed rebar pull-out test for OC, conventional FRC and HPFRCC. The enhancement is generally attributed to matrix tensile strength but using HPFRCC leads to disproportionally higher bond strength increment relative to a tensile strength increment due to strain hardening behavior of such a material [25].

1.3   Supplementary techniques for investigation of bond behavior

1.3.1   Digital image correlation (DIC) techniques

The rebar pull-out test program was supported by the digital image correlation (DIC) techniques. Such experimental techniques measure the in-plane deformations of a specimen surface accurately by tracking registered points on such a surface. Compared to the measurements at discrete points from conventional extensometer and strain gauge techniques for mechanical testing, more detailed information is provided by continuous displacement and strain maps in a surface range measured by the DIC techniques at different loading stages. In addition to such a benefit, the relatively low facility requirements for conducting DIC techniques make such techniques widely used in mechanical testing of solid materials [44]. In the literature, the mechanical behaviors for rebar/concrete interface [45] and fiber reinforced concrete [46] were successfully investigated by DIC. In [47], the authors utilized DIC to capture the slippage within rebar/matrix interface and the crack characteristic during tensile testing for concrete and Engineered Cementitious Composites (ECC) specimens reinforced by different types of reinforcing bars.

A typical way to apply DIC techniques to a mechanical test is shown in Figure 11. Before and during load application towards the specimen, a camera is used to take pictures repeatedly against a region of interest (ROI), a range of specimen surface with random speckle pattern. On the reference image taken before loading, a DIC software registers the rectangular reference subsets located at the intersections of the virtual mesh in Figure 12. Figure 13 shows an example for a reference subset. The unique speckle pattern of such a subset differentiates itself from other subsets and same subset can be identify again by the speckle pattern on the deformed images, images for deformed surface after load application. By comparing the registered subsets in reference and deformed images, the rigid body motion and deformation of each subsets are calculated by DIC software and hence, displacement and strain field on ROI are available. [44]
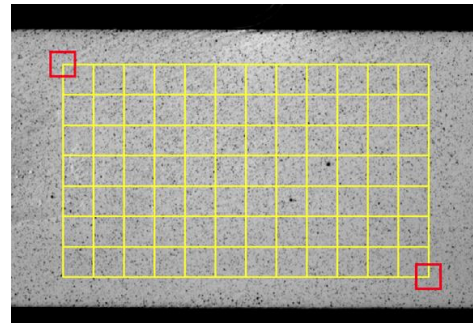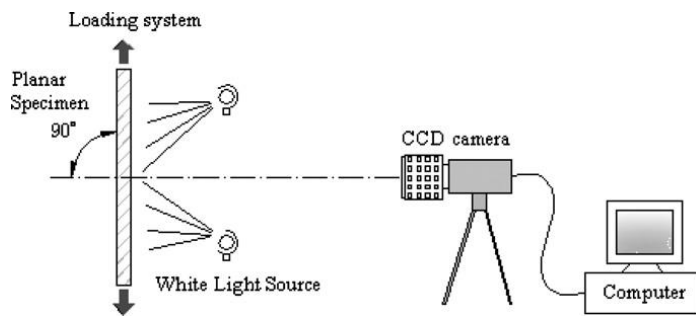
Figure 11: Typical optical image capture system for DIC techniques [44]

Figure 12: Reference image for DIC measurements [44]
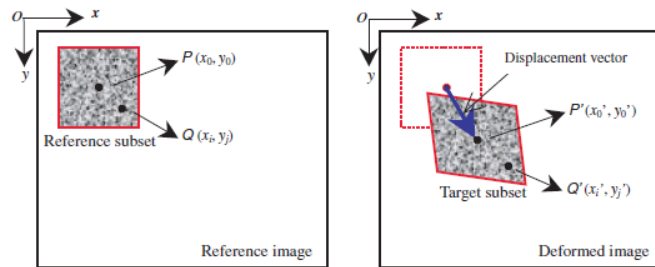
Figure 13: Schematic illustration for tracking registered subset and obtaining subset displacement/deformation [44]

1.3.2 Vibration tests

Different to the DIC techniques, which is applied on material surface, vibration tests provide information for the bond region inside the specimen. In the literature, the vibration test was

applied to rock bolt to monitor its bond condition with the rock matrix. In a common manner, the bond damaged can be detect by measuring the natural frequencies from rock bolt vibration induced by a hammer or an impact device. A decrement of the natural frequency indicates a system stiffness decrement induced by bolt/matrix debonding [48, 49] and longitudinal cracks in the material surrounding the rock bolts [50]. In addition, the vibration may also be affected by pre-stress applied to rock bolt because the pre-stress closes the micro cracks in the material around the bolt and hence, leads to stiffness increment of the system accompanied by natural frequency increment [51]. To sum up, the vibration tests provide information about bond damage and stress state in the bond region for a rock bolt system. Such a characteristic is a motivation to further investigate the bond region for rebar pull-out specimen with vibration test.

1.4   Computational simulation for rebar bond behavior

In the literature, 2-dimensional Finite Element (FE) model were developed to simulate the rebar bond behavior in concrete [52]. On the other hand, the bond stress-slippage law between FRC matrix and ribbed GFRP (glass fiber reinforced polymer) bar in 2-dimension FE model was calibrated by comparing results from simulations and experiments [53].

3-dimensional models for Finite Element Analysis (FEA) were also commonly used to investigate the rebar pull-out behaviors in different type of concrete matrices. In [54, 55], steel rebar was represented by truss elements and concrete matrix were simulated by 3-dimensional solid elements utilizing microplane model [56]. The bond interaction between matrix and rebar was induced by discrete bond elements, in which relation between bond stress and relative displacement in the direction parallel to rebar is assigned. The effect of normal stress between rebar and concrete is considered in the formulation for such relation.

On the other hand, the rebar pull-out model developed in [57, 58] utilizes 3-dimensional solid elements to represent both concrete matrix and rebar. Interface elements were created at the surface between concrete and rebar elements. Relations between stresses and relative displacements in the directions parallel and perpendicular to the rebar is assigned to such interface elements to simulate the rebar/concrete bond behavior.

The bond interaction between rebar and concrete matrix was approached differently in the model developed in [59]. Instead of interface elements, kinematic relation between the nodes on rebar and concrete elements induced the bond interaction. Figure 14 described how concrete and rebar

slip against each other when the rebar is pulled out from the concrete matrix. The thick solid line represents the rebar surface around a rebar rib. Before rebar pull-out, the concrete surface at the rebar/matrix interface is represented by the dashed line and is fully attached to the rebar surface as shown in the figure. At this stage, point C, which is located on concrete, contacts point S, which is on rebar surface. After pulling out the rebar along the Z-axis with u_{Sz} of displacement, concrete at point C is forced to slip against the inclined surface of rebar rib and moves to a new location, point C', accompanying by u_{Cr} of radial displacement of the concrete matrix. The relation between u_{Sz} and u_{Cr} is highly dominated by the inclination of the rib surface which point S locates on. The crushed concrete attached to the rib surface also affects such kinematic relation but this factor is ignored by the authors to simplify the model.

The model developed in [59] utilize a fictitious crack model [37], which is a subset of cohesive crack model, to simulate the tensile behavior within cracked region. The fictitious crack model simulates the fracture process zone on the crack as a region with fictitious crack closure stress, and has a cohesive crack law defining the relation between such crack closure stress and crack width. The crack closure stress-crack width relation is ideal for representing the tensile softening behavior of crack regions in a plain concrete and simulating the crack closure stress induced by fibers across cracks in FRC.
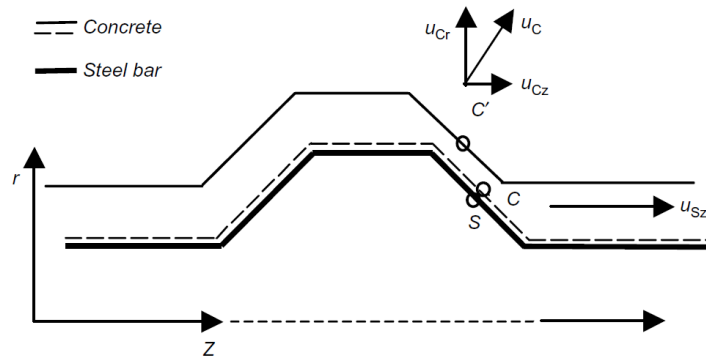
Figure 14: Kinematic relation between concrete matrix and rebar at the interface between them [59]

In [59], the main splitting crack faces were simulated with interface elements. After tensile strength is achieved in the interface elements, such elements exhibit a tensile softening behavior following the cohesive crack law. To simulate the rebar pull-out behavior in both plain concrete and FRC matrices, different cohesive crack laws corresponding to these matrix materials were applied to the model.

2   Experimental investigation of rebar bond behavior in HyFRC

2.1   Introduction

In this chapter, rebar bond behavior in HyFRC is investigated by an extensive rebar pull-out test program. Some of the pull-out tests were also supported by DIC and vibration tests. The combination of PVA microfibers and hooked-end steel macrofibers in HyFRC is expected to provide a multi-scale crack bridging mechanism, which provides sufficient crack closure stress to resist the splitting cracks induced by rebar pull-out (as shown in Figure 15) despite HyFRC's relatively low fiber volume fraction. The crack closure stress in HyFRC leads to normal stress gripping the rebar and matrix around it. Similarly, spiral reinforcement also leads to crack closure stresses and hence the formation of normal stresses that act against the rebar as shown schematically in Figure   16. However, in this case the closure stresses are mainly activated in close vicinity of the spiral. The desirable failure mode is frictional pull-out rather than the brittle splitting failure, which is often observed in concrete matrices without transverse reinforcements.
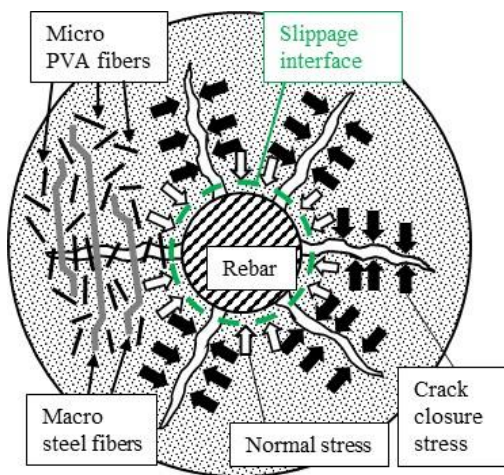
Figure 15: Bond mechanism in HyFRC
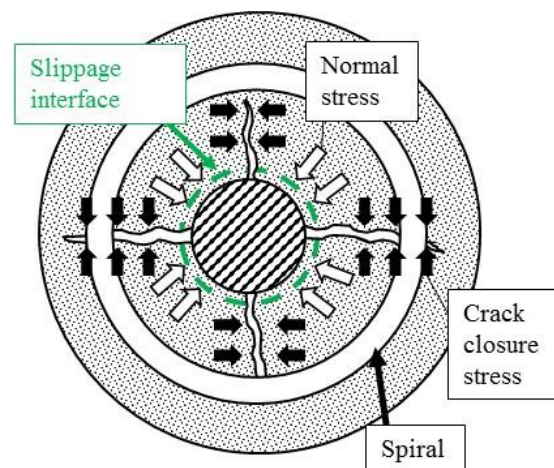
Figure   16: Bond mechanism for ordinary concrete confined by transverse reinforcement

Figure 17 provides a schematic example for frictional pull-out failure from side view of the rebar. Such failure occurs when shear cracks in the matrix keys between rebar ribs become dominant (section 1.2.1). Afterwards, the rebar and matrix between rebar ribs slips out against the exterior matrix and hence a slippage interface forms as shown by the dashed line in Figures 15-17. In this case, both peak and post-peak bond resistance depends on the interlocking/friction resistance at

rebar/matrix interface, shear crack/crushing resistance of concrete keys between rebar ribs and the effectiveness of reinforcement in regards to resisting splitting cracks. A more effective reinforcement leads to higher normal stress gripping/confining the rebar and matrix around it. Intense gripping behavior increases the rebar rib/matrix bearing force and the frictional force at rebar/concrete interface so higher peak and post-peak bond stress occurs. The intensity of the rebar gripping/confining behavior in HyFRC and other types of HPFRCCs is controlled by mechanical properties of the matrices such as elastic modulus, stress level for cracking and degree of hardening behavior within cracks.
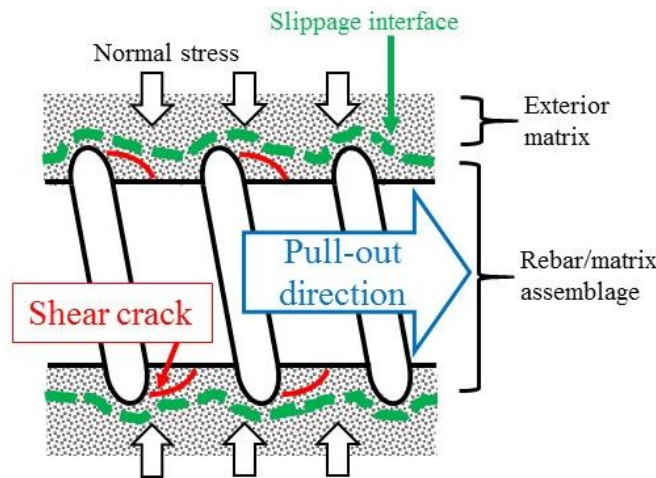
Figure 17: Bond mechanism for frictional pull-out failure mode

2.2 Conventional rebar pull-out test series with various parameters

2.2.1 Introduction

Conventional rebar pull-out test series were conducted to investigate the rebar bond behavior when a concrete matrix is replaced by HyFRC. Control and HyFRC specimens were fabricated with and without fly ash, two different rebar sizes (No. 4 and No.8), and with and without spiral reinforcements.

As mentioned in Chapter 1, replacing cement with fly ash reduces the environmental impact of concrete. The pozzolanic reaction from fly ash can densify the steel fiber/concrete interface and hence, leads to superior mechanical behavior of a FRC matrix [60]. Similarly, fly ash may also densify the interface between steel rebar and concrete to provide a better rebar bond behavior. To

investigate the above beneficial effects of fly ash, rebar pull-out specimens of HyFRC and its control matrix without fibers were made with high volume fly ash replacements.

In addition, rebar pull-out tests were performed for the specimens made by Engineered Cementitious Composites (ECC). Such a material is a mortar-based HPFRCC utilizing significant micro fiber bridging for ultra-high ductility and showed to provide superior load capacity and energy absorption in structural elements [61]. The uniaxial tensile responses reported in [6] with set-up showed in [62] indicate that ECC exhibit higher strength and more significant hardening behavior compared to HyFRC because of the lower w/c ratio and higher fiber content for ECC. The tensile characteristics, matrix compositions (mortar v.s. concrete), and type and volume fractions of fibers are the main differences between ECC and HyFRC. The combination effect of above differences in rebar bond behavior are the main parameters under investigation.

In addition to a monotonic loading protocol, some rebar pull-out tests were also carried out with cyclic loading protocol to investigate the ability of HyFRC in regards to resisting deterioration under repeated loading.

2.2.2 Materials

The mixtures for conventional rebar pull-out test specimens are shown in Table 1. Micro PVA fibers (PVA-1) and macro hooked-end steel fibers, SF-1 (DRAMIX RC-80/60-BN fiber) and SF-2 (DRAMIX ZP305 (Bekaert) fiber), with different lengths are incorporated into the HyFRC while OC is HyFRC's control mixture without fibers. With 50% fly ash replacement, OC-50FA and HyFRC-50FA are the mixtures modified from OC and HyFRC respectively. ECC only incorporates PVA fibers (PVA-2) as reinforcement. Such a material has much lower aggregate content and higher cement paste content comparing to other mixture in the table and do not have coarse aggregates. Silica sands (0.13 mm particle size) are used as fine aggregates for ECC and no coarse aggregates are used for such a material. Gravels with 3/8 inch (9.52 mm) of maximum size of aggregates (MSA) and Vulcan sands (2.9 of fineness modulus and 0.6 mm of medium particle size) are used as coarse and fine aggregates for other mixtures (OC, OC-50FA, HyFRC and HyFRC-50FA) respectively. Table 2 summarizes the properties of the fibers used in the mixtures and Figure 18 shows the dimensions of hook end steel fibers.

Table 1: Mixture for conventional rebar pull-out test specimens (per m³)

Mixture	Cement (kg)	Fly ash (kg)	Fine aggregate (kg)	Coarse Aggregate (kg)	Water (kg)	SP (L)	VMA (L)	SF-1 (% vol.)	SF-2 (% vol.)	PVA-1 (% vol.)	PVA-2 (% vol.)	w/c
OC	424	0	854	758	228	0.00	0	0	0	0.00	0	0.54
OC-50FA	234	234	852	774	187	0.46	0	0	0	0.00	0	0.40
HyFRC	423	0	852	774	228	0.00	0	0.8	0.5	0.2	0	0.54
HyFRC-50FA	234	234	852	734	187	0.46	0	0.8	0.5	0.2	0	0.40
ECC	548	657	438	0	312	2.58	0.197	0	0	0	2	0.26

Note: (for Table 1)

- SP (superplasticizer): Melflux 2641 is used for ECC
- VMA (viscosity modifying agent): Cellulose is used for ECC
- w/c: water-to-cementitious material ratio, water-to-binder ratio

Table 2: Fiber properties

Fiber	Mix	Material	Length (mm)	Diameter (mm)	Strength (MPa)	Stiffness (GPa)
SF-1	HyFRC	Steel, hook end	60	0.75	1225	210
SF-2	HyFRC	Steel, hook end	30	0.55	1350	210
PVA-1	HyFRC	Polyvinyl alcohol	8	0.038	1600	40
PVA-2	ECC	Polyvinyl alcohol	12.7	0.04	1600	43
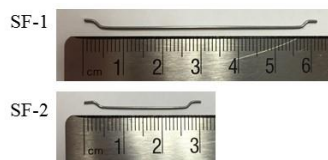
Figure 18: Hook end steel fiber dimensions

2.2.3 Test specimens

The specimen for conventional rebar pull-out test consists of a No. 4 or No. 8 deformed reinforcing bar centrally embedded in a cementitious matrix as shown in Figure 19 and such a specimen dimension is referred as "d1". The geometry information of rebars is summarized in Table 3 for reference. The matrix is a cylinder with 152.4 mm diameter and 304.8 mm height. In this case, the ratios between concrete/cement-composite cover thicknesses and rebar diameters (c/d_b) are 5.5 and 2.5 for specimens with No. 4 and No. 8 rebar, respectively. Two PVC (Polyvinyl Chloride) pipes (shown by dashed lines) were used to debond the surface of rebar from concrete and only the middle region of rebar bonded to concrete with bond lengths (L_e) selected as 3.5 times rebar diameter (d_b). In this case, approximately 5 ribs were located within the bond lengths. To account for any irregularity from fabrication process, the exact embedment lengths were measured right before casting which allows a more accurate bond stress calculation. Spirals were used as transverse reinforcement in some of specimens with no. 8 rebar, as shown in Figure 20. All of the specimens with no. 4 rebars were made without spiral. The spiral wire is an ASTM A641, Zinc–Coated (Galvanized) Carbon Steel with 483 MPa (70 ksi) of tensile strength and 3.43 mm of diameter. Herein, 25.4 and 12.7 mm of spiral spacing lead to 0.75 and 1.5 percent volume ratio for transverse reinforcement, respectively.
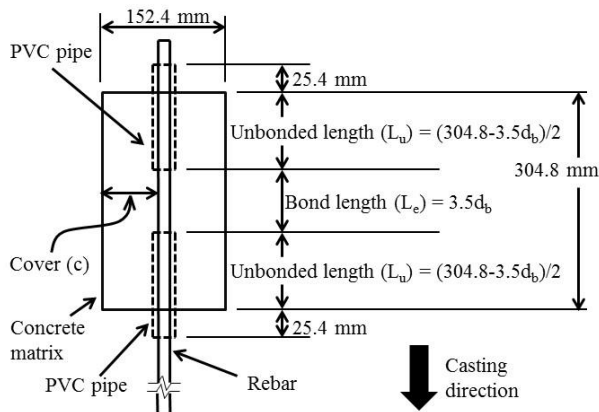
Figure 19: Specimen dimension 1 (d1)
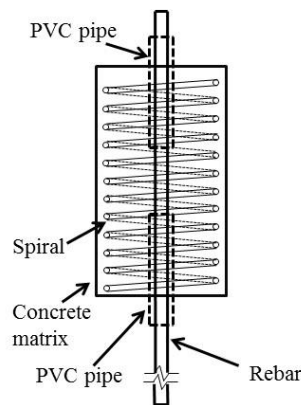
Figure 20: Spiral configuration for specimen dimension 1

Table 3: Rebar information for pull-out test

Rebar size	Diameter (mm)	Height of rib (mm)	Rib spacing (mm)	Rib height/rib spacing
No. 4	12.7	0.6985	8.7122	0.08
No. 8	25.4	2.845	18.29	0.156

During casting, wood frames were used to make sure the rebars were well centered, as shown in Figure 21, and a vibrator was used to achieve compaction for the fresh materials. The casted materials were kept in molds and covered by wet fabric and plastic sheet for moisture curing. The curing periods were 28 days for OC, HyFRC and ECC while the OC-50FA and HyFRC-50FA were cured for 56 days to achieve a similar compressive strength (f_c') as OC and HyFRC. To summarize the specimen conditions for conventional rebar pull-out tests, Table 4 and 5 show the properties for specimens with no. 4 and no. 8 rebars respectively.

Figure 21: Specimen sealed by plastic wrap

Table 4: Specimen condition for conventional No. 4 rebar pull-out test

Specimen name	Mixture	Presence of spiral	Spiral Volume fraction	Spiral spacing (mm)	Number of specimens	Specimen dimension	Moisture curing age (day)
OC-NC-d1	OC	No	0	-	4	d1	28
HyFRC-NC-d1	HyFRC	No	0	-	4	d1	28
ECC-NC-d1	ECC	No	0	-	4	d1	28

Table 5: Specimen condition for conventional No. 8 rebar pull-out test

Specimen name	Mixture	Presence of spiral	Spiral Volume fraction	Spiral spacing (mm)	Number of specimens	Specimen dimension	Moisture curing age (day)
OC-NC-d1	OC	No	0	-	3	d1	28
OC-C(0.75)-d1	OC	Yes	0.75%	25.4	3	d1	28
OC-C(1.5)-d1	OC	Yes	1.5%	12.7	3	d1	28
OC-50FA-NC-d1	OC-50FA	No	0	-	2	d1	56
OC-50FA-C(1.5)-d1	OC-50FA	Yes	1.5%	12.7	2	d1	56
HyFRC-NC-d1	HyFRC	No	0	-	3	d1	28
HyFRC-C(0.75)-d1	HyFRC	Yes	0.75%	25.4	3	d1	28
HyFRC-50FA-NC-d1	HyFRC-50FA	No	0	-	2	d1	56
ECC-NC	ECC	No	0	-	3	d1	28
ECC-C(1.5)	ECC	Yes	1.5%	12.7	3	d1	28

2.2.4   Test set-up and procedure

2.2.4.1   Monotonic rebar pull-out test

Conventional rebar pull-out tests with monotonic loading protocol were conducted by a 534 kN (120 kip) capacity universal testing machine (UTM120) and the test set-up for specimen with No. 8 rebar is shown in Figure 22. The matrix was supported by a bearing plate on the upper machine head when the rebar was gripped and pulled out by machined inserts in the lower head. The bottom debond region in the matrix kept the rebar bond region apart from the confinement stress field induced by the bearing plate. During testing, the load (F) applied to the rebar was recorded by a load cell in the hydraulic actuator, and the displacements measured by potentiometer 1 and 2 are correspond to the rebar slippage (s) against the matrix. The test set-up for specimens with No. 4 rebar is identical to the one shown in Figure 22, except that the cylindrical wedged rebar pulling grips were used in the lower machine head.

For compression test, additional 102x203 mm concrete cylinders were casted with same batch materials as the rebar pull-out specimen. Three cylinders were tested for f_c' of each batch of concrete and cementitious composite mixtures except that compressive tests were conducted for two cylinders for the f_c' of ECC mixture used for no. 8 rebar pull-out test. The obtained f_c' indicates the casting quality and is used to normalize the bond stress for direct comparison, independent of f_c'.
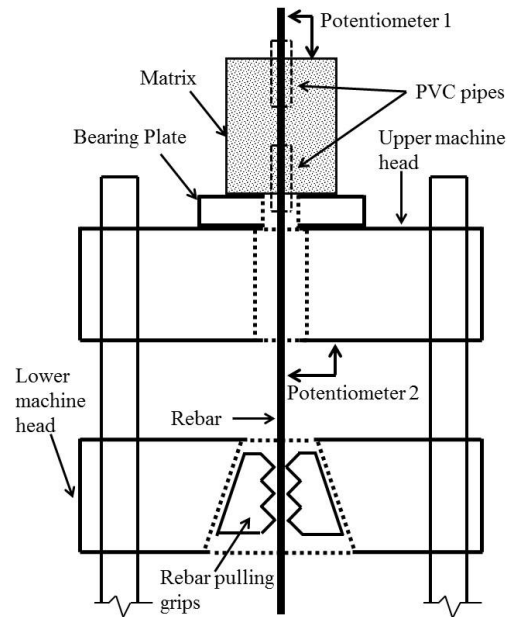
Figure 22: Set-up for conventional No. 8 rebar pull-out test with monotonic loading protocol

2.2.4.2   Unidirectional cyclic rebar pull-out test

Unidirectional cyclic rebar pull-out tests were conduct for No. 8 rebar specimens on an MTS 311.41 load frame with 1112 kN (250 kips) of tensile capacity and 2224 kN (500 kips) of compressive capacity. In general, the instrumentation and restraints for such a test are similar to that of the monotonic rebar pull-out test but the set-up is inverted as shown in Figure 23. The rebar was stressed/pulled out by a mechanical coupler connected with the machine head and the rebar slippages were measured by two LVDTs. Instead of monotonic tensile loading, the rebar was repeatedly loaded in tension and unloaded according to two kinds of loading protocols, labeled p1 and p2. Such loading protocols were determined according to [28].

Figure 23: Set-up for conventional rebar pull-out test with cyclic loading protocol

In loading protocol 1 (p1), the cyclic loadings were controlled according to selected rebar slippages increments. Tensile load was applied to the rebar until reaching 0.76 mm of rebar slippage at which point the rebar was unloaded. Such a loading/unloading process was repeated for 6 cycles to gain 0.76 mm of slippage increment in each cycle. Then, another 13 cycles were conducted in same manner with 1.52 mm of slippage increment. Finally, the rebar was pulled-out monotonically.

As show by the results presented later in this section, in general, the rebar slippages at peak bond stresses for the monotonic rebar pull-out tests conducted are lower than the rebar slippages at peak bond stresses [28] reports. This is due to different specimen dimensions and test set-ups. Therefore, the 0.76 mm (0.03 inch) rebar slippage increments for the first six cycles of p1 were selected to be lower than the 1.27 mm (0.05 inch) rebar slippage increments used in the unidirectional cyclic rebar pull-out tests in [28]. To terminate the tests in manageable times, the slippage increments were increased to 1.52 mm in the following cycles which occurred after the peak bond stresses.

An average peak bond stress normalized by f_c' can be calculated for OC and HyFRC from the results of monotonic rebar pull-out tests. Different percentages of such averaged values were used as bond stress targets for cyclic loadings in protocol 2 (p2). In this case, the specimens were loaded until 50%, 65%, 80%, 90% and 100% of the normalized peak bond stress was reached

22

and unloaded. Table 6 provides the number of cycles utilized at each load level. If the bond stress decreases before reaching current bond stress target, the specimen was unloaded as well. Some specimens did not exhibit obvious strength decrement after being loaded to 100% of normalized peak bond stress from monotonic testing so additional cycles having 110% and 120% peak stress as target were performed until the target was no longer reachable.

Table 6: Loading protocol 2 (p2) for cyclic test

Percentage of normalized peak bond stress	50%	65%	80%	90%	100%
Number of cycles	3	3	5	5	3~5

2.2.5 Test results and discussion

2.2.5.1 Compressive behavior for HyFRC

Compressive tests were conducted on HyFRC specimens from the same batch material used for the no. 8 rebar pull-out specimens with D1 dimension. The compressive stress-strain curves are shown in Figure 24.
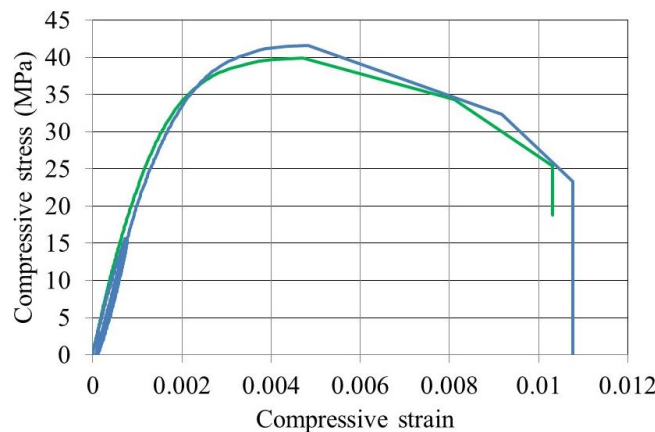
Figure 24: Compressive stress-strain curves for HyFRC

2.2.5.2 Bond stress calculation and normalization

The averaged bond stress along the rebar embedment length can be calculated from the load (F) applied to rebar with the following equation:

$$\tau = \frac{F}{\pi \, d_b \, l_e} \qquad (1)$$

$\tau = $ Bond stress [MPa]

$F = $ Load [N]

$d_b = $ Bar diameter [mm]

$l_e = $ Embedment length [mm]

Equation (2) calculated the normalized bond stress according to the method provided in [10].

$$\tau_{(f_c'=36.8 \, MPa)} = \tau \sqrt{\frac{36.8}{f_c'}} \qquad (2)$$

$\tau_{(f_c'=36.8 \, MPa)} = $ Normalized bond stress [MPa]

$\tau = $ Experimental bond stress calculated from equation (1)

$f_c' = $ Concrete compression strength [MPa]

2.2.5.3 Monotonic pull-out test program for specimens with no. 8 rebars

2.2.5.3.1 Change in Failure Mode

The cracking behavior observed from the rebar pull-out tests is similar to what is reported in the literature. The bearing action between rebar ribs and matrix leads to a tension ring stress field around the rebar which cracks the matrix in radial direction. In this case, 2 to 4 fully developed splitting cracks in radial direction lead to splitting failure accompanied by rebar/matrix detachment for an unconfined OC specimen as shown in Figure 25. Instead of having splitting failure, all of the specimens with either fiber or spiral reinforcement exhibit frictional pull-out failure accompanied by a high number of fine splitting cracks. Figure 26 shows a saw cut cross-section that exhibits frictional pull-out behavior with multiple fine splitting cracks which propagated radially away from the rebar.
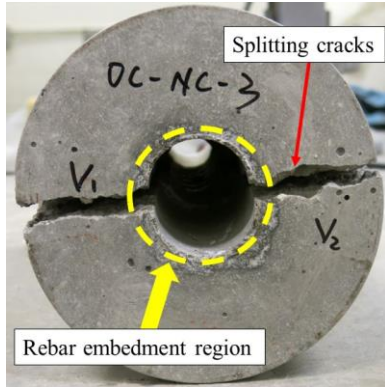
Figure 25: Splitting failure for
OC-NC specimens
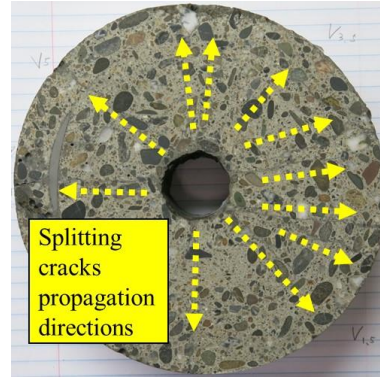
Figure 26: Frictional pull-out
failure mode for OC-C(0.75)

2.2.5.3.2 Normalized bond stress-rebar slippage curves

The normalized bond stress-rebar slippage curves for unconfined/spiral-confined OC and HyFRC without fly ash are shown in Figure 27a and 27b, for overall and low slippage ranges respectively.

The OC-NC specimen loses bond resistance immediately after peak bond stress because of rebar/matrix detachment caused by splitting failure. By transferring failure mode into a frictional pull-out, unconfined HyFRC matrix improves the peak bond stress and provides residual bond resistance at the softening branch. A rebar in such a HyFRC matrix also exhibits better bond behavior compared to that in an OC confined with 0.75% volume fraction of spiral. The spiral volume fractions are required to be as high as 1.5% for OC specimens to reach post peak performances comparable to unconfined HyFRC. In addition, HyFRC exhibits a stiffer ascending branch before the peak bond stress because the fibers close to the rebar are able to resist the inclined bond cracks and splitting cracks at crack initiation stages while the spiral engages after the cracks propagated further at later stages. Such a stiffer ascending curve is interpreted as a more significant slip stiffening behavior for a rebar provided by a HyFRC matrix. Confining HyFRC with 0.75% of spiral further improves the rebar pull-out behavior in such a material and as a result, the confined HyFRC matrix provides significantly higher bond resistant compared to confined OC matrix (with 0.75% or 1.5% of spiral).

(a)

(b)
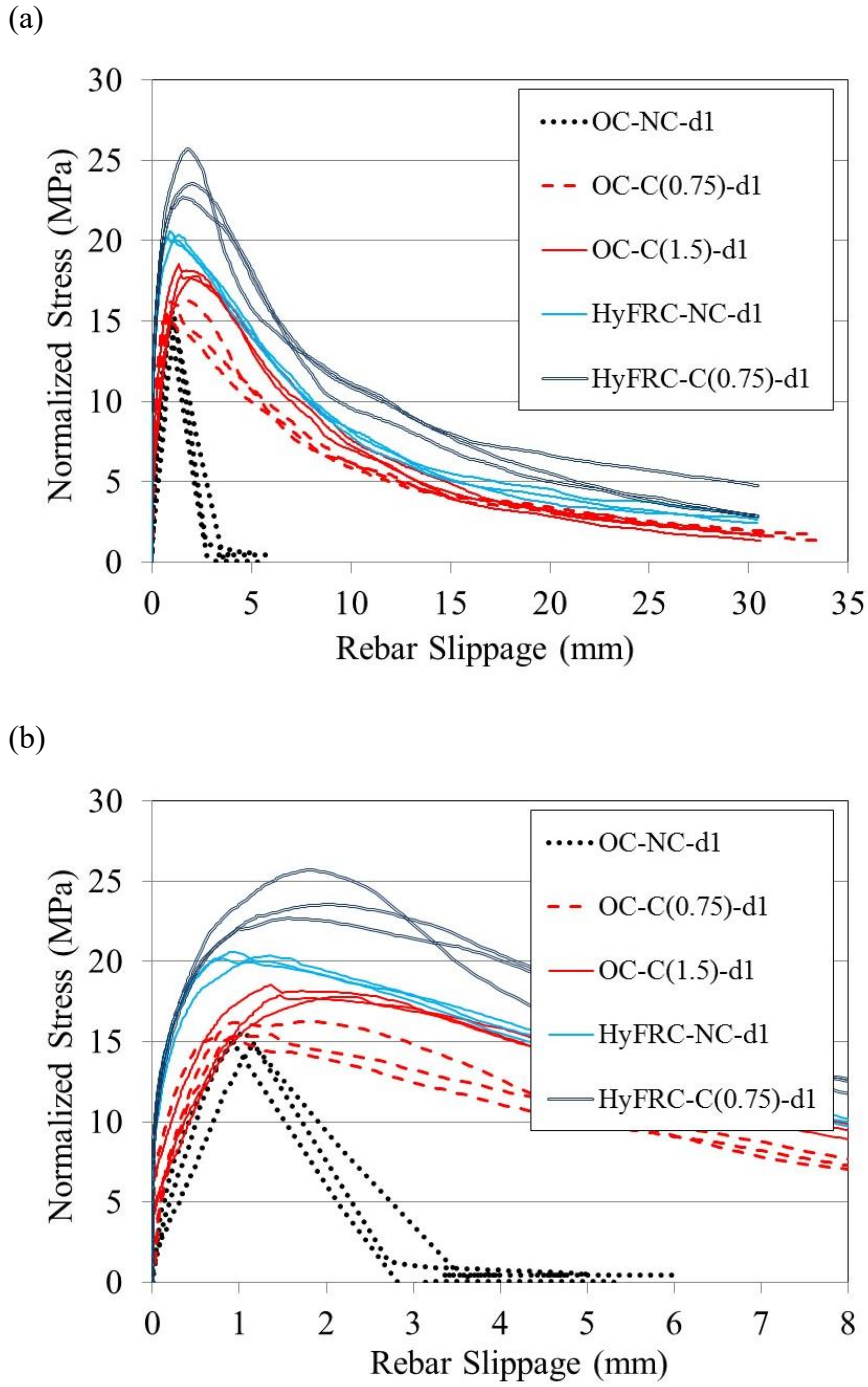
Figure 27: Slippage-normalized bond stress curves for conventional rebar pull-out test in (a) Overall slippage range (b) Low slippage range

26

As it will be discussed in detail in Chapter 3, the HyFRC matrix provides superior slip stiffening behavior and high peak/residual pull-out resistance of rebar because of the presence of the PVA microfibers which are able to increase the pull-out resistance of the steel macrofibers. When a steel macrofiber is bridging a splitting crack, such fiber is initially stretched and then, pulled out from the matrix gradually. By resisting pull-out of steel macrofibers, PVA microfibers make such macrofibers provide higher crack closure stress. Therefore, higher normal stress is induced to grip the rebar. The experimental results in chapter 3 will indicate that such synergy between micro and macro fibers exists in HyFRC and improves the rebar pull-out resistance.

In order to investigate the effect of fly ash, the normalized bond stress-rebar slippage curves for matrix without/with 50% fly ash replacement are compared for: unconfined OC, confined OC and unconfined HyFRC, in Figure 28a, 28b and 28c respectively.

The unconfined OC specimens without and with fly ash exhibit similar peak bond stress. Such behavior is expected because the splitting failures of unconfined OC matrices are governed by their tensile strengths and similar tensile strengths are presumed for such matrices without/with fly ash due to their similar f_c'. On the other hand, it is expected that the fly ash enhances the bond resistances for specimens with frictional pull-out failures by densifying the rebar/matrix interfaces. The bond behaviors of confined OC match such a trend with increments of peak bond stresses induced by fly ash. Oppositely, fly ash decreases the rebar pull-out resistances in unconfined HyFRC. According to experimental evidence reported in the literature, fly ash decreased both chemical and frictional bond between PVA fibers and matrix [63]. In this case, the PVA fiber pull-out resistance which is reduced by fly ash in the HyFRC-50FA matrix provides less crack closure stress to restrain micro cracks. In addition, the bond performances of steel macrofibers may be degraded by fly ash as well, because the microfiber reinforced matrix is less effective in resisting steel macrofiber pull-outs. Such characteristic is shown by the fiber pull-out test results reported in section 3.4.1.3 and is further discussed in section 3.5.3 based on the fiber pull-out test results. Although fly ash may improve certain degree of rebar pull-out resistance by densifying the interface between matrix and steel rebar/macrofibers, the bond degradations of micro and macro fibers caused by fly ash is more dominant in affecting the rebar pull-out performance. Therefore, fly ash reduced the rebar pull-out resistance provided by the HyFRC.

(a)
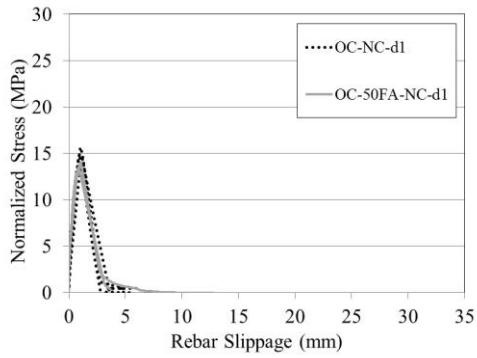
(b)
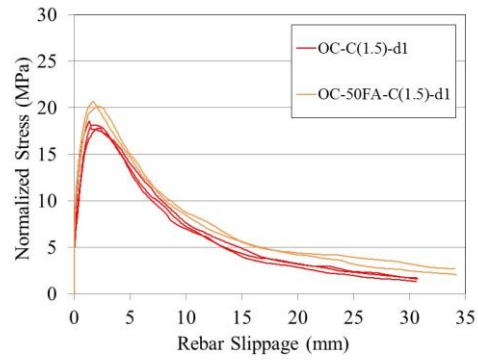
(c)
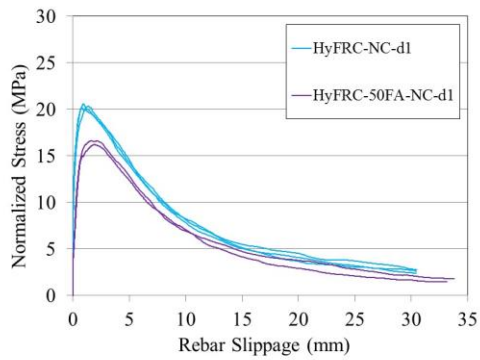
Figure 28: Slippage-normalized bond stress curves for (a) unconfined OC specimens without and with fly ash (b) confined OC specimens without and with fly ash (c) unconfined HyFRC specimens without and with fly ash

The normalized bond stress-rebar slippage curves for unconfined and confined ECC specimens are compared with unconfined and confined HyFRC specimens in Figure 29.
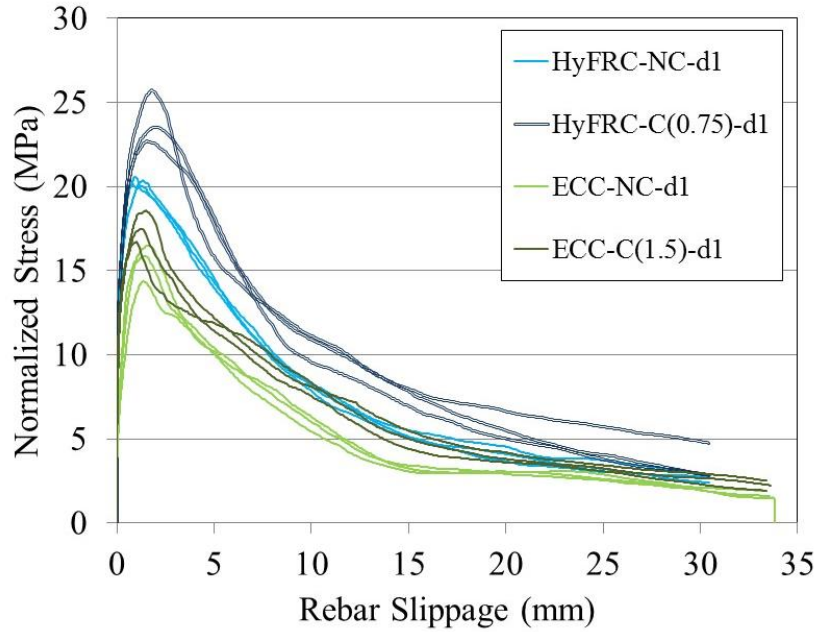
Figure 29: Slippage-normalized bond stress curves for comparison of HyFRC and ECC without/with spiral

The bond performance of HyFRC specimens exceeds the performance of ECC specimens. Contrary to HyFRC specimens, in which spiral improved the bond resistance, using spirals in ECC didn't lead to observable enhancement of bond resistance. In the literature, a similar effect was observed in lap splice beam bending tests [64]. Bandelt et al. indicates that transverse reinforcements didn't enhance the peak bond stresses for longitudinal rebars in ECC, but increased the bond strengths in the HyFRC material, similar to what is presented herein.

Table 7 summarizes the results obtained from rebar pull-out tests, and lists the failure modes and compressive strengths of the various specimens.

Table 7: Summary of monotonic pull-out tests for d1 specimen with no. 8 rebar

Specimen	Averaged compressive strength (MPa)	Max. normalized bond stress (MPa)	Average of max. normalized bond stress (MPa)	Slip at peak stress (mm)	Average of slip at peak stress (mm)	Failure mode
OC-NC-d1-1	41.93	14.74	15.16	0.97	0.85	Splitting failure
OC-NC-d1-2		15.64		0.86		
OC-NC-d1-3		14.95		0.73		
OC-C(0.75)-d1-1		16.26	15.64	1.48	1.08	Frictional pull-out
OC-C(0.75)-d1-2		15.43		1.06		
OC-C(0.75)-d1-3		15.23		0.69		
OC-C(1.5)-d1-1	36.50	18.53	18.05	1.36	1.67	
OC-C(1.5)-d1-2		17.78		2.19		
OC-C(1.5)-d1-3		17.91		1.47		
HyFRC-NC-d1-1	40.04	20.19	20.39	0.81	1.02	
HyFRC-NC-d1-2		20.33		1.35		
HyFRC-NC-d1-3		20.60		0.91		
HyFRC-C(0.75)-d1-1		25.70	23.98	1.81	1.78	
HyFRC-C(0.75)-d1-2		22.67		1.54		
HyFRC-C(0.75)-d1-3		23.49		2.00		
OC-50FA-NC-d1-1	41.51	13.54	13.80	0.87	0.95	Splitting failure
OC-50FA-NC-d1-2		14.06		1.04		
OC-50FA-C(1.5)-d1-1		20.68	20.39	1.73	1.89	Frictional pull-out
OC-50FA-C(1.5)-d1-2		20.10		2.05		
HyFRC-50FA-NC-d1-1	43.88	16.21	16.42	1.91	1.79	
HyFRC-50FA-NC-d1-2		16.63		1.67		
ECC-NC-d1-1	52.22	16.50	15.58	1.60	1.45	
ECC-NC-d1-2		15.87		1.41		
ECC-NC-d1-3		14.36		1.35		
ECC-C(1.5)-d1-1		18.56	17.57	1.52	1.26	
ECC-C(1.5)-d1-2		16.69		1.01		
ECC-C(1.5)-d1-3		17.47		1.27		

2.2.5.3.3 Splitting crack characteristics for specimens with frictional pull-out failures

Table 8 lists the number of splitting cracks on saw-cut cross sections from specimens with frictional pull-out failure. In general, a larger splitting crack number usually infers that the matrix exhibited a more significant hardening behavior during rebar pull-out because the hardening behavior allows continuously increased stress at cracked region to be redistributed to uncrack regions and open new splitting cracks. Note that the crack numbers of unconfined and spiral-confined ECC specimens are special cases. The crack numbers of ECC are lower than HyFRC but it doesn't mean that ECC material has worse ability to provide hardening behavior when mechanical load is applied. Such characteristic will be discussed later in this section.

Table 8: Number of splitting crack branches

Specimen name	Number of radial splitting crack branches
OC-C(0.75)	38
OC-C(1.5)	22
OC-50FA-C(1.5)	15
HyFRC-NC	56
HyFRC-C(0.75)	33
HyFRC-50FA-NC	35
ECC-NC	25
ECC-C(1.5)	27

The HyFRC-NC (unconfined HyFRC without fly ash) exhibits most cracks in Table 8 due to its superior ability for stress redistribution in cracked regions. In such a matrix, many crack branches are close to each other as shown in Figure 30. On the other hand, the confined OC exhibits minimal amount of crack branches along a crack path. Figure 31 gives an example for this type of isolated splitting crack in OC-C(0.75).

To explain the difference in the number of splitting crack between unconfined HyFRC and spiral-confined OC specimens shown in Table 8, we refer to the schematic shown in Figures 32 and 33. After the splitting cracks form, the stress states around the rebar, shown as concentric tension rings, remain similar in the unconfined HyFRC specimen since the fibers maintain continuity of the tension rings along the cracks, as shown in Figure 32. This continuity allows other cracks to initiate. The tensile stress in circular direction around an existing crack is ideal to form new cracks both in close vicinity and other locations. In Fig. 32, the new cracks can form at both the dashed blue lines and the region within these lines. Such characteristic leads to the high

density of cracks observed in Fig. 30. On the other hand, due to lack of crack bridging and hence lack of closure stresses, no tensile stresses are being transferred across the splitting cracks in spiral-confined OC except at the locations where the spiral bridges the cracks as shown in Figure 33. Hence, in regions in close vicinity to the splitting cracks, the stress patterns are disrupted. In fact, the tensile stresses in these regions are no longer circular except at the spiral. In this case, new cracks form at regions far away from the initially formed cracks because higher circular component of tensile stress occurs at these regions. For example, a new crack is easier to form at the location indicated by the dashed blue line in Figure 33. Such characteristics decrease the density of cracks; hence confined OC exhibits more isolated and less splitting cracks compared to unconfined HyFRC.
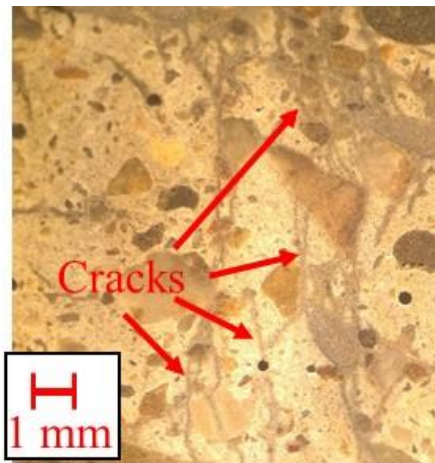
Figure 30: Branched multiple cracking for HyFRC-NC

Figure 31: A isolated splitting crack for OC-C(0.75)

Similar to the mechanisms described above, the presence of spirals also decreases the number of splitting cracks in HyFRC. Even if the fibers allow some tensile stress to be transferred across a splitting crack, the spiral localizes such a stress transformation at a single spot and thereby affect the stress pattern as shown in Figure 34.
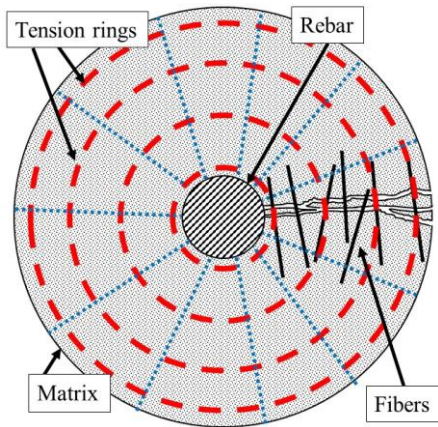
Figure 32: Tension ring for matrix with fiber reinforcement after cracking
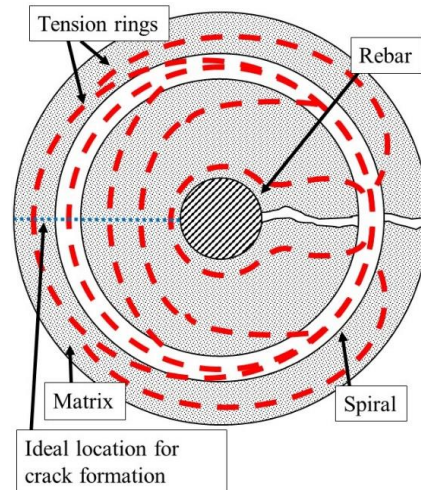
Figure 33: Tension ring for matrix with spiral reinforcement after cracking
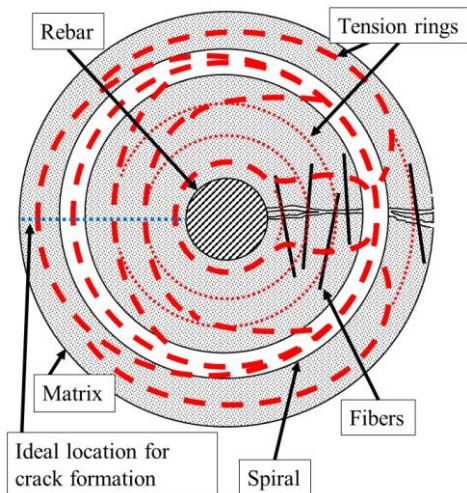
Figure 34: Tension ring for matrix with both spiral and fiber reinforcement after cracking

Incorporating 50% fly ash replacement in unconfined HyFRC leads to a decrease in the number of cracks, which indicates a less significant hardening behavior in the fiber reinforced matrix. Such a reduction in hardening behavior may be caused by decreases of micro/macro fiber pull-out resistances which are induced by fly ash as will be discussed later. Another factor for the reduction in splitting cracks in HyFRC with fly ash may be the denser interface between rebar and matrix due to fly ash which increases the stress for crack initiation. The same reasons may be responsible for the reduced number of splitting cracks in OC-50FA-C(1.5) compared to that in OC-C(1.5).

33

A unique splitting crack pattern was observed in the rebar pull-out specimens made of unconfined and confined ECC matrices. Instead of cracks propagating from the rebar to the concrete free surface as in confined OC and unconfined/confined HyFRC, most cracks only propagate up to 5 to 6 mm away from rebar. No visible cracks were observed at the outer region further away from the rebar as shown in Figure 35 for unconfined ECC. Similar crack patterns were also observed in confined ECC. Hence, ECC matrices seem to be more effective in resisting splitting cracks compared to spiral reinforcements or HyFRC matrices. The high amount of PVA fibers allow the ECC matrix to resist the splitting cracks effectively right after crack initiation. The radial expansion only occurs in the ECC matrix close to the rebar so the spiral which is located further away from the rebar is not being mobilized. This is contrary to the OC and HyFRC specimens where the whole matrix dilates and hence mobilized the spiral. This explains the similarity between ECC specimens with and without spiral in regards to crack patterns, number of cracks, and the bond performances provided by the normalized bond stress-rebar slippage curves.
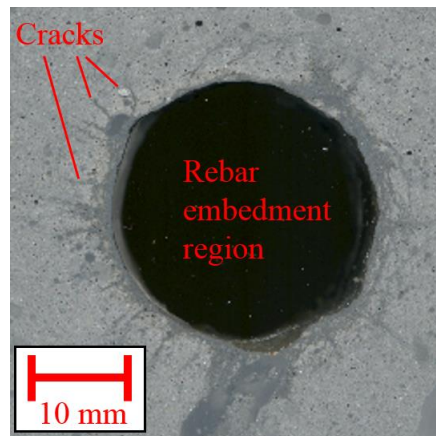
Figure 35: Splitting cracks for ECC-NC after no. 8 rebar pull-out

The ECC matrix exhibits superior splitting crack resistance, however, its rebar pull-out resistance is inferior compared to a HyFRC matrix. The difference in pull-out resistance between ECC and HyFRC is caused by their different cement paste/aggregate proportions and presence/lack of coarse aggregates. According to the literature, pull-out tests performed on ribbed FRP (fiber reinforced polymer) bars shows that a FRC with coarse aggregates provides higher pull-out strength compared to an ECC [65]. The authors argue that the coarser aggregates in FRC are responsible for the higher bond strength by increasing the interlocking and friction at bar/matrix interface. The same reasoning can explain the rebar pull-out tests reported herein. Compared to ECC, the significantly higher aggregate content, larger size of fine aggregates and the presence of coarse aggregates in HyFRC lead to its higher steel rebar pull-out resistance by increasing the

interlocking/friction not only at the rebar/matrix interface but also within the partially/fully developed shear cracks around the rebar.

Although ECC is designed to exhibit a much higher strain capacity compared to HyFRC and hence one would expect a higher number of splitting cracks around the rebar, the lower maximum bond stress of ECC limits its performance. Before more significant number of splitting cracks could develop in ECC, the crushing/shear failure in the matrix keys became dominant and the bond stress started to decrease followed by crack stabilization. Therefore, the ECC was unable to develop as many splitting cracks as HyFRC.

2.2.5.4 Monotonic pull-out test for specimens with no. 4 rebars

Monotonic pull-out tests were conducted for specimens with no. 4 rebar and the test results are summarized in Table 9. With a higher c/d_b ratio and lower rebar rib height/rib spacing ratio, the dimensions of such specimens are more likely to provide a frictional pull-out failure mode compared to the specimens with no. 8 rebars. No matter if spiral and fiber reinforcements were used or not, all of the no. 4 rebar specimens exhibited frictional pull-out failure rather than splitting failure.

The averaged normalized bond stress-rebar slippage curves for no. 4 rebar specimens with different matrices are plotted for overall and low rebar slippage range in Figure 36a and 36b respectively. Because frictional pull-out failures were induced in all specimens by the specimen dimension, replacing an unconfined OC matrix with a HyFRC matrix improved peak/residual bond stress in a less significant manner compared to the improvement observed in no. 8 rebar specimens. The ECC provides the stiffest ascending branch up to the peak bond stress among all matrix materials but its softening behavior is identical to OC.

The crack patterns after no. 4 rebar pull-outs were observed on saw cut cross sections. In Figure 37, the cracks are marked in red color for the OC and HyFRC matrices and both of them exhibit similar internal splitting cracks. By bridging such cracks, the fibers in HyFRC confined the matrix internally which leads to a smoother softening behavior as shown in Figure 36.

Table 9: Summary of monotonic pull-out tests for d1 specimen with no. 4 rebar

Specimen	Averaged compressive strength (MPa)	Max. normalized bond stress (MPa)	Average of max. normalized bond stress (MPa)	Slip at peak stress (mm)	Average of slip at peak stress (mm)	Failure mode
OC-NC-d1-1	42.86	19.84	17.91	1.41	1.39	Frictional pull-out
OC-NC-d1-2		17.85		1.55		
OC-NC-d1-3		17.09		1.48		
OC-NC-d1-4		16.81		1.13		
HyFRC-NC-d1-1	36.75	21.29	21.63	1.29	1.31	
HyFRC-NC-d1-2		20.26		1.31		
HyFRC-NC-d1-3		22.12		1.38		
HyFRC-NC-d1-4		22.81		1.27		
ECC-NC-d1-1	45.07	21.50	20.12	0.68	0.64	
ECC-NC-d1-2		18.47		0.45		
ECC-NC-d1-3		22.25		0.77		
ECC-NC-d1-4		18.19		0.65		

Similar to the ECC specimen with no. 8 rebar, the ECC with no. 4 rebar also reveals radial splitting cracks only in the ECC matrix close to the rebar as shown in Figure 38. Again, the lower aggregate content, smaller size of fine aggregates and lack of coarse aggregates in ECC are responsible for the low frictional resistance represented by the softening curve beyond the peak bond stress. Therefore, the descending branch for ECC in Figure 36 follows that of OC.

(a)
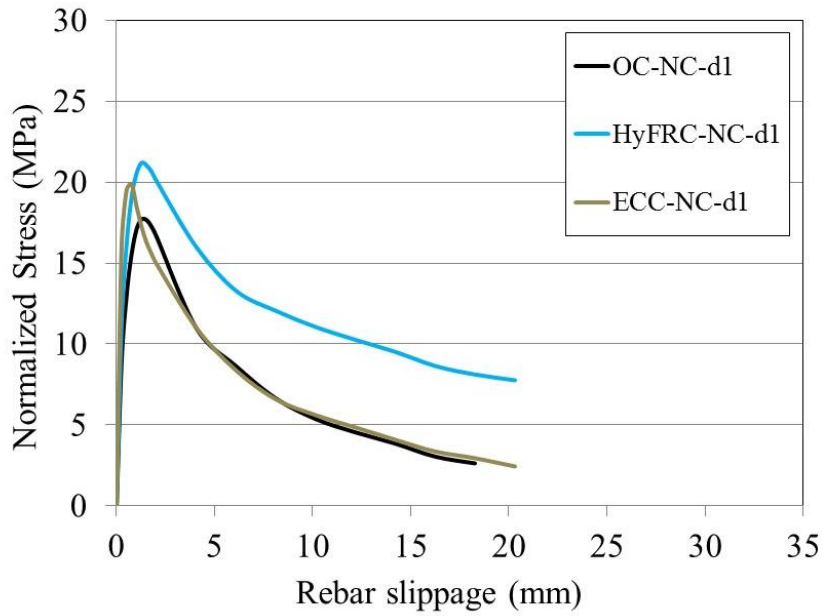
(b)
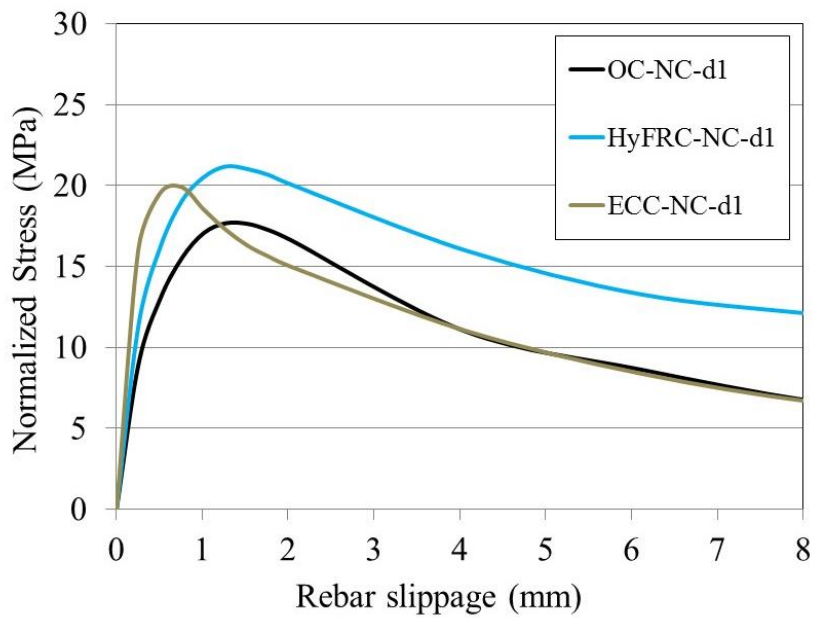
Figure 36: Averaged of normalized bond stress-rebar slippage curves for no. 4 rebar pull-out test in (a) overall slippage range (b) low slippage range
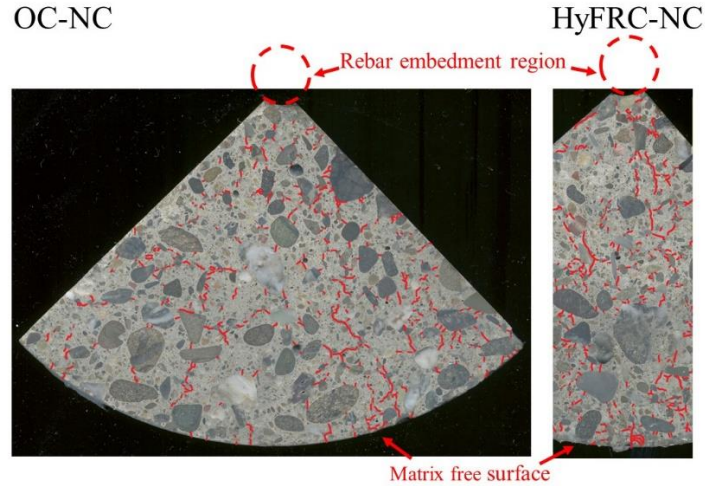
OC-NC   HyFRC-NC

Figure 37: Crack patterns for OC-NC and HyFRC-NC after no. 4 rebar pull-out
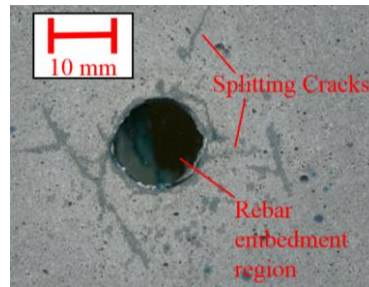
Figure 38: Crack pattern for ECC-NC after no. 4 rebar pull-out

2.2.5.5 Unidirectional cyclic pull-out test for specimens with no. 8 rebars

In addition to monotonic loading, pull-out tests were also conducted for specimens with no. 8 rebars under cyclic tensile loading. Figure 39 shows the normalized bond stress-rebar slippage curves for OC-C(1.5) and HyFRC-NC specimens tested under cyclic loading protocols, p1 and p2, and the monotonic pull-out behaviors for same type of specimens are shown in each figure for comparison. Note that the specimens tested under monotonic and cyclic loading were made by different batch materials. As shown in Table 7, the averaged f_c' for OC-C(1.5) and HyFRC-NC specimens tested monotonically are 36.50 and 40.04 MPa respectively. The averaged f_c' for OC-C(1.5) and HyFRC-NC specimens tested under cyclic loading are 39.5 and 39.8 MPa respectively.

Figure 39: Cyclic rebar pull-out behavior v.s. monotonic rebar pull-out behavior

Specimen	OC-C(1.5)-d1	HyFRC-NC-d1
p1 loading v.s. monotonic loading	Overall response: 	Overall response:
p2 loading v.s. monotonic loading	Overall response: Low rebar slippage range: 	Overall response: Low rebar slippage range:
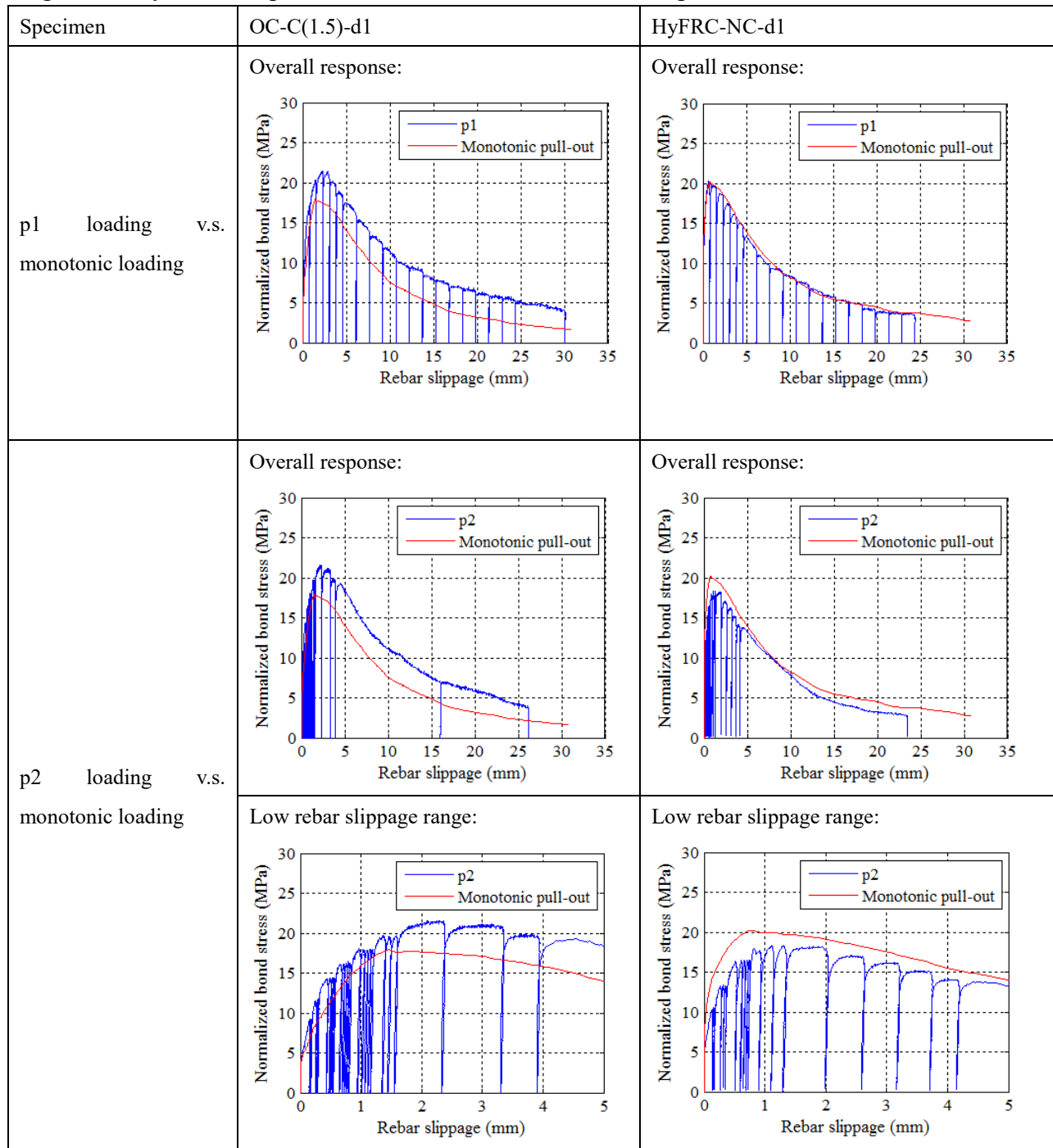
Both OC-C(1.5) and HyFRC-NC exhibit bond strengths under cyclic loadings similar to the pull-out resistance under monotonic loadings no matter what kind of loading protocol is used. Such characteristics indicate that minimal amount of additional bond damages was induced by repeated tensile loading. In the literature, unidirectional cyclic pull-out tests were performed for other types of HPFRCC by Chao [28]. He also reported that additional bond strength degradation from repeated load cycles is minimal in some matrices with 1% and 2% of Torex fiber, a twisted polygonal steel fiber. Compare to the OC-C(1.5) tested under monotonic loading, the slightly higher pull-out resistance for the same type of specimen tested under cyclic loading may be due to the slightly different compressive strengths of different batch materials.

2.3 Modified rebar pull-out test accompanied by digital image correlation (DIC) technique

2.3.1 Introduction

In addition to conventional rebar pull-out tests, modified rebar pull-out tests accompanied by digital image correlation (DIC) technique were conducted to unconfined and spiral-confined HyFRC specimens to further investigate the rebar/HyFRC matrix bond characteristics and the effect of spiral on such performance. The DIC technique provides detailed surface information on strain distribution, crack patterns and crack widths at various rebar pull-out stages. To apply DIC measurements, the specimen configurations and test set-up were changed slightly. The modified rebar pull-out tests and the DIC results are being discussed in following sections.

2.3.2 Materials and test specimens

For the modified rebar pull-out test, unconfined HyFRC and spiral-confined HyFRC (0.75% volume fraction of spiral) matrix with mixture proportions shown in Table 1 (the HyFRC mixture without fly ash) were used for the rebar pull-out specimens. The specimens were made with a modified specimen dimension, d2, which differs from the d1 specimens used in chapter 2.2. The geometry information of d2 is given in Figure 40. The dimensions and conditions for d2 are very similar to the original dimension, d1, except that the casting direction was reversed and the top debonded region was removed. Therefore, the specimen without the top debonded region has an exposed free surface at the top of the rebar/matrix bond region and such an exposed surface is the Region of Interest (ROI) for DIC measurements. By reversing the casting direction, this surface is cast against the bottom surface of a cylindrical mold and hence provides a smooth

surface well suited for DIC measurements. Because the d2 specimens were also used for vibration tests, threaded holes were drilled at the bottom ends (ends of L_l in Figure 40) of the rebar in order to attach an accelerometer for measuring vibration. Table 10 provides information for d2 specimens.
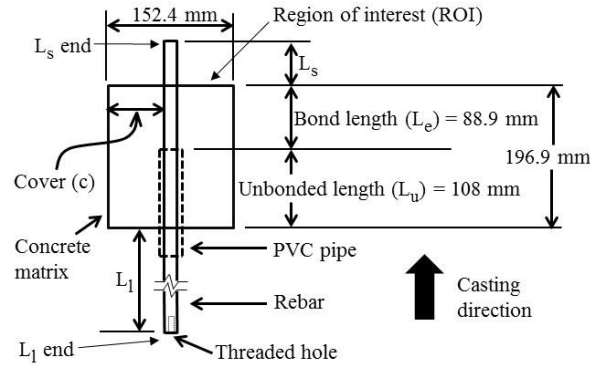
Figure 40: Specimen dimension 2 (d2)

Table 10: Specimen condition for pull-out test

Specimen name	Mixture	Presence of spiral	Spiral Volume fraction	Spiral spacing (mm)	Number of specimens	Specimen dimension	Moisture curing age (day)
HyFRC-NC-d2	HyFRC	No	0	-	2	d2	28
HyFRC-C(0.75)-d2	HyFRC	Yes	0.75%	25.4	1	d2	28

In order to apply the DIC technique, a random speckle pattern was generated on the ROI by spray paint. For optimal DIC results, the speckles need to be a few pixel wide (3 px to 15 px) in the camera photos capturing the ROI. Figure 41 shows the top view of a ROI and reveals various sections indicated as side 1, 2, 3 and 4 for a given specimen. 60 mm concrete strain gauges were attached on each section as shown in Figure 42. The gauges attached very close to the ROI are denoted as "T" whereas the strain gages attached at the middle of the bond region (which is $0.5L_e$ lower than the ROI) will be referred to as "M". The strain gauges T and M are present on all four sides of the specimen. Figure 42 indicates the locations of T4 and M4 strain gauges on the side 4 as an example.
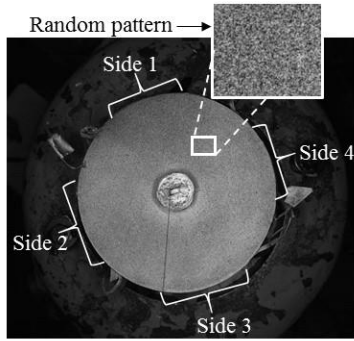
Figure 41: Top view of region of interest (ROI)
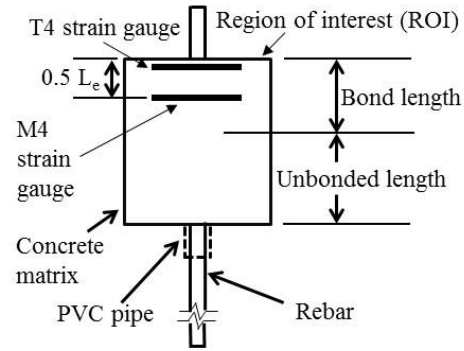
Figure 42: Side view for rebar pull-out specimen at side 4

2.3.3 Test set-up and procedure

The set-up for modified rebar pull-out test is very similar to that of the conventional rebar pull-out test except for some modifications shown in Figure 43 and 44 and summarized in Table 11. During rebar pull-out, a camera at the top took high resolution photos of the ROI in 4 second intervals. These photos were later used for the DIC analysis. Rather than clamping on the rebar directly, the potentiometer 1 was fixed at the horizontal beam above the specimen and connected the rebar with a piano wire to make sure that such a fixture won't block the view of camera. Due to the reversed casting direction, the matrix had a rough bottom surface rather than a smooth one. To provide a uniform stress transformation, a hydrostone was applied between the rough surface and the bearing plate as shown in Figure 44.
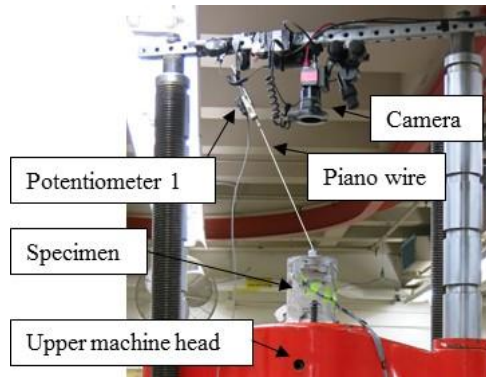
Figure 43: Modified pull-out test setup for DIC techniques

Figure 44: Support condition of modified pull-out test

Table 11: Comparison of test set-up and method for conventional and modified rebar pull-out test

Test name	Conventional rebar pull-out test	Modified rebar pull-out test
Test machine	534 kN (120 kip) capacity universal testing machine (UTM 120)	
Specimen dimension	d1	d2
Attaching method for Potentiometer 1	Clamping on free end of rebar	Connecting to free end of rebar with a piano wire
Attaching method for Potentiometer 2	Clamping on load end of rebar	
Monitored by DIC measuring system	No	Yes
Matrix supporting method	Supporting matrix bottom surface with a bearing plate on the upper machine head	
Hydrostone between matrix bottom surface and bearing plate	No	Yes
Rebar pull-out fixture	Machined inserts in the lower machine head	

2.3.4 Test result and discussion

2.3.4.1 Data processing method

The applied loads and rebar slippages measured during rebar pull-out test were converted to normalized bond stress-rebar slippage curves in same manner as that in conventional rebar pull-out tests.

The photos of ROI taken by the camera continuously captured the change of its speckle pattern caused by the matrix deformation and cracking during rebar pull-out. In a DIC software called Optecal [66], the algorithm subdivided each ROI image into subsets. Each subset was 41x41 pixels and the center-to-center distance between neighboring subsets was 13 pixels. Then, displacement and strain maps were calculated at every rebar pull-out stages recorded by a ROI image. Note that the strain calculation is unable to represent a discontinuity. As a result, a crack on ROI will be interpreted as a large continuous strain which visualizes the crack pattern. The crack widths can be calculated by the displacement field at each side of a crack. The measurements obtained from the strain gauges are used to verify the DIC measurements and to reveal the different mechanical behavior of the matrix at different heights.

2.3.4.2 Normalized bond stress-rebar slippage response

The normalized bond stress-rebar slippage curves for d2 specimens are plotted under overall and low rebar slippage range in Figure 45a and 45b, respectively. Table 12 summarizes the important values and failure modes for rebar pull-out tests and shows the corresponding compressive strengths from three of 102x203 mm cylinders made from the same batch material. The DIC measurements were conducted on both HyFRC-NC and HyFRC-C specimens.
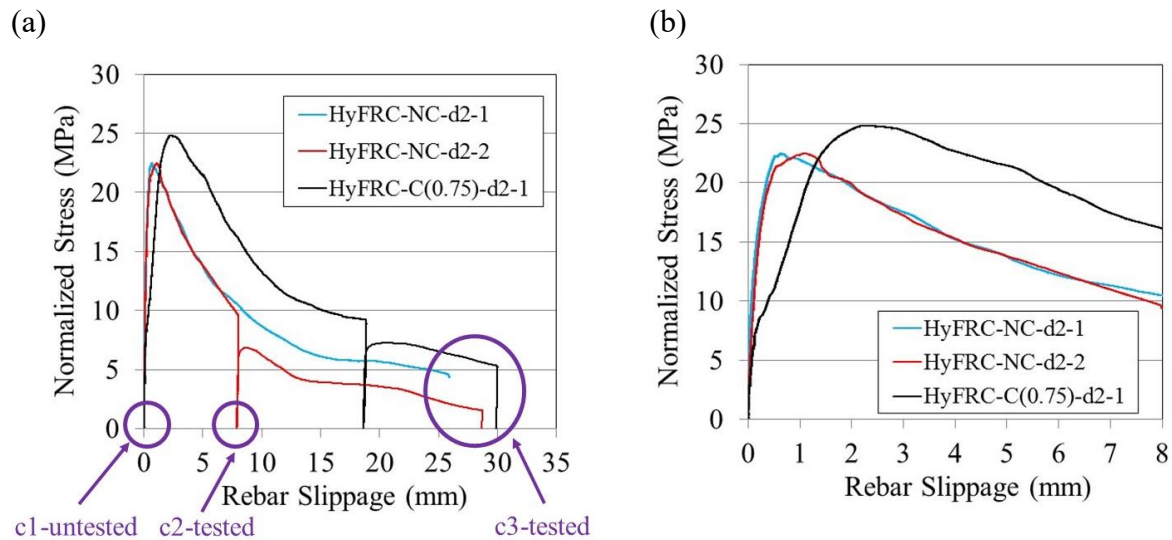
Figure 45: Normalized bond stress-slippage curves for d2 specimens in (a) overall slippage range (b) low slippage range

Table 12: Summary of pull-out tests for d2 specimen with no. 8 rebar

Specimen	DIC measurement	Averaged compressive strength (MPa)	Max. normalized bond stress (MPa)	Average of max. normalized bond stress (MPa)	Slip at peak stress (mm)	Average of slip at peak stress (mm)	Failure mode
HyFRC-NC-d2-1	No		22.5		0.65		
HyFRC-NC-d2-2	Yes	41.2	22.5	22.5	1.09	0.87	Frictional pull-out
HyFRC-C(0.75)-d2-1	Yes		24.9	24.9	2.27	2.27	

Since all these specimens exhibit frictional pull-out behavior, their bond stress-slippage responses exhibit a smooth softening branch after the peak. As shown in Figure 45, the spiral improves the rebar pull-out behavior in HyFRC d2 specimens in a similar manner as that in HyFRC conventional rebar pull-out test (i.e. d1 specimens discussed in section 2.2).

Compared to unconfined-HyFRC, spiral-confined HyFRC is expected to provide similar or slightly higher slopes for the ascending curves before peak bond stress as shown by the curves for d1 specimens (Figure 27b). The potentiometer 1 of d1 specimens was clamped to the rebars and directly measured the relative slippage between rebars and matrices. On the other hand, the rebar slippages for d2 specimens were calculated from the measurements from a potentiometer attached to the test machine with a steel beam (Figure 43). Although the bottom surfaces of d2 specimens were attached to the bearing plate with hydrostones, slightly non-uniform stress transformation between the specimens and bearing plate may still occur. If more bearing stress occurred at one side of the matrix, small amount of horizontal displacements can be induced to the top rebar tips, which were linked to potentiometer 1 with an inclined piano wire. Such rebar tip displacements induced different errors for the calculated rebar slippage values in different specimens. As a result, the ascending curve slope for spiral-confined d2 specimen is lower than the slope for the d2 specimen without spiral (Figure 45).

2.3.4.3 Interpretation of strain and crack characteristic on ROI

The strain fields on the top specimen surfaces were obtained with DIC measurements during rebar pull-out, and visualized with polar coordinates. Figure 46 compares strains in circular direction for different specimens at two different stages, occurrence of peak bond stress and 8

mm rebar slippage after peak bond stress. Cracks assumed to have strains higher than 0.002 can be identified easily on the strain map. When the peak bond stresses were reached, some splitting cracks had developed on the top specimen surfaces. Such cracks continued to develop beyond the peak bond stresses and then, stabilized at certain rebar slippage. Herein, 8 mm rebar slippage is chosen for final crack pattern visualization in Figure 46 because the patterns were stabilized at this stage.

Rebar pull-out stage	Specimen name		Values for strain in circular direction
	HyFRC-NC	HyFRC-C	Tensile strain
Peak bond stress			
8 mm of rebar slippage occurred			
Selected wider crack locations			Compressive strain
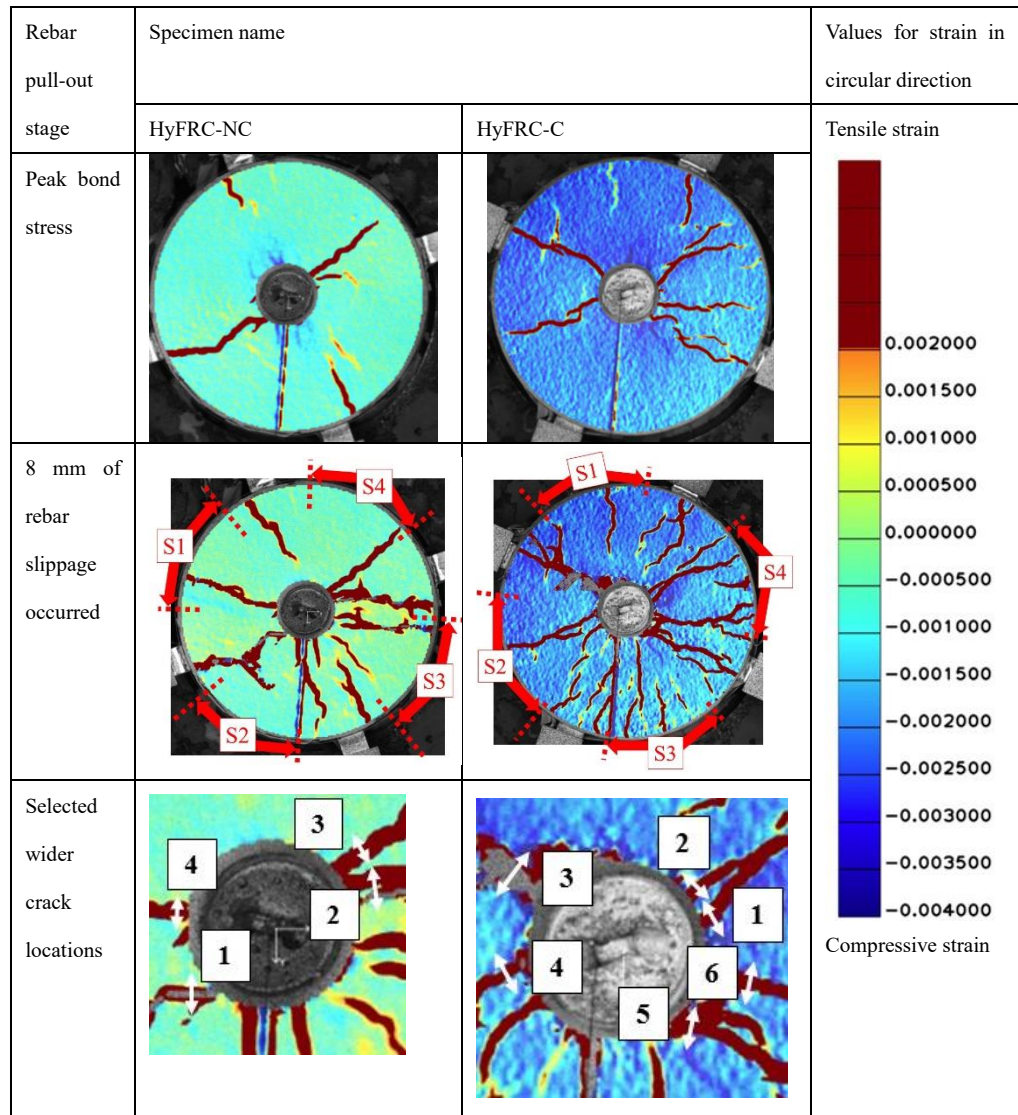
Figure 46: Crack pattern and strain in circular direction for ROI.

In order to understand the difference in behavior between the mid-height of the matrix and the top surface, the strains measured by the strain gauges are plotted in Figures 47a and 47b against normalized bond stress up to 500 and 6000 of micro strain respectively. Gauge lengths of strain

gauges on side 1, 2, 3, and 4 are indicated as S1, S2, S3, S4 in Figure 46 respectively. At the initial stages of loading, tensile strains developed in "M" strain gauges as expected because the circular tension stress is induced by bearing force between rebar ribs and matrix as discussed in section 1.2.1. Meanwhile, the compressive strain field developed on the ROI can be observed from "T" strain gauges, and the circular compressive strain field also occurred at later stages according to the strain maps in Figure 46. Such a compressive strain field may be induced by the non-uniform mechanical behavior along the specimen height. Because the rebar was pulled out downward during testing, a more intense tension stress in circular direction developed at lower bond regions compared to the top regions. In this case, the matrix in the lower bond regions expanded more in circular direction. Simultaneously, splitting cracks initiated from the bottom/middle bond regions and then propagated to the ROI at the top. Such non-uniform matrix deformation and crack opening along specimen height led to the measured compressive strain field in circular directions which only DIC is able to completely reveal.

When the bond stresses were approaching the peak values, widening of radial splitting cracks induced elongations in circular directions along the side surfaces of the cylindrical matrices. As a result, tensile strains in the middle height of the matrix increased more significantly (Figure 47a). Simultaneously, such circular elongation starts to overcome the compressive strain measured by the "T" strain gauges. Then, increasing tensile strains was measured by these "T" strain gauges. After peak bond stress, the circular matrix elongation in the middle bond region and the splitting crack development continued to be induced by the radial components of bearing forces between the exterior matrices and the rebar/matrix assemblages that slipped against the exterior matrices (Figure 17). Therefore, the circular tensile strains in Figure 47 kept increasing up to certain stages beyond the peak bond stresses.

According to Figure 46, reaching peak bond stress leads to 6 and 9 splitting cracks on HyFRC without and with spiral, respectively. After crack stabilization, 10 and 17 cracks are observed on the ROI of HyFRC without and with spiral respectively. Herein, using spiral in HyFRC increases the number of splitting cracks on the ROI at the top concrete surface. Such characteristics at the top bond region are different from the observation of the crack pattern in the middle bond region of d1 specimens which revealed the highest number of cracks in unconfined HyFRC (Table 8). The different crack characteristic at different height of the matrix is explained by a crack propagation process in vertical direction. The crack patterns from the saw cut sections infer that more splitting cracks may also develop in the middle bond region of d2 specimen with unconfined HyFRC matrix compared to the confined one. However, most of the cracks in unconfined HyFRC were very fine and only few of relatively wide cracks propagated upward to

the ROI by overcoming the compressive stress field in the top matrix. On the other hand, more cracks with moderate widths propagated to the ROI on the confined HyFRC. Note that such a characteristic in confined HyFRC doesn't represent a poorer crack resistance compared to the unconfined HyFRC because unconfined HyFRC actually has much wider cracks in few locations. In next section, such an issue will be discussed further with the DIC-measured crack widths.

In addition to the strains in circular direction, radial strains on top surfaces of different specimens were also obtained by DIC measurements. Such radial strains are compared in Figure 48 at three different stages, 10 MPa of normalized bond stress in the ascending bond stress-slippage curves, occurrence of peak bond stresses and 10 MPa of normalized bond stress in descending bond stress-slippage curves. These three stages are shown by a schematic example in Figure 49. The compressive stress-strain relation in Figure 24, which is obtained from the specimens made by a different batch of HyFRC material, can be used to convert the radial compressive strain on ROI (Figure 48) into radial compressive stress. The radial compressive stress in close vicinity of rebar can be identified and represents the value of normal compressive stress gripping the rebar. For example, -0.002 of strain on the color bar in Figure 48 is correspond to 33.76 MPa of compressive stress according to Figure 24. Note that the stress values identified by Figure 48 occurred on the top specimen surface and may be different to the values of stress that gripped the rebar in the middle bond region. However, Figure 48 still provides many insights into how matrices behave during rebar pull-out. On the top surface of unconfined HyFRC, the increment of radial compressive strain/stress before peak bond stress indicates increasing normal stress against the rebar. After peak bond stress, some reduction of such radial compressive strain/stress was observed. The top surface of spiral-confined HyFRC also exhibited increment of radial compressive strain/stress before peak bond stress. Because the spiral provided additional crack clamping behavior, such radial compressive strain/stress on confined HyFRC was more intense and represents higher rebar gripping stress compared to unconfined HyFRC. Herein, the radial strains obtained by DIC measurements visualize the rebar bond improvement mechanism provided by the spiral.

(a)

(b)
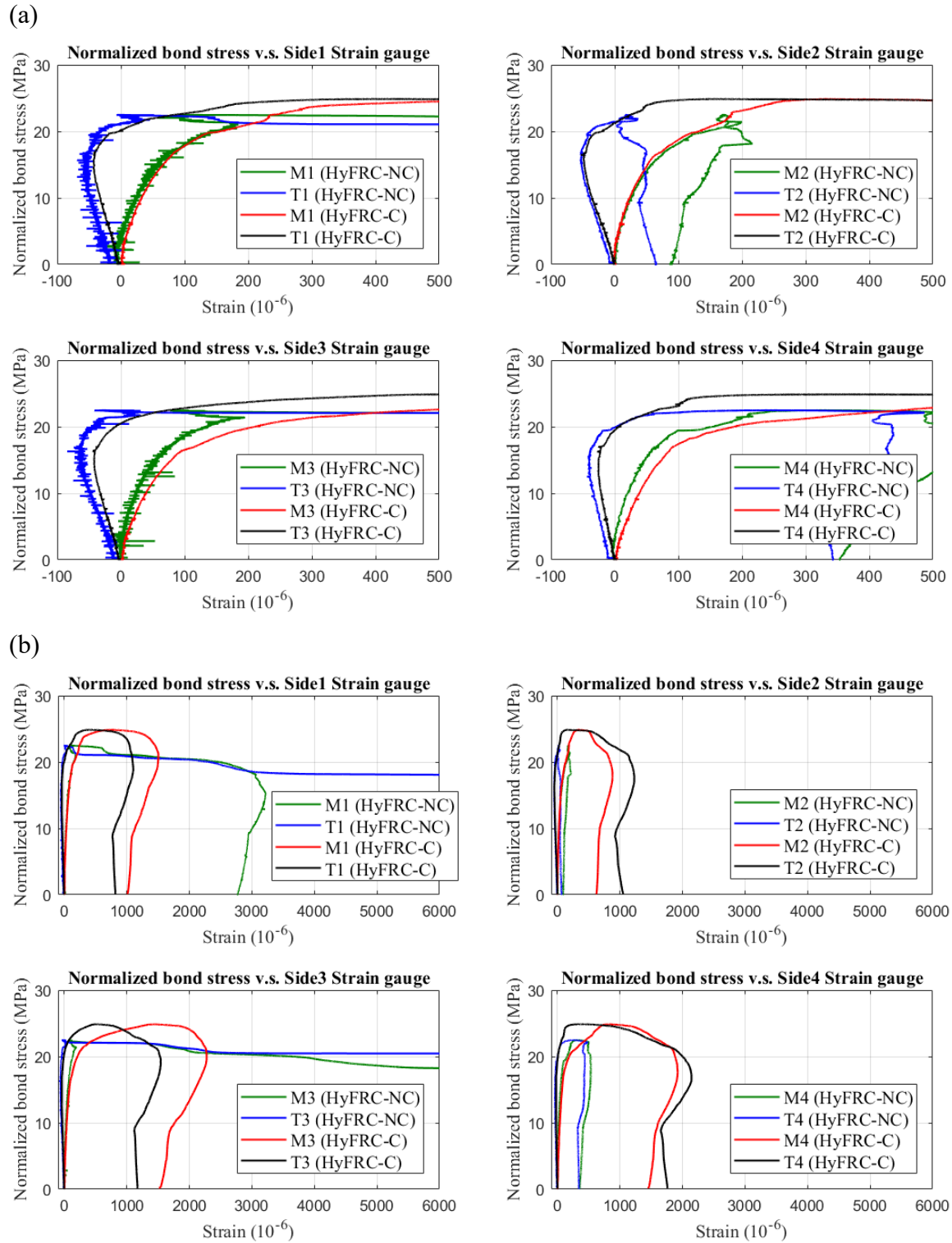
Figure 47: Strain-normalized bond stress relations in (a) initial stage (b) overall range

Rebar pull-out stage	Specimen name		Values for strain in radial direction
	HyFRC-NC	HyFRC-C	Tensile strain
10 MPa of normalized bond stress in ascending curve			
Peak bond stress			
10 MPa of normalized bond stress in descending curve			Compressive strain
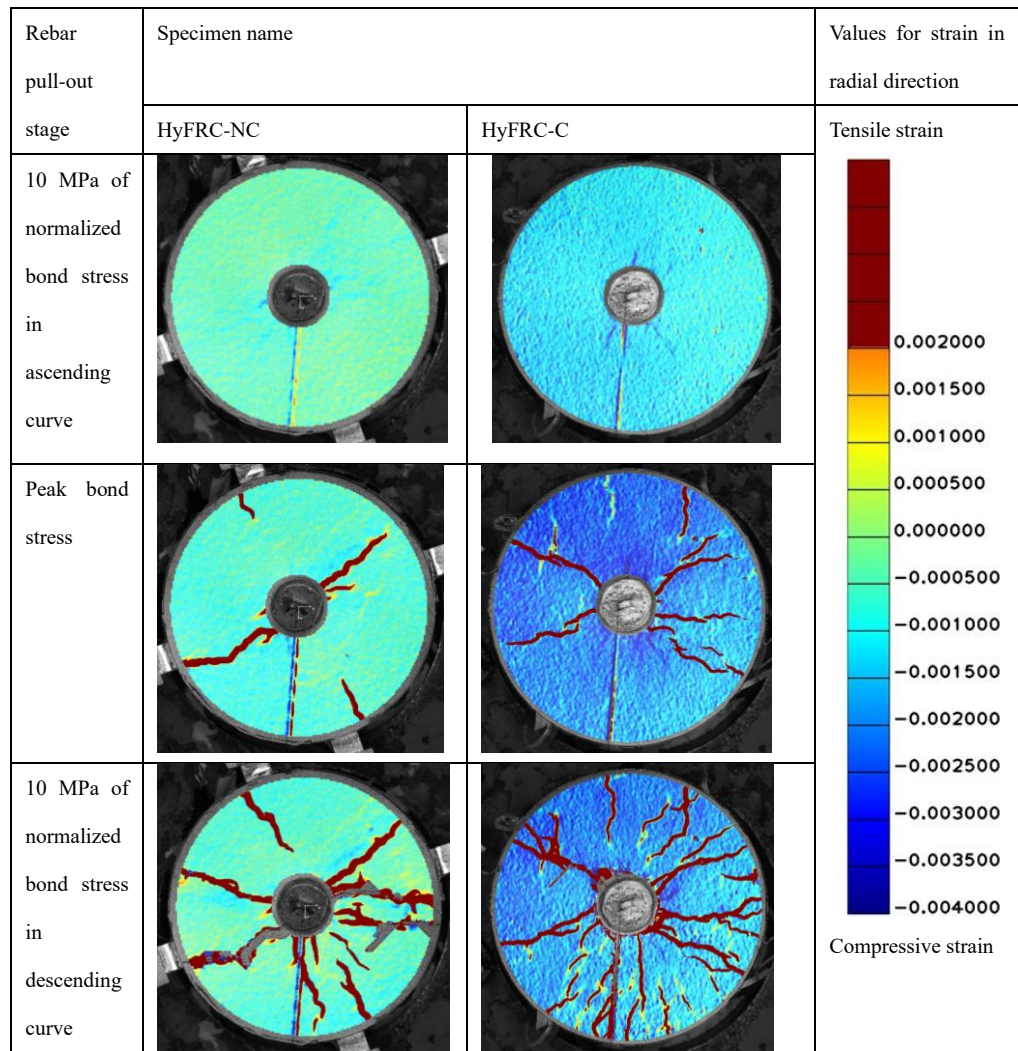
Figure 48: Strain in radial direction for ROI
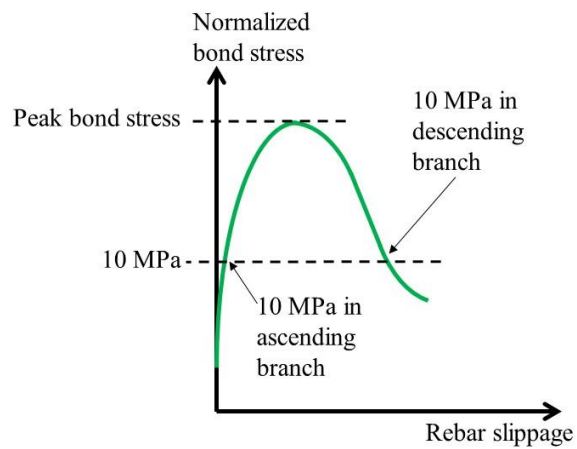
Figure 49: Schematic example showing stages corresponding for radial strain visualization

2.3.4.4   Crack width measurement for cracks on ROI

The crack widths closest to the rebars for individual splitting cracks on top surfaces are plotted against the rebar slippage in Figures 50a and 50b for the slippage below 3 and 8 mm respectively. The curves for wider cracks (final crack widths wider than 40 micron) are labeled in square boxes and the locations of labeled cracks are indicated in Figure 46. The solid points on the crack width-rebar slippage curves mark the data points correspond to peak bond stresses.

The crack width distributions for different specimens were quite different. At peak bond stress, unconfined HyFRC had crack 1 with a crack width as wide as 86 micron. 10 and 50 micron of crack width were measured for crack 2 and 3 which were about 180 degrees away from crack 1. In this case, the crack width didn't distribute uniformly and the crack openings mainly occurred at opposite side of the rebar. By clamping cracks, the spiral in HyFRC induced additional crack closure stress which led to a more uniform distribution of crack openings at peak bond stress. In this case, 5 cracks with crack widths ranging from 10 to 60 micron were measured on confined HyFRC and these cracks were off by around 15 to 60 degree from each other.

After the peak bond stress, the crack widths of crack 1 to 4 on unconfined HyFRC increased continuously. Fiber pull-out behavior is likely to be more dominant in crack 1 and 2 so more significant crack widening behavior occurred in these two cracks at opposite sides of the rebar. Eventually, their widths were as high as 600 micron. By clamping the HyFRC matrix, spiral made the crack width distribute in a more uniform manner and avoided the abrupt crack width increments after peak bond stress. In this case, all crack width can be controlled to be below 250 micron for confined HyFRC.

The more pronounced fiber pull-out in crack 1 and 2 of unconfined HyFRC matrix reduced the crack closure stress in these cracks and hence, led to reduction of radial compressive strain/stress on the top surface of such matrix after peak bond stress (Figure 48). However, these relatively wide cracks were still too fine to significantly decrease the rebar pull-out resistance in unconfined HyFRC. Therefore, the rebar pull-out performance improvement induced by spiral was not very pronounced (Figure 45) even if the spiral reinforcement exhibited good ability to control crack widths.

(a)

(b)
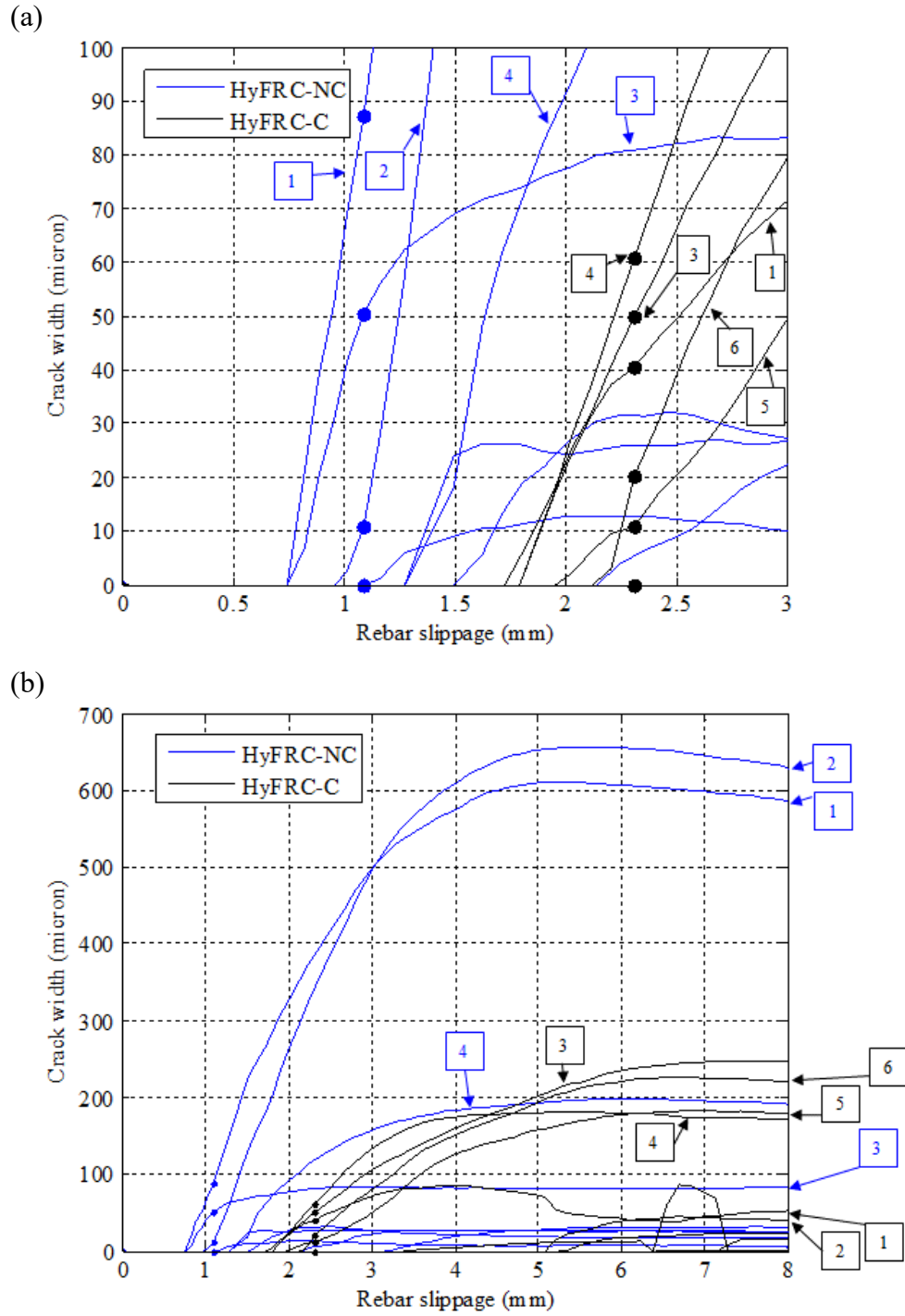
Figure 50: Individual crack width-rebar slippage curves in (a) Low slippage range (b) Overall slippage range

2.4   Vibration test series

2.4.1   Introduction

In order to support the rebar pull-out test results, vibration tests were performed for the d2 specimens with unconfined and spiral-confined HyFRC matrices at different rebar pull-out stages. Such tests investigate the effect of spiral to the bond damage in matrix around rebar.

During rebar pull-out, the slippage between rebar and matrix changed the rebar location so not only bond damage but also changed specimen configuration affected the natural frequencies. In order to understand the effect of specimen configuration, vibration tests were performed on undamaged specimens with different rebar locations. The results from such test series are used to differentiate the effects of changing rebar location and increased bond damage in regards to the natural frequencies.

An additional rebar pull-out specimen was made with artificial damage around the rebar which simulates a severely damaged bond region. The vibration test result for such a specimen is compared with the vibration test results for tested d2 specimens with common bond failure around rebars.

2.4.2   Test specimens, set-up and program

Hammer vibration tests were performed on rebar pull-out specimens with d2 dimensions as shown in Figure 51. As shown in Figure 40, the lengths of rebar sticking out from different sides of these specimens are called L_s and L_l. The specimens were hanging from a steel frame to isolate them from the ground. From the L_s end of the rebar, a hammer induced an axial impact force recorded by the data acquisition system and the longitudinal accelerations for the induced vibration were measured by an accelerometer attached at the L_l end of rebar.
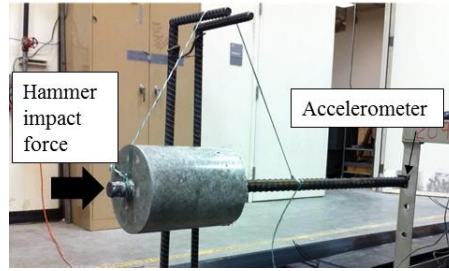
Figure 51: Hammer vibration test set-up

The vibration test program is summarized in Table 13. Specimens #1, 2 and 3 are the d2 specimens tested with the modified rebar pull-out test set-up reported previously. Their specimen dimensions, conditions and pull-out test results were provided in Figure 40 and Table 10 and 12. Their normalized bond stress-rebar slippage curves are shown in Figure 45.

Table 13: Summary of specimens for vibration test and test program

No.	Specimen name	Mixture	Spiral Volume fraction	Artificial damage	Casting configuration	Stages for performing vibration test
1	HyFRC-NC-d2-1	HyFRC	0%	No	c1	c1-untested c3-tested
2	HyFRC-NC-d2-2	HyFRC	0%	No	c1	c1-untested c2-tested c3-tested
3	HyFRC-C(0.75)-d2-1	HyFRC	0.75%	No	c1	c1-untested c3-tested
4	HyFRC-NC-d2-c1-undamaged	HyFRC	0%	No	c1	c1-untested
5	HyFRC-NC-d2-c3-undamaged	HyFRC	0%	No	c3	c3-untested
6	HyFRC-NC-d2-c3-damaged	HyFRC	0%	Yes	c3	c3-untested

Rebar pull-out not only induces bond damage but also changes the rebar location relative to the matrix. The location of rebar actually affects the vibration test result and hence, needs to be treated as an experimental parameter. In Table 13, the stages at which the vibration tests were performed are represented by two series of letters, and the first letter series indicates various rebar locations with different specimen configurations, c1, c2 and c3, as shown in Figure 52. Compared to c1, the rebar in configuration c2 and c3 has been shifted with Δs_1 and (Δs_1 +

Δs_2) of displacements, respectively. The second letter series following the letters for specimen configurations is either "untested" or "tested", and indicates whether a rebar pull-out test was performed or not. Take #2 specimen (HyFRC-NC-d2-2) as an example, it was casted in c1 configuration. Before rebar pull-out test, vibration test was conducted to it and the corresponding stage is called "c1-untested". After performing rebar pull-out tests, the rebar shifted and the configuration changed to c2 and then, c3. Figure 45a indicates the points on the normalized bond stress-rebar slippage curves that correspond to the stages for performing vibration tests. After pulling out the rebar in #2 specimen to different rebar slippage stages, the specimen was unload and vibration tests were conducted at stages referred as "c2-tested" and "c3-tested". #1 and 3 specimens were also casted in c1 configuration. For these specimens, the stages in which vibration tests were conducted are indicated in Figure 45a as well.

In order to investigate the effect of changing specimen configurations in regards to natural frequency, specimens #4 and 5 were cast with c1 and c3 configuration respectively. Other specimen dimensions and materials for these specimens are same as specimens #1 and 2. Vibration tests were performed on these specimens (#4 and 5) without any bond damage. Specimen # 6 was cast with identical specimen parameters as specimen #5 except that artificial bond damages were induced by packing sands between rebar ribs to simulate a completely crushed matrix as schematically shown in Figure 53. The thickness of the sand layer is close to but a little lower than the rib height, which is given in Table 3, to make sure that the rib is not completely covered by the sand layer. Vibration tests were performed to such an artificially damaged specimen to compare its vibration frequency with the frequencies from the specimens with common bond damages caused by rebar pull-out. After performing vibration tests on the artificially damaged specimen, rebar pull-out test was performed to that specimen to obtain its bond strength and bond stiffness, which is correspond to the slope of the ascending branch on bond stress-slippage curve. For compression tests, three of 102 mm by 203 mm cylinders were casted with same batch materials as specimens #4,5 and 6.
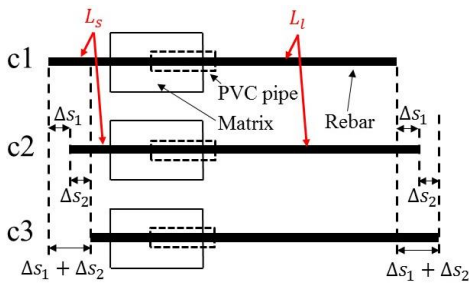
Figure 52: Specimen configurations   Figure 53: Artificial damage around rebar
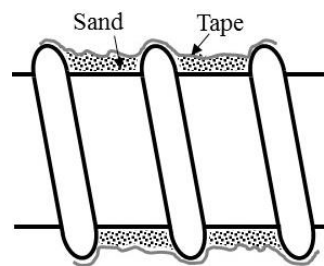
2.4.3 Data processing method and test results interpretation

The frequency spectrums of vibrations can be obtained by performing Fast Fourier Transform (FFT) to the measured accelerations. Figure 54 shows the spectrum for HyFRC-NC-d2-2 specimen at c1-untested and c3-tested stage as an example. The frequency values that correspond to the peak amplitudes are interpreted as natural frequencies of the system.
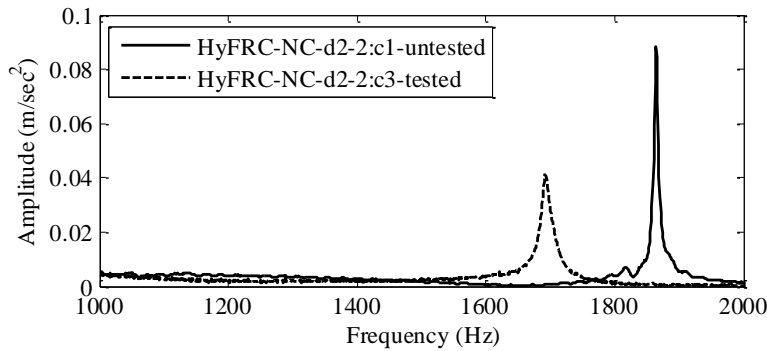
Figure 54: Response spectrum for acceleration of HyFRC-NC specimen

The results for the vibration test program are summarized in Table 14. Extra care was taken during casting to keep the L_s and L_l end length the same at c1 and c3 configurations to provide consistent results among the different specimens.

After conducting rebar pull-out tests for specimens #1,2 and 3, the combination of bond damage and change in rebar location always caused a frequency shift towards lower frequency. On the other hand, the test results of specimens #4 and 5 indicate that changing the rebar location from c1 to c3 without bond damage leads to a smaller frequency shift. Therefore, bond damage due to rebar pull-out is responsible for the reduction in frequency in specimens #1,2 and 3.

By subtracting the natural frequency of "HyFRC-NC-d2-c3-undamaged" (i.e. specimen #5 which is a representative specimen for the "c3-untested" stage) from the frequencies of specimens #1,2 and 3 at "c3-tested" stage, the portion of frequency decrease that was induced by bond damage only can be determined and are listed in Table 15. Similarly, the frequency difference between "HyFRC-NC-d2-c3-undamaged" (specimen #5) and "HyFRC-NC-d2-c3-damaged" (specimen #6) specimens represents the decrease in frequency induced by the artificial bond damage and the associated frequency decrease is also shown in Table 15.

56

Table 14: Results summary of vibration test program

No.	Specimen name	Compressive strength (MPa)	Rebar pull-out stages for vibration test	L_s (mm)	L_l (mm)	Natural frequency (Hz)
1	HyFRC-NC-d2-1		c1-untested	38.1	609.6	1855
			c3-tested	9.525	638.2	1754
2	HyFRC-NC-d2-2	41.2	c1-untested	38.1	611.2	1864
			c2-tested	30.2	619.1	1782~1783
			c3 tested	9.327	641.4	1691~1692
3	HyFRC-C(0.75)-d2-1		c1-untested	38.1	611.2	1847
			c3-tested	10.12	642.1	1723~1724
4	HyFRC-NC-d2-c1-undamaged		c1-untested	38.1	608.0	1868
5	HyFRC-NC-d2-c3-undamaged	37.3	c3-untested	9.525	635.0	1812
6	HyFRC-NC-d2-c3-damaged		c3-untested	9.525	635.0	280~326

Table 15: Shifting of natural frequency due to bond damage at c3 configuration

No.	Specimen name	Frequency shift induced by bond damage only (Hz)	Bond damage type	Residual bond strength (MPa)	Residual bond stiffness (MPa/mm)
1	HyFRC-NC-d2-1	1754-1812 = -58	Common bond damage induced by rebar pull-out	4.6	N/A
2	HyFRC-NC-d2-2	1691-1812= -121		1.5	Higher than 15.1
3	HyFRC-C(0.75)-d2-1	1724-1812-= -88		5.3	Higher than 15.1
6	HyFRC-NC-d2-c3-damaged	-1486 ~ -1532	Artificial bond damage	0.3	0.12

Residual bond strength/stiffness for rebar pull-out specimens at c3 configuration are summarized in Table 15. The methods of obtaining such residual bond strength/stiffness are similar to that reported in [49] and is explained as follows. For specimens #2 and 3, the residual bond strengths correspond to the bond strength before entering the unloading curves at c3-tested stages indicated in Figure 45a and the residual bond stiffness are obtained from the slopes of such unloading curves. Both specimens #2 and 3 (i.e. unconfined and confined HyFRC specimens) exhibit similar unloading curves and the slopes/stiffness are always higher than 15.1 MPa/mm. For specimen #1, the residual bond strength is obtained in same manner as specimens #2 and 3 while the residual bond stiffness is not available. The residual bond stiffness of the specimen #1

is expected to be similar to the stiffness of specimen #2 because both specimens were made with unconfined HyFRC matrices. The residual bond strength of the #6 specimen (specimen with artificial bond damage) is obtained from its peak bond stress for rebar pull-out and the residual bond stiffness of such a specimen is correspond to the slop of bond stress-slippage curves in the beginning of loading.

2.4.4   Discussion of test results

In Table 15, the frequency shift induced by rebar pull-out failure in specimen #3 (a spiral-confined HyFRC specimen) is within the frequency shift range induced by the failure mode of specimens #1 and 2 (unconfined HyFRC specimens). In this case, the shearing and crushing failures in the bond regions of unconfined and confined HyFRC are too similar for vibration test to differentiate.

According to [49], the residual bond strength/stiffness in the rebar pull-out specimens are expected to be positively related to the rebar vibration frequency which is an indicator of system stiffness. The lowest value of residual bond strength/stiffness was observed for the artificial damage specimen #6. This specimen also had the lowest frequency of all specimens given in Table 14. The low frequency is a result of the large frequency shift induced by the artificial bond damage. On the other hand, the far less frequency shifts of specimens #1, 2 and 3 in Table 15 are induced by rebar pull-out damage. Hence pull-out damage is far less severe compared to the artificial bond damage. From Figure 55, many uncrushed matrix regions could be identified on the bond region of the rebar pulled out from unconfined and spiral-confined HyFRC matrix. Instead of causing the matrix to crush as what simulated by the artificial bond damage, the shear failure of frictional rebar pull-out only partially crushes and cracks the matrix around the rebar. Therefore, the frequency decrease induced by rebar pull-out is less significant.

In the literature, pre-stress in rock bolt led to increment of its vibration frequency by closing cracks around the bolt [51]. In the rebar pull-out specimens, the rebar gripping force mobilized by rebar slippages may play a similar role. In the specimens with frictional pull-out failure, the rebar gripping force increase the system stiffness by closing cracks and compacting materials in the bond region. However, the different intensities of the rebar gripping forces in unconfined and confined HyFRC matrices cannot be differentiated due to their similarities in natural frequencies at the c3-tested stage. On the other hand, the vibration tests were performed on the specimen with artificial damage at c3-untested stage (a stage before inducing any rebar slippage) so the

obtained frequency represents a state without rebar gripping force. The much lower natural frequency in the artificial damaged specimen is expected because the material compacting behavior provided by rebar gripping force didn't occur in such a specimen to increase its stiffness.
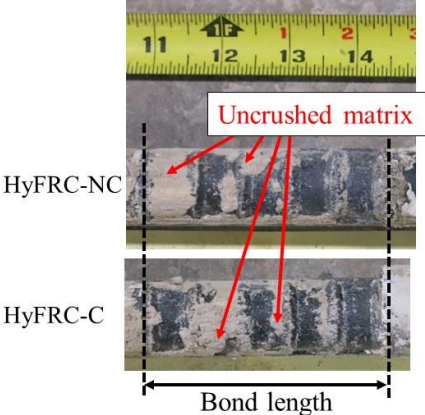
Figure 55: Bond region on rebar after pull-out

3   Single fiber pull-out test series

3.1   Introduction

Single fiber pull-out tests were carried out to study the micro/macro fiber synergies in HyFRC. By pulling out a macro hooked-end steel fiber from a cementitious matrix with and without PVA microfibers, one can investigate if the microfiber reinforcement enhances the bond behavior of a macrofiber and hence, leads to a higher crack resisting ability for a macrofiber in a HyFRC. As mentioned in Chapter 1, one of the research topics in this thesis focuses on replacing cement with supplementary materials, fly ash and slag, to reduce the environmental impact from concrete mixtures. Therefore, the effect of such type of replacement in macrofiber bond performance and in the effectiveness of microfibers in improving such performance is also investigated by fiber pull-out tests. The pozzolanic reaction from slag and fly ash may densify the steel macrofibers/matrix interface and hence, may improve its bond resistance. In addition, some fiber pull-out specimens were made by ultra-high strength concrete with and without steel microfiber reinforcement to investigate the degree of micro/macro fiber interaction in extremely strong matrix. Although the HyFRC mixture for rebar pull-out test only incorporates a relatively small amount of PVA microfibers, some of the fiber pull-out tests incorporate a higher microfiber dosage to highlight the effect of microfibers on enhancing the macrofiber pull-out resistance.

3.2   Specimen preparation

3.2.1   Material for matrix and mixing

A kitchen mixer was used for mixing fresh material for the matrix of single fiber pull-out specimens. The mixtures and moisture curing ages for the typical mortars under investigation are shown in Table 16. The following notation was used for the single fiber pull-out samples listed in Table 16: M stands for mortar matrix; the first letters in parenthesis represent the sand type which is either Vulcan sand (VS) or silica sand (SS). The Valcun sand was also utilized in the rebar pull-out specimens with HyFRC matrices. Properties of this type of sand are specified in section 2.2.2. The silica sand has a particle size of 60 to 80 micron. The second set of letters in parenthesis indicate the weight fraction of cement, fly ash, or fly ash and slag, respectively. For

example, "55FA" indicates that 55% of cement was replaced by fly ash; "15FA-45S" means that 15% and 45% of cement were replaced by fly ash and slag, respectively; "Ord." indicates that 0% of cement has being replaced. The w/c ratio is shown next and is either 0.54 or 0.28. The moist curing times "2w" or "4w" indicate 2 weeks and 4 weeks of moist curing, respectively. The PVA fiber volume percentages are given last and are either 0% (denoted as NF), 0.29% or 2%. Note the PVA fibers used for fiber pull-out specimens are the PVA-1 fibers, which was also used in the HyFRC matrix for rebar pull-out specimens. The properties of the such microfibers were given in Table 2. The PVA-fiber-reinforced M(VS,Ord.) samples (i.e. M(VS,Ord.)-0.54-2w-0.29%PVA and M(VS,Ord.)-0.54-4w-0.29%PVA) in Table 16 contain the same PVA fiber volume percentage as the PVA volume percentage in the mortar portion of the HyFRC. Furthermore, such M(VS,Ord.) sample was specifically designed to have the same material proportions (i.e. cement, fine aggregates and water) as the mortar portion of the HyFRC. Hence, the effect of 0.29% of PVA fibers on the pull-out resistance of the steel macrofiber can be directly correlated to the rebar pull-out tests of HyFRC specimens as will be discussed in section 3.5.4.

In addition to the conventional mortar mixtures shown in Table 16, matrices for fiber pull-out specimens were also made with an ultrahigh performance mortar mix shown in Table 17 to investigate the effect of steel microfibers on the pull-out resistance of the steel macrofiber. The ultrahigh performance material, denoted as "UHPC" in Table 17 represents a matrix mixture modified from the material proportions in the literature for an ultra-high performance fiber reinforced concrete (UHPFRC) [67]. The UHPC mixture was used to study the effect of steel microfibers and extremely high matrix strength on steel macrofiber pull-out resistance. Such mixture provides sufficient viscosity to prevent segregation of the fibers during mixing. In this case, the UHPC matrices were made with 3% micro steel fiber (12 mm of length and 80 of aspect ratio) for UHPFRC matrices and also made without such micro fibers for control matrices. The sands used in such matrices consist of coarse and fine sands with a coarse/fine sand weight ratio selected as 2. The median particle size of coarse sand, fine sand and the glass powder are 460, 150 and 1.8 micron respectively. The UHPC mixture utilizes grading of many types of small particles to obtain very dense packing. High strength of such a material corresponds to the low w/c ratio and minimum defects provided by such a packing.

Table 16: Mix design for matrix of single fiber pull-out specimens

Mix design name	Type II-V cement	Type F fly ash	Slag	Sand	Water	SP	VMA	Vol. % of PVA-1 fiber	Curing age
	Unit: kg/m^3								
M(VS,Ord.)-0.54-2w-NF	611.4	0	0	1232.9	330.2	0	0	0	2 weeks
M(VS,Ord.)-0.54-2w-0.29%PVA	609.6	0	0	1229.3	329.2	0	0	0.29	2 weeks
M(VS,Ord.)-0.54-4w-NF	611.4	0	0	1232.9	330.2	0	0	0	4 weeks
M(VS,Ord.)-0.54-4w-0.29%PVA	609.6	0	0	1229.3	329.2	0	0	0.29	4 weeks
M(SS,Ord.)-0.28-2w-NF	1357.2	0	0	409.6	371.3	9.20	4.52	0	2 weeks
M(SS,Ord.)-0.28-2w-2%PVA	1357.5	0	0	357.2	365.7	12.04	7.10	2	2 weeks
M(SS,Ord.)-0.28-4w-NF	1359.0	0	0	410.2	371.8	8.33	4.04	0	4 weeks
M(SS,Ord.)-0.28-4w-2%PVA	1359.3	0	0	357.7	366.2	11.16	6.66	2	4 weeks
M(SS,55FA)-0.28-2w-NF	558.1	669.3	0	409.7	338.8	5.90	2.83	0	2 weeks
M(SS,55FA)-0.28-2w-2%PVA	556.2	667.0	0	356.0	333.7	9.99	5.96	2	2 weeks
M(SS,55FA)-0.28-4w-NF	557.2	668.2	0	409.1	338.2	7.50	2.82	0	4 weeks
M(SS,55FA)-0.28-4w-2%PVA	558.9	670.3	0	357.8	335.3	7.55	3.58	2	4 weeks
M(SS,15FA-45S)-0.28-2w-NF	509.0	190.9	572.6	409.7	349.1	7.87	3.72	0	2 weeks
M(SS,15FA-45S)-0.28-2w-2%PVA	509.3	190.9	572.9	357.5	342.9	10.85	6.48	2	2 weeks
M(SS,15FA-45S)-0.28-4w-NF	510.2	191.4	574.1	410.8	350.0	6.11	2.92	0	4 weeks
M(SS,15FA-45S)-0.28-4w-2%PVA	509.0	190.8	572.5	357.0	346.1	9.13	5.53	2	4 weeks

Note:

- SP (Superplasticizer): Glenium 7500
- VMA (Viscosity-Modifying Admixture): Rheomac 362

Table 17: Mixture for UHPC

Mixture	Type II-V Cement	Type F fly ash	Silica fume	Sand	Glass powder	Water	SP	Vol. % of micro steel fiber
	Unit: kg/m^3							
UHPC-0.25-NF	866.0	86.61	216.5	779.4	216.5	251.4	57.8	0
UHPC-0.25-3%MSF	840.0	84.01	210.0	756.0	210.0	243.9	56.0	3

Note:

- SP (Superplasticizer): Grace Cast 575

To sum up, different types of matrices, were made without and with micro fibers. In later sections, the matrix/specimen without micro fiber reinforcement will be referred as an unreinforced matrix/specimen and the matrix/specimen reinforced by micro fibers will be referred as a reinforced matrix/specimen.

3.2.2 Specimen dimension and condition

The specimens consist of a 60 mm hooked-end steel fiber (denoted as SF-1 in Table 2 and Figure 18), embedded along the central axis of a cylindrical cementitious matrix with 38 mm diameter and 38 mm height as shown in Figure 56. The same hooked–end steel fiber was used in the HyFRC rebar pull-out specimens. The molds for casting fiber pull-out specimens are shown in Figures 57 and 58. These molds serve to position the steel fiber and aligned it with the central axis of the cylindrical matrix. Consistent embedment lengths (19.2 ± 0.5 mm) for hooked-end steel fibers were used. During casting, the fresh material was pour into the molds and a vibration table was used to achieve compaction. In addition to the single fiber pull-out specimens, 51x51x51 mm cubes and 51x102 mm cylinders were casted for compressive tests and splitting tensile tests, respectively.
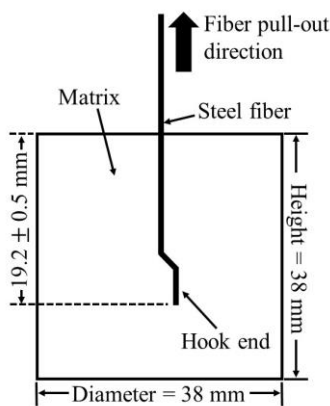
Figure 56: Side view of single fiber pull-out specimen
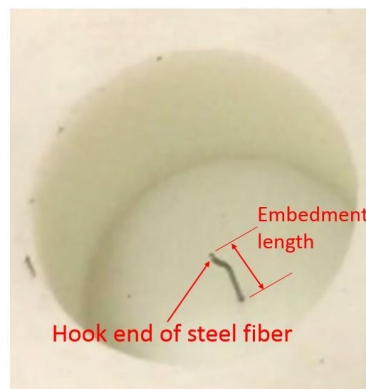
Figure 57: Mold for single fiber pull-out specimen

Figure 58: Casting of single fiber pull-out specimen

All types of specimens, including the single fiber pull-out, compression, and splitting tension specimens with M matrices were cured in fog room for a period indicated in Table 16 and were tested right after such moisture curing. The fiber pull-out specimens with M matrices were wrapped with plastic wrap during testing to prevent drying shrinkage. On the other hand, drying

shrinkage of the UHPC specimen is very small and can be ignored [68]. The UHPC specimens were kept in air-dry condition after 14 days of moisture curing, and were tested 98 days after casting.

3.3 Testing procedure

A 267 kN (60 kip) capacity universal testing machine (UTM 60) was used to perform the single fiber pull-out test and the test set-up is shown in Figure 59 and 60. In order to fix the specimen, the bottom matrix face was glued to a bottom plate by epoxy. Such a support condition was used in the literature to simulate a more realistic stress field around fiber when it is bridging a crack [33]. A grip clamped and pulled out the steel fiber when the upper machine head moved upward. A displacement rate between 0.01 and 0.03 mm/sec was chosen. A load cell was coupled with the grip to measure the applied axial load; the fiber displacement during pull-out was measured by a potentiometer.
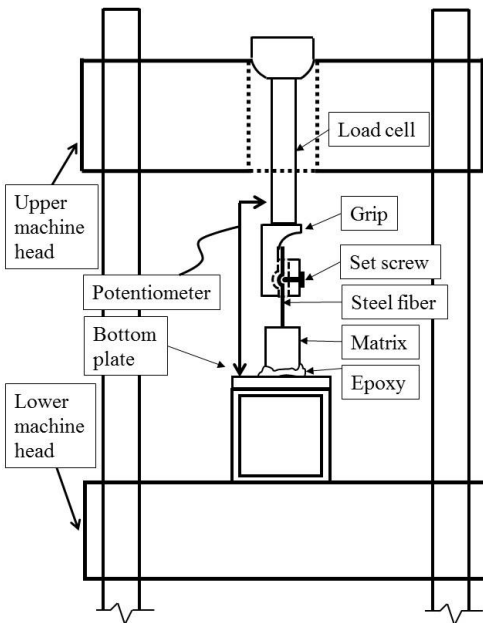
Figure 59: Overall view of single fiber pull-out test set-up

Figure 60: Close view of single fiber pull-out test set-up for the specimen glued to a steel plate.

In order to obtain matrix compressive strengths, standard compressive tests were performed for the 51x51x51 mm cube specimens with 1334 N/sec as loading rate. Splitting tension tests were performed for the 51x102 mm cylinders to evaluate the tensile characteristic according to ASTM C496 except that the tensile resistances are represented by splitting tension stress correspond to initiation of first visible crack rather than the ultimate splitting tension stress because the test set-up resisted the specimen to be split apart right after tensile failure and made the ultimate stress unrepresentative.

3.4   Test result

3.4.1   Results of mechanical testing

The test results for specimens with M(VS,Ord.), M(SS,Ord.), M(SS,55FA), M(SS,15FA-45S) and UHPC matrices are summarized in Table 18, 19, 20, 21 and 22, respectively. In general, test results from two compressive tests and two splitting tensile tests are used to measure the listed averaged compressive strengths (f_c') and averaged splitting tension stresses at first crack initiations $(f_{t,cr})$, respectively, but some exceptions are described by the notes below Table 20 and 21.

Because the $f_{t,cr}$ values are determined by observation for the crack development on specimen surfaces, such values are affected by different crack development processes in different specimens and are only used to characterize the tensile resistance of matrices in an approximate manner. On the other hand, the f_c' values are used as main parameters to represent matrix strengths for the discussions in later sections. According to the test results for all specimen types, using micro fiber reinforcement always increases the value of $f_{t,cr}$ of the matrix. The test results also show that increasing curing age from 2 to 4 weeks for M matrices leads to increase of f_c' values for same matrix type except for the M(SS,15FA-45S)-0.28-NF matrix, of which the f_c' at 2 week curing age is not available. However, it is reasonable to assume that a longer curing age also leads to increase of f_c' for such M(SS,15FA-45S)-0.28-NF matrix.

Table 18: Test results of specimen with M(VS,Ord.) matrix

	Mechanical test results		Fiber pull-out test results			
Specimen name	Average f_c' (MPa)	Average $f_{t,cr}$ (MPa)	Peak load (N)	Average peak load (N)	Fiber displacement at peak load (mm)	Average fiber displacement at peak load (mm)
M(VS,Ord.)-0.54-2w-NF-1	37.46	4.40	311.4	289.6	0.96	0.95
M(VS,Ord.)-0.54-2w-NF-2			310.7		0.93	
M(VS,Ord.)-0.54-2w-NF-3			315.9		1.04	
M(VS,Ord.)-0.54-2w-NF-4			254.0		0.88	
M(VS,Ord.)-0.54-2w-NF-5			256.2		0.96	
M(VS,Ord.)-0.54-2w-0.29%PVA-1	38.58	4.69	271.8	295.1	0.96	0.98
M(VS,Ord.)-0.54-2w-0.29%PVA-2			306.7		0.88	
M(VS,Ord.)-0.54-2w-0.29%PVA-3			287.6		1.02	
M(VS,Ord.)-0.54-2w-0.29%PVA-4			315.1		1.16	
M(VS,Ord.)-0.54-2w-0.29%PVA-5			294.3		0.89	
M(VS,Ord.)-0.54-4w-NF-1	43.41	5.30	330.3	334.6	0.89	0.89
M(VS,Ord.)-0.54-4w-NF-2			340.2		0.86	
M(VS,Ord.)-0.54-4w-NF-3			338.4		0.95	
M(VS,Ord.)-0.54-4w-NF-4			331.9		0.83	
M(VS,Ord.)-0.54-4w-NF-5			325.5		0.88	
M(VS,Ord.)-0.54-4w-NF-6			341.5		0.91	
M(VS,Ord.)-0.54-4w-0.29%PVA-1	45.73	5.50	329.5	339.2	0.79	0.87
M(VS,Ord.)-0.54-4w-0.29%PVA-2			324.3		0.87	
M(VS,Ord.)-0.54-4w-0.29%PVA-3			325.4		0.89	
M(VS,Ord.)-0.54-4w-0.29%PVA-4			380.1		0.97	
M(VS,Ord.)-0.54-4w-0.29%PVA-5			333.5		0.84	
M(VS,Ord.)-0.54-4w-0.29%PVA-6			342.7		0.84	

Table 19: Test results of specimen with M(SS,Ord.) matrix

	Mechanical test results		Fiber pull-out test results			
Specimen name	Average f_c' (MPa)	Average $f_{t,cr}$ (MPa)	Peak load (N)	Average peak load (N)	Fiber displacement at peak load (mm)	Average fiber displacement at peak load (mm)
M(SS,Ord.)-0.28-2w-NF-1	60.12	4.48	355.1	369.9	0.72	0.73
M(SS,Ord.)-0.28-2w-NF-2			372.7		0.82	
M(SS,Ord.)-0.28-2w-NF-3			372.1		0.70	
M(SS,Ord.)-0.28-2w-NF-4			367.0		0.64	
M(SS,Ord.)-0.28-2w-NF-5			362.1		0.72	
M(SS,Ord.)-0.28-2w-NF-6			390.3		0.76	
M(SS,Ord.)-0.28-2w-2%PVA-1	69.59	8.98	390.7	409.1	1.02	0.84
M(SS,Ord.)-0.28-2w-2%PVA-2			397.3		0.77	
M(SS,Ord.)-0.28-2w-2%PVA-3			410.8		0.93	
M(SS,Ord.)-0.28-2w-2%PVA-4			422.7		0.81	
M(SS,Ord.)-0.28-2w-2%PVA-5			433.2		0.78	
M(SS,Ord.)-0.28-2w-2%PVA-6			400.0		0.74	
M(SS,Ord.)-0.28-4w-NF-1	65.20	4.76	<u>379.5</u>	370.0	<u>0.74</u>	0.80
M(SS,Ord.)-0.28-4w-NF-2			356.3		0.85	
M(SS,Ord.)-0.28-4w-NF-3			371.4		0.76	
M(SS,Ord.)-0.28-4w-NF-4			416.0		0.73	
M(SS,Ord.)-0.28-4w-NF-5			326.4		0.70	
M(SS,Ord.)-0.28-4w-NF-6			379.8		0.94	
M(SS,Ord.)-0.28-4w-2%PVA-1	79.75	11.51	<u>425.3</u>	448.65	<u>0.67</u>	0.97
M(SS,Ord.)-0.28-4w-2%PVA-2			452.8		1.28	
M(SS,Ord.)-0.28-4w-2%PVA-3			<u>354.1</u>		<u>5.66</u>	
M(SS,Ord.)-0.28-4w-2%PVA-4			444.5		0.66	
M(SS,Ord.)-0.28-4w-2%PVA-5			<u>296.8</u>		<u>5.80</u>	
M(SS,Ord.)-0.28-4w-2%PVA-6			<u>343.0</u>		<u>1.90</u>	

Table 20: Test results of specimen with M(SS,55FA) matrix

	Mechanical test results		Fiber pull-out test results			
Specimen name	Average f_c' (MPa)	Average $f_{t,cr}$ (MPa)	Peak load (N)	Average peak load (N)	Fiber displacement at peak load (mm)	Average fiber displacement at peak load (mm)
M(SS,55FA)-0.28-2w-NF-1	39.88	2.96	346.2	342.2	0.89	0.87
M(SS,55FA)-0.28-2w-NF-2			313.6		0.88	
M(SS,55FA)-0.28-2w-NF-3			355.2		0.95	
M(SS,55FA)-0.28-2w-NF-4			322.1		0.81	
M(SS,55FA)-0.28-2w-NF-5			356.9		0.84	
M(SS,55FA)-0.28-2w-NF-6			358.9		0.87	
M(SS,55FA)-0.28-2w-2%PVA-1	36.09	6.36	383.8	385.7	0.60	0.66
M(SS,55FA)-0.28-2w-2%PVA-2			355.8		0.92	
M(SS,55FA)-0.28-2w-2%PVA-3			386.9		0.59	
M(SS,55FA)-0.28-2w-2%PVA-4			426.2		0.57	
M(SS,55FA)-0.28-2w-2%PVA-5			375.2		0.65	
M(SS,55FA)-0.28-2w-2%PVA-6			386.4		0.61	
M(SS,55FA)-0.28-4w-NF-1	43.41	3.64	344.9	331.0	0.67	0.78
M(SS,55FA)-0.28-4w-NF-2			351.3		0.95	
M(SS,55FA)-0.28-4w-NF-3			348.6		0.90	
M(SS,55FA)-0.28-4w-NF-4			289.8		0.71	
M(SS,55FA)-0.28-4w-NF-5			<u>357.6</u>		<u>0.62</u>	
M(SS,55FA)-0.28-4w-NF-6			320.7		0.69	
M(SS,55FA)-0.28-4w-2%PVA-1	52.02	7.08	306.3	341.8	0.72	0.68
M(SS,55FA)-0.28-4w-2%PVA-2			334.2		0.62	
M(SS,55FA)-0.28-4w-2%PVA-3			334.7		0.67	
M(SS,55FA)-0.28-4w-2%PVA-4			357.2		0.73	
M(SS,55FA)-0.28-4w-2%PVA-5			361.6		0.58	
M(SS,55FA)-0.28-4w-2%PVA-6			357.1		0.75	

Note: The average $f_{t,cr}$ for M(SS,55FA)-0.28-2w-2%PVA specimen is obtained from only one specimen because the result of another specimen is not available.

Table 21: Test results of specimen with M(SS,15FA-45S) matrix

Specimen name	Mechanical test results		Fiber pull-out test results			
	Average f_c' (MPa)	Average $f_{t,cr}$ (MPa)	Peak load (N)	Average peak load (N)	Fiber displacement at peak load (mm)	Average fiber displacement at peak load (mm)
M(SS,15FA-45S)-0.28-2w-NF-1	N/A	5.11	368.6	329.7	0.75	0.76
M(SS,15FA-45S)-0.28-2w-NF-2			332.9		0.75	
M(SS,15FA-45S)-0.28-2w-NF-3			322.9		0.81	
M(SS,15FA-45S)-0.28-2w-NF-4			333.2		0.76	
M(SS,15FA-45S)-0.28-2w-NF-5			298.1		0.65	
M(SS,15FA-45S)-0.28-2w-NF-6			322.6		0.81	
M(SS,15FA-45S)-0.28-2w-2%PVA-1	47.54	8.01	395.4	383.5	0.71	0.68
M(SS,15FA-45S)-0.28-2w-2%PVA-2			388.1		0.61	
M(SS,15FA-45S)-0.28-2w-2%PVA-3			380.7		0.73	
M(SS,15FA-45S)-0.28-2w-2%PVA-4			392.7		0.70	
M(SS,15FA-45S)-0.28-2w-2%PVA-5			360.3		0.66	
M(SS,15FA-45S)-0.28-2w-2%PVA-6			<u>408.5</u>		<u>0.55</u>	
M(SS,15FA-45S)-0.28-4w-NF-1	53.14	5.06	452.0	467.9	0.77	0.77
M(SS,15FA-45S)-0.28-4w-NF-2			463.5		0.79	
M(SS,15FA-45S)-0.28-4w-NF-3			503.3		0.90	
M(SS,15FA-45S)-0.28-4w-NF-4			487.9		0.72	
M(SS,15FA-45S)-0.28-4w-NF-5			416.6		0.71	
M(SS,15FA-45S)-0.28-4w-NF-6			484.3		0.76	
M(SS,15FA-45S)-0.28-4w-2%PVA-1	71.91	8.44	473.4	457.8	0.53	0.61
M(SS,15FA-45S)-0.28-4w-2%PVA-2			442.3		0.62	
M(SS,15FA-45S)-0.28-4w-2%PVA-3			477.8		0.65	
M(SS,15FA-45S)-0.28-4w-2%PVA-4			441.7		0.56	
M(SS,15FA-45S)-0.28-4w-2%PVA-5			454.3		0.67	
M(SS,15FA-45S)-0.28-4w-2%PVA-6			457.1		0.66	

Note: The average f_c' for M(SS,15FA-45S)-0.28-2w-2%PVA specimen is obtained from only one specimen because the result of another specimen is not available.

Table 22: Test results of specimen with UHPC matrix

Specimen name	Mechanical test results		Fiber pull-out test results			
	Average f_c' (MPa)	Average $f_{t,cr}$ (MPa)	Peak load (N)	Average peak load (N)	Fiber displacement at peak load (mm)	Average fiber displacement at peak load (mm)
UHPC-0.25-NF-1	86.30	7.53	455.4	443.9	0.53	0.59
UHPC-0.25-NF-2			467.4		0.57	
UHPC-0.25-NF-3			426.2		0.62	
UHPC-0.25-NF-4			<u>495.5</u>		<u>0.83</u>	
UHPC-0.25-NF-5			426.4		0.65	
UHPC-0.25-3%MSF-1	146.76	N/A	442.1	447.4	0.49	0.60
UHPC-0.25-3% MSF-2			443.4		0.62	
UHPC-0.25-3% MSF-3			<u>518.7</u>		<u>0.65</u>	
UHPC-0.25-3% MSF-4			440.0		0.54	
UHPC-0.25-3% MSF-5			464.2		0.74	

In some of the fiber pull-out specimens (M(SS,Ord.)-0.28-4w-NF-1, M(SS,Ord.)-0.28-4w-2%PVA-1, M(SS,55FA)-0.28-4w-NF-5, M(SS,15FA-45S)-0.28-2w-2%PVA-6, UHPC-0.25-NF-4 and UHPC-0.25-3% MSF-3), the steel macrofibers fractured during testing. No. 3, 5 and 6 of M(SS,Ord)-0.28-4w-2%PVA specimens exhibit abnormally low peak pull-out loads due to large matrix defect, which will be shown in section 3.4.2. The test results from these specimens with macrofiber fracture or matrix defect are excluded for the calculations of averaged peak loads, averaged fiber displacements at peak load and averaged load-fiber displacement curves, which are shown in later sections. The values of peak fiber pull-out loads and fiber displacements at peak loads from these specimens of which test results were not included in the calculation of the averaged responses are underlined in the tables.

3.4.1.1 Typical fiber pull-out behavior

To evaluate the bond behavior of steel macrofibers in different matrices, the applied axial loads are plotted against the displacements, which consists of slippage and fiber elongation, for such

macrofiber. Let's take specimens with M(VS,Ord.)-0.54-4w-NF matrices as an example. The load-displacement curves for each specimen are shown in Figure 61, and used to calculate the averaged load-displacement curve which is plotted in Figure 62a and 62b for high and low fiber displacement ranges respectively. At the beginning of the test, the steel fiber stretches elastically with minimal slippage so the ascending branch of the averaged curve (Figure 62b) is linear. Mobilization of steel fiber slippage occurred at the end of such linear ascending curve and leads to a plateau on the averaged curve. Such slippage is the main component of displacement afterwards and leads to micro cracks around the steel fiber. The double peaks on the curves in Figure 61 and 62a were also observed in the hooked-end steel fiber pull-out tests conducted by other researchers, and such double peak shape is explained by multiple plastic deformation stages of the hook end as shown in Figure 63 [33]. The ascending curve before first peak load is caused by the increasing load necessary to deform the two bended portions of the hooked end of the steel fiber at stages a and b. After the first peak load, the load increases again to deform one remaining bended portion at stage c. After stage d, the load drops from the second peak load and the curve enter a constant load region which is associated with friction resistance. This type of twin peak is common for the fiber pull-out specimens investigated in this thesis. Some specimens didn't exhibit the second peak because the matrices provided relatively gradual decrement of fiber pull-out resistance after first peak as shown in Figure 64.
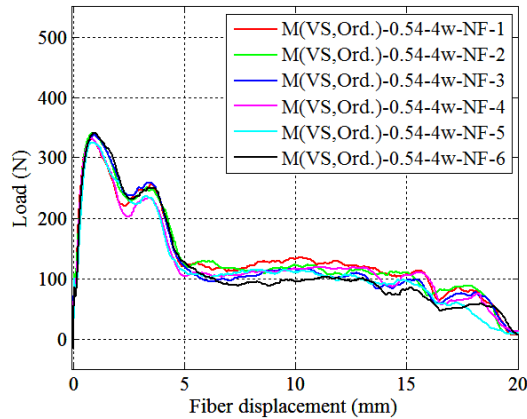
Figure 61: Individual load-displacement curves for M(VS,Ord.)-0.54-4w-NF specimens
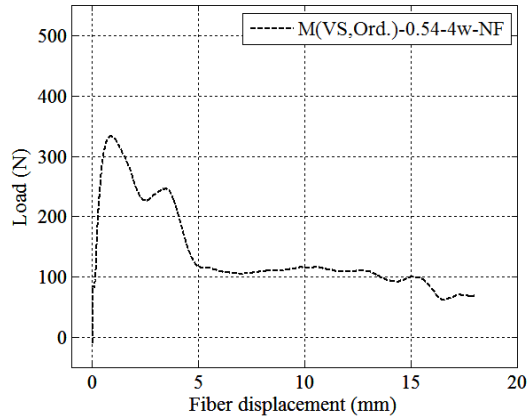
(a)   (b)

Figure 62: Averaged load-displacement curve for M(VS,Ord.)-0.54-4w-NF in (a) overall fiber displacement range (b) low fiber displacement range
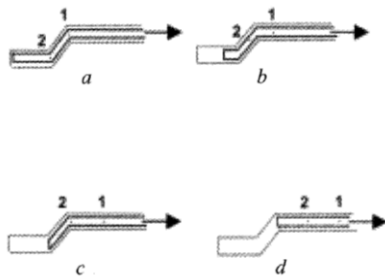
Figure 63: Plastic deformation stage of steel fiber hook [33]
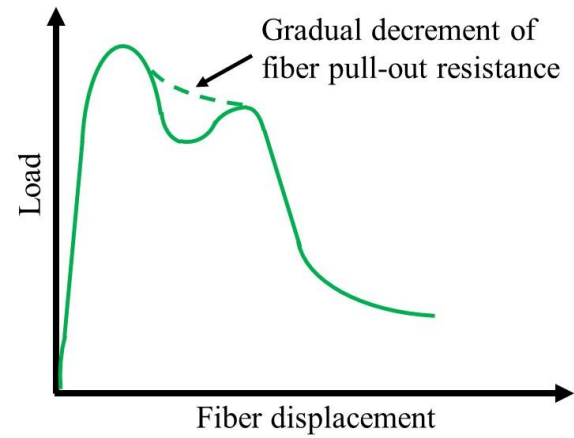
Figure 64: Schematic example showing how gradual fiber pull-out load decrement after first peak affect the shape of load-fiber displacement curve.

3.4.1.2   Test results for specimens with M(VS,Ord.) matrices with and without PVA fibers

As a result of same material proportions in the mortar portions of M(VS,Ord.) and HyFRC, the M(VS,Ord.) matrices achieved compressive strengths (Table 18) which are comparable to the compressive strengths of HyFRC matrices used for rebar pull-out tests (Table 7, 9 and 12). The averaged load-displacement curves for each type of fiber pull-out specimens with M(VS,Ord.)

matrices are shown in Figure 65a and 65b for overall and low fiber slippage ranges respectively. Increasing curing age from 2 to 4 weeks led to higher fiber pull-out resistance for the unreinforced mortar matrices before reaching the constant pull-out resistance stage. The PVA fiber reinforcement increased the load level corresponding to the end of the linear ascending curve occurring in the beginning of fiber pull-out, and improved the averaged pull-out resistance in the following non-linear ascending branch before maximum load.

(a)

(b)
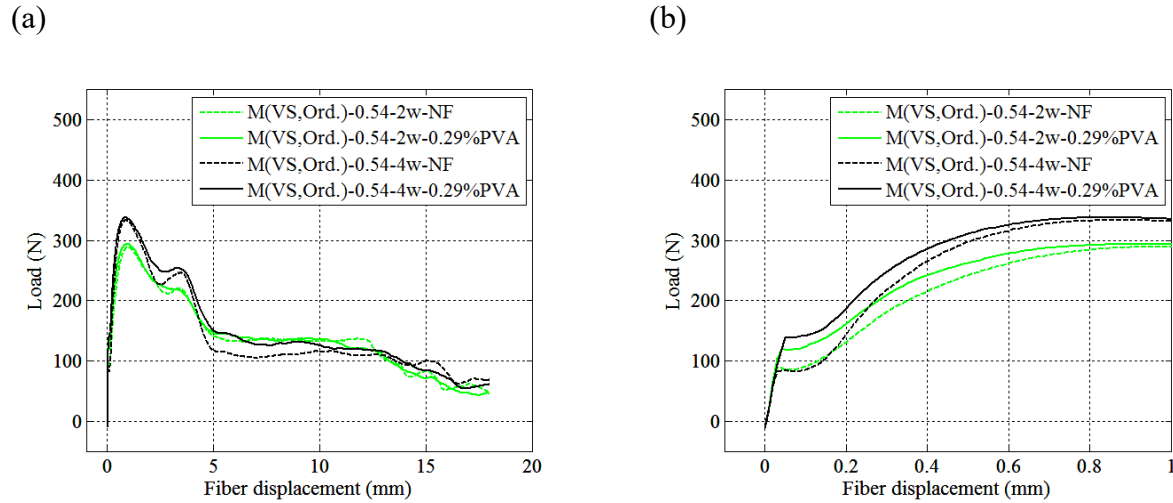
Figure 65: Averaged load-displacement curve for M(VS,Ord.) in (a) overall fiber displacement range (b) low fiber displacement range

3.4.1.3 Test results for specimens with M(SS,Ord.), M(SS,55FA) and M(SS,15FA-45S) matrices

The averaged load displacement curves obtained from fiber pull-out tests for M(SS,Ord.) are shown in Figure 66a and 66b for high and low fiber displacement ranges, respectively. Note that only no. 2 and 4 of specimens with M(SS,Ord.)-0.28-4w-2%PVA matrices were used to calculate their corresponding average load-displacement curve. No. 3, 5 and 6 specimens with M(SS,Ord.)-0.28-4w-2%PVA matrices were excluded from the calculation of averaged load-displacement response because of their abnormal shapes of individual load-displacement curves induced by large matrix voids at the macrofiber embedment region. Such abnormal shapes can be observed in Figure 67, which plots the individual load-displacement curves for all specimens with M(SS,Ord.)-0.28-4w-2%PVA matrices. As an example for the matrix defects discussed herein, the large voids for M(SS,Ord.)-0.28-4w-2%PVA-3 specimen is shown in section 3.4.2. Besides, no. 1 specimen with M(SS,Ord.)-0.28-4w-2%PVA matrix was not used for averaged load-displacement curve calculation because steel macrofiber fractured during the

fiber pull-out test. According to Figure 67, the fiber pull-out resistance of such specimen decreased abruptly after the fiber fracture occurred at 4.2 mm of fiber displacement.

(a)   (b)
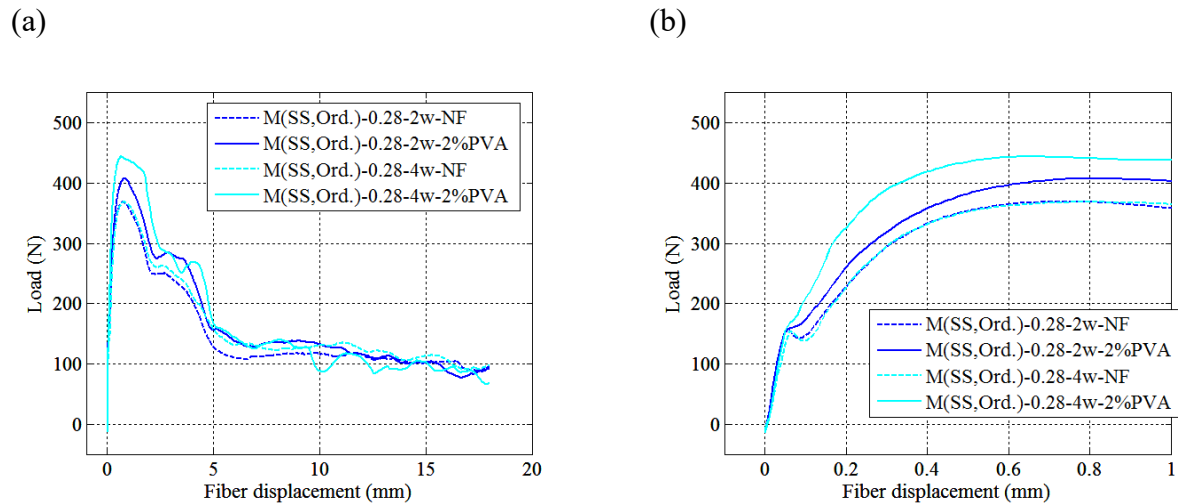
Figure 66: Averaged load-displacement curve for M(SS,Ord.) in (a) overall fiber displacement range (b) low fiber displacement range
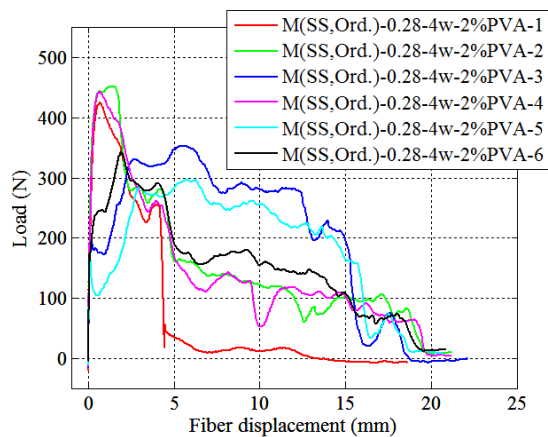
Figure 67: Individual load-displacement curves for M(SS,Ord.)-0.28-4w-2%PVA specimens

According to Figure 66, increasing curing age from 2 to 4 weeks led to minimal difference between the fiber pull-out behaviors in M(SS,Ord.) matrices without PVA fiber reinforcement. On the other hand, using 2% of PVA fibers in such type of matrix improved not only fiber pull-out resistances at the ascending curves before peak but also the peak pull-out load. Such enhancement from PVA fibers become more significant when the specimens were cured longer.

The averaged load-displacement curves for fiber pull-out specimens with M(SS,55FA) matrices are shown in Figure 68a and 68b for overall and low fiber displacement ranges respectively. On the other hand, the averaged load-displacement curves for M(SS,15FA-45S) specimens are shown in Figure 69a and 69b for overall and low fiber displacement ranges respectively. In Figure 68 and 69, the averaged fiber pull-out responses for M(SS,Ord.) specimens are also plotted for comparison.

(a) (b)
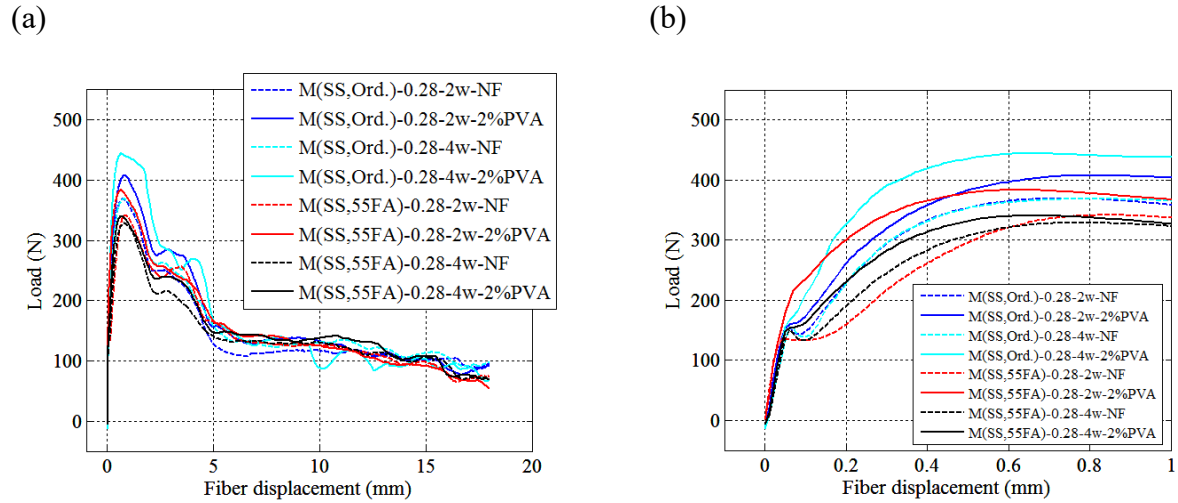
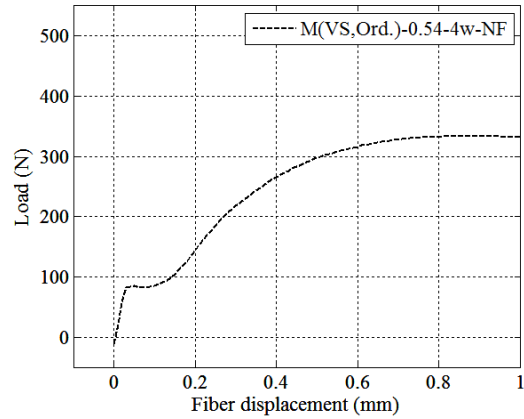Figure 68: Averaged load-displacement curve for M(SS,Ord.) and M(SS,55FA) in (a) overall fiber displacement range (b) low fiber displacement range

(a) (b)
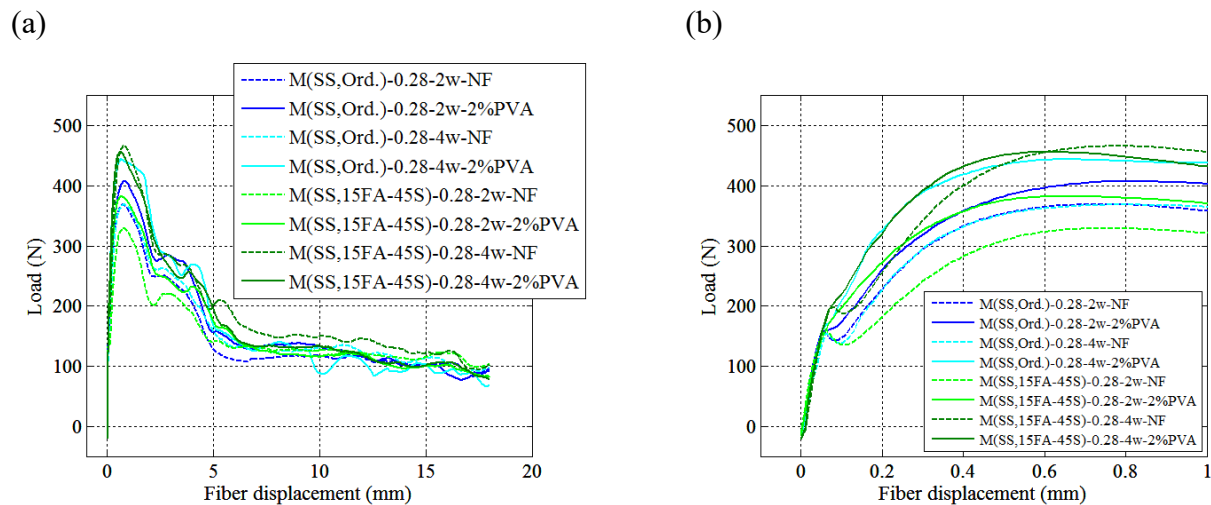
Figure 69: Averaged load-displacement curve for M(SS,Ord.) and M(SS,15FA-45S) in (a) overall fiber displacement range (b) low fiber displacement range

At 2 weeks of curing age, PVA microfibers improved the steel macrofiber pull-out load in M(SS,55FA) matrices until 2.9 mm of macrofiber displacement (Figure 68a). Such enhancement was very pronounced in the ascending branch before peak load (Figure 68b). When the curing age of M(SS,55FA) specimens was increased from 2 to 4 weeks, PVA fibers induced less significant improvement of steel fiber pull-out resistance before peak load. What's more, the PVA-fiber-reinforced M(SS,55FA) matrices which were cured for 4 weeks provided lower macrofiber pull-out resistance compared to reinforced matrices cured for 2 weeks.

Increasing curing age from 2 to 4 weeks enhanced the macrofiber pull-out behavior in unreinforced M(SS,15FA-45S) matrix significantly. At 2 weeks of curing age, the PVA-fiber-reinforcement in the M(SS,15FA-45S) matrices improved the macrofiber pull-out load until the load-fiber displacement curve entered the constant load region. The peak load was enhanced pronouncedly. When the curing age of such matrices was increased to 4 weeks, PVA fibers still improved the macrofiber pull-out behavior but such improvement only occurred in the ascending branch of the load-fiber displacement curve. In this case, the peak value and the pull-out resistance after peak were not improved by PVA fibers.

3.4.1.4 Test results for specimens with UHPC matrices

The averaged load-fiber displacement curves for fiber pull-out specimens with UHPC matrices are shown in Figure 70a and 70b for high and low fiber displacement ranges respectively. The macro fiber pull-out behaviors for unreinforced and reinforced UHPC specimens are almost identical.
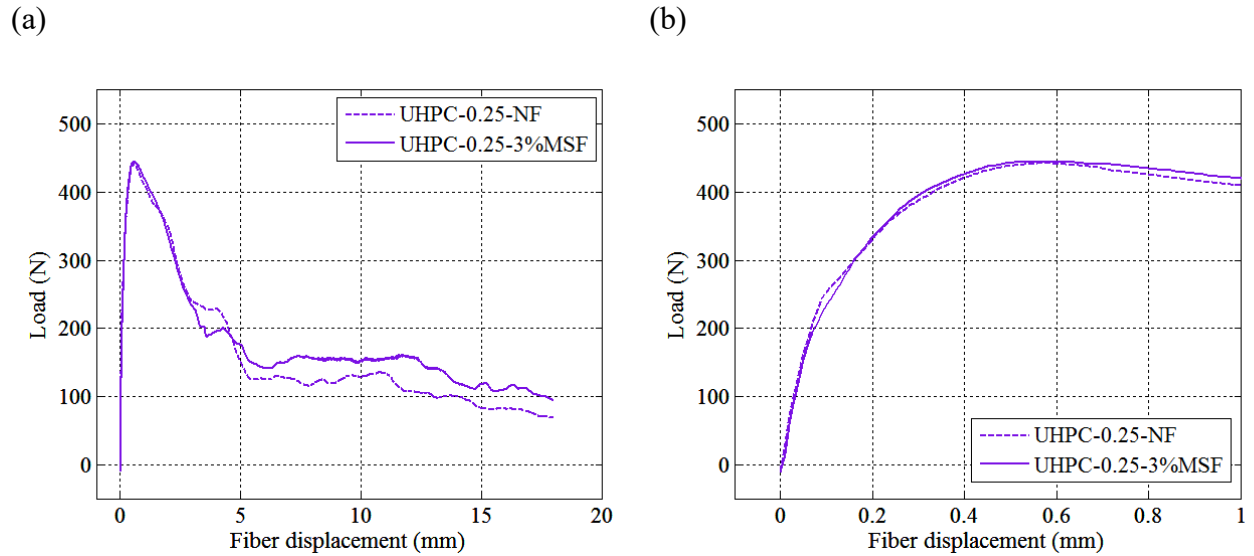
Figure 70: Averaged load-displacement curve for specimens with UHPC matrices in (a) overall fiber displacement range (b) low fiber displacement range

3.4.2 Analysis of the saw cut cross section

To further understand how microfibers affect the macrofiber/matrix bond by resisting micro cracks in the matrices, additional observations were conducted for the M(VS,Ord.)-0.28-4w, M(SS,Ord.)-0.28-4w and UHPC matrices around the steel macrofibers. After pull-out and removing the hooked-end steel macrofiber, blue epoxy was poured into the original fiber embedment region. If there are micro cracks induced by fiber pull-out, the cracks are filled with epoxy. After the epoxy was hardened and protected the micro cracks, the matrix was cut along the embedment region of steel macrofiber. A typical saw cut cross section is shown in Figure 71, in which the dark blue color form epoxy shows not only the original embedment region of the steel macrofibers, which consists of a straight portion and a hooked end, but also micro cracks perpendicular to the macrofibers. The micro cracks observed herein are similar to the micro cracks observed from the fiber pull-out specimen in the literature [33].
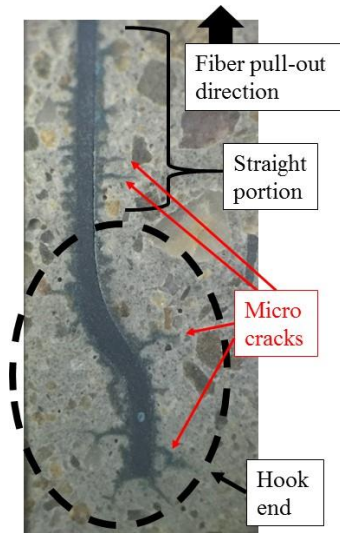
Figure 71: Typical saw-cut section of M(VS,Ord.)-0.54-4w-NF-3

The number of micro cracks along the steel macrofiber embedment region was counted based on observations with a microscope, and are summarized in Table 23. Unreinforced M(VS,Ord.) and M(SS,Ord.) matrices exhibited similar amount of micro cracks. Using 0.29% of PVA fibers in the M(VS,Ord) matrix reduced the amounts of micro cracks significantly. More pronounced reduction in the number of micro crack was achieved by reinforcing M(SS,Ord.) matrix with a much higher PVA fiber content, 2%. In this case, only very minimal micro cracks were observed in the PVA-fiber-reinforced M(SS,Ord.) matrices. No micro cracks were observed in UHPC matrices with and without steel microfibers.

Table 23: Number of cracks along embedment lengths of steel macrofibers

Specimen name	Number of cracks
M(VS,Ord.)-0.54-4w-NF-3	26
M(VS,Ord.)-0.54-4w-0.29%PVA-3	17
M(SS,Ord)-0.28-4w-NF-2	30
M(SS,Ord)-0.28-4w-2%PVA-3	3
M(SS,Ord)-0.28-4w-2%PVA-4	0
UHPC-0.25-NF-3	0
UHPC-0.25-3%MSF-1	0

No. 3 and no. 4 specimens with M(SS,Ord)-0.28-4w-2%PVA matrices were observed herein. The crack characteristic for no. 4 specimen is representative for specimens with typical load-fiber

displacement curves used for calculation of the averaged response. On the other hand, Figure 72 shows the area around the straight portion and hooked end of steel macrofiber embedment region in no. 3 specimen. In this case, an air void which attaches to the fiber hook are filled with blue epoxy. This air void is responsible for the poor fiber pull-out behavior of No. 3 specimen reported in Figure 67.
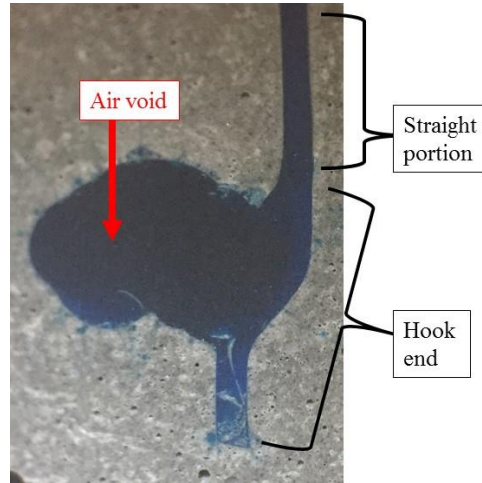
Figure 72: Saw-cut section of M(SS,Ord.)-0.28-4w-2%PVA-3

3.5   Discussion

3.5.1   Effect of curing age for macrofiber pull-out performance in unreinforced M matrices

Increasing curing age from 2 to 4 weeks leads to 15.9%, 8.4% and 8.9% of f_c' increments for unreinforced M(VS,Ord.), M(SS,Ord.) and M(SS,55FA) matrices respectively. A longer curing age allows the matrices to develop higher strengths, which are supposed to make macrofiber slippage more difficult to induce cracks, and allow the steel macrofiber/matrix interface to densify more. Therefore, longer curing may improve the macrofiber pull-out behavior in a certain manner. Such pull-out performance improvements induced by curing age increase are observed in unreinforced M(VS,Ord.) matrices as reported previously but not observed in unreinforced M(SS,Ord.) and M(SS,55FA) matrices. The hooked end macrofiber pull-out resistance before stage d in Figure 63 is more dominant by the plastic deformation process of fiber hook rather than the frictional resistance at macrofiber/matrix interface. In a low strength matrix, macrofiber pull-out induced many cracks around the fiber embedment region and hence, led to deformation of fiber pull-out channel around the fiber hook, which allows the hook to deform less during slipping out. A longer curing age provided a higher f_c' in unreinforced

M(VS,Ord.) matrices to reduce such channel deformation and hence, improve the macrofiber pull-out performance. Unreinforced M(SS,Ord.) and M(SS,55FA) matrices didn't exhibit such type of improvement because the longer curing age lead to lower percentages of f_c' increments compared to unreinforced M(VS,Ord.) matrix. As reported previously, the unreinforced M(SS,15FA-45S) specimens also exhibit macrofiber pull-out performance improvement induced by curing age increment (Figure 69). In this type of specimen, the longer curing age provide such performance improvement not only by providing higher f_c' but also by allowing higher degree of pozzolanic reaction from both fly ash and slag to densify the macrofiber/matrix interface.

3.5.2 Effect of microfibers in improving macrofiber pull-out performance

By resisting the cracks induced by steel macrofiber pull-out, the PVA-fiber-reinforcements delay the macrofiber slippage mobilization (corresponding to the end of the linear ascending branches of the averaged load-fiber displacement curves occurred in the beginning of fiber pull-out) in M(VS,Ord.) and M(SS,55FA)-0.28-2w matrices until higher load level. In the nonlinear portions of the averaged load-fiber displacement curves between the ends of the linear ascending curves and the maximum loads, PVA fibers maintain higher averaged pull-out load for macrofibers embedded in all M matrices. Such increments of pull-out load represent more significant slip stiffening behaviors of steel macrofibers.

The micro crack number comparison in section 3.4.2 is helpful to understand how the macrofiber pull-out performances are improved by the microfiber reinforcements. 0.29% of PVA microfibers leads to decrement of micro crack number in M(VS,Ord.)-0.54-4w matrix and hence, improves the macrofiber pull-out resistance before the peak pull-out load (Figure 65). Compared to M(VS,Ord.)-0.54-4w matrix, much higher dosage (2%) of PVA fibers in M(SS,Ord.)-0.28-4w matrix induces more significant micro crack number decrement and hence, leads to a more pronounced enhancement of macrofiber pull-out performance (Figure 66). In this case, such enhancement occurred not only before peak resistance but also at the peak resistance.

After macrofiber pull-out, no visible micro cracks were found in both unreinforced and steel-microfiber-reinforced UHPC matrices because their high matrix strengths prevent the micro crack developments. The microfiber reinforcement only makes a difference when micro cracks are present in the matrix without microfibers. Therefore, the UHPC specimen reinforced by steel microfibers exhibited a macrofiber pull-out behavior similar to the pull-out behavior exhibited by unreinforced UHPC (Figure 70).

80

3.5.3   Effect of replacing cement with supplementary cementitious/pozzolanic materials

As mentioned previously, higher matrix strengths, indicated by higher f_c' values, increase the difficulties for cracks to form in the matrices and may lead to higher macrofiber pull-out resistances. 55% of fly ash replacement delays the strength development in M(SS,55FA) matrices compared to M(SS,Ord.). In this case, the unreinforced M(SS,55FA) matrices cured for both 2 and 4 weeks exhibit lower f_c' values compared to the f_c' for all unreinforced M(SS,Ord.) matrices. Therefore, the averaged load-fiber displacement curve for unreinforced M(SS,55FA) exhibited lower peak and lower load before peak load compared to M(SS,Ord.). On the other hand, a different relation between f_c' and macrofiber pull-out resistance is observed in the comparison between unreinforced M(SS,15FA-45S) and M(SS,Ord.) matrices which are both cured for 4 weeks. At such curing age, unreinforced M(SS,15FA-45S) exhibited lower f_c' but provided higher macrofiber pull-out resistance compared to the unreinforced M(SS,Ord.) because the pozzolanic reaction from slag and fly ash in M(SS,15FA-45S) improved the bond resistance between macrofiber and matrix by densifying the interface between them.

In the M(SS,Ord.), increasing curing age from 2 to 4 weeks made the PVA microfibers more effective in improving macrofiber pull-out resistance (Figure 66) because the bond resistance between PVA fibers and such matrix increased during curing. Oppositely, increasing curing age decreased the ability of PVA fibers in M(SS,55FA) to enhance the macrofiber pull-out behavior before and at the peak pull-out load (Figure 68b). Such characteristic for M(SS,55FA) shows that when 55% of cement is replaced by fly ash, increasing curing age causes a decrement of the bond resistance between PVA fibers and matrix. As mentioned in section 2.2.5.3.2, the PVA fibers/matrix bond degradation induced by fly ash was confirmed in the literature [63]. As a result of such bond degradation, the PVA-fiber-reinforced M(SS,55FA) specimens with 4 weeks of curing age provided relatively low macrofiber pull-out resistance. Before reaching the constant load region of the averaged load-fiber displacement curve, such pull-out resistance was lower than the resistance provided by PVA-fiber-reinforced M(SS,Ord.) specimens with 2 and 4 weeks of curing ages.

Similar to M(SS,55FA), curing age increment also made the PVA fibers in M(SS,15FA-45S) matrix less effective in improving the macrofiber pull-out performance before and at the peak load of the load-fiber displacement curve (Figure 69b). However, such effectiveness decrement of PVA fibers in M(SS,15FA-45S) matrices were induced by a mechanism which is different to the mechanism for M(SS,55FA) matrices and is discussed herein.

Because minimal or no micro cracks were observed in microfiber-reinforced M(SS,Ord)-0.28-4w and unreinforced/microfiber-reinforced UHPC-0.25 matrices after macrofiber pull-out (Table 23), the maximum loads of the averaged load-fiber displacement curves of these specimens were mainly dominant by the plastic deformation of the hooked end of the steel macrofiber and occurred in a range between 442N to 445 N (Figure 66 and 70). Such range is considered as an upper limit for PVA microfibers to improve the peak macrofiber pull-out load significantly. The unreinforced M(SS,15FA-45S) with 2 weeks of curing age exhibited a peak load far lower than the load range mentioned herein so using PVA fibers improved the macrofiber pull-out performance obviously until the stage corresponding to the start point of the constant load region on the load-fiber displacement curve (Figure 69). On the other hand, the PVA fibers in such M(SS,15FA-45S) matrix with 4 weeks of curing age only improved the ascending load-fiber displacement curve before peak load and were not able to improve the peak load because the averaged load-fiber displacement curve for unreinforced M(SS,15FA-45S) matrix with 4 weeks of curing age (Figure 69) exhibited a peak load (466 N) higher than the load range mentioned above.

3.5.4 Interpretation of single fiber pull-out test results in regards to micro/macro fiber synergy in HyFRC

According to the results from the rebar pull-out tests, HyFRC matrix improved the rebar pull-out resistance compared to OC, and provided higher peak bond stress and bond resistance after peak bond stress compared to ECC. In addition, HyFRC also exhibited sufficient bond damage resistant when the rebar was pulled out under uniaxial cyclic loading. The superior bond performance in HyFRC was achieve by a fiber content as low as 1.5% (Table 1) because the multi-scale crack bridging from micro and macro fibers provided high crack resisting ability of matrix.

The PVA microfibers in HyFRC resist the micro cracks at onset caused by rebar pull-out before such cracks become macro cracks, which are then bridged by the steel macrofibers. In addition, the PVA microfibers also make the steel macrofiber bridging more effective because the pull-out resistance between the macrofibers and matrix are improved by the microfiber reinforcement.

The fiber pull-out results for specimens with M(VS,Ord.) mixtures, which are designed according to the mixture of HyFRC, confirm that PVA microfibers with same volume fractions as the mortar portion of HyFRC improve the bond behavior of steel macrofiber pronouncedly (Figure 65b). When a steel macrofiber is bridging a crack induced by rebar pull-out, the fiber elongation and fiber slippage occur. The PVA-fiber-reinforcement makes the steel fiber more difficult to be pulled out. Therefore, the steel fiber elongates further and provides higher crack

closure stress, which leads to higher rebar gripping force from the HyFRC matrix. In this case, the PVA microfibers lead to more significant slip stiffening behavior for steel macrofiber and such an enhancement in fiber scale is one of the reason explaining why HyFRC provides superior slip stiffening behavior and peak/residual bond resistance of rebar. Herein, a multi-scale bond enhancement is observed in a system consists of a rebar embedded in the HyFRC matrix.

According to the discussion in section 3.5.3, the fiber pull-out results from M(SS,Ord.) and M(SS,55FA) specimens shows that replacing 55% cement with fly ash make the PVA microfiber reinforcement less effective in resisting the macrofiber pull-out at 4 week of curing age. Although the M(SS,Ord.) and M(SS,55FA) matrices have different material proportions compared to the HyFRC matrices with and without high volume fly ash for rebar pull-out specimens, the fiber pull-out test results for these M matrices show how fly ash decrease steel macrofiber pull-out resistance in HyFRC by weakening the bond resistance between PVA microfiber and matrix. Such fiber/matrix bond degradations induced by fly ash decrease the rebar pull-out resistance in HyFRC-50FA. Using high volume fly ash in the HyFRC material make the multi-scale bond enhancement less significant in a HyFRC-rebar system.

4 Computational simulation of rebar pull-out behavior in HyFRC

4.1 Introduction

Finite Element (FE) models are developed in a Finite Element Analysis (FEA) software, DIANA [69], to investigate the rebar pull-out behavior in the bond regions of HyFRC specimens without and with transverse steel reinforcement. In the 3-dimensional model presented in [59], radial matrix displacement on rebar/matrix interface is induced by axial displacement of rebar through a kinematic relation. To simplify the modeling work, 2-dimensional models were developed in this thesis and the radial matrix displacements are directly applied by assigning displacements to matrix nodes at rebar/matrix interface. Similar to [59], cohesive crack laws, which is expressed as relations between crack width and crack closure stress, are applied to interface elements to simulate the behavior of splitting cracks induced by rebar bond behavior.

The DIC measurements performed for rebar pull-out tests only provide the mechanical behaviors on surfaces of HyFRC matrices. On the other hand, the FEA results from the model reported herein characterize the mechanical behavior inside the HyFRC matrices, and support the explanation for the mechanical behavior observed in the rebar pull-out tests with DIC.

4.2 Properties and parameters of rebar pull-out model

4.2.1 Model for Unconfined HyFRC specimens

An overall view for the dimension and mesh of the model with unconfined HyFRC matrix is provided in Figure 73a. The elements in gray and light blue regions represent the HyFRC matrix. They are 2D plane strain elements. To simplify the model, the material for these elements are assumed to be isotropic and elastic. The elastic modulus was selected as 22660.8 N/mm^2 according to the measurement from compression tests for HyFRC conducted in the rebar pull-out test program. The Poission ratio was assumed to be 0.2, which is a typical value for concrete. Figure 73b highlights the region around rebar/matrix interface. Radial displacements, p1, p2, p3, p4, p5 and p6, were assigned to the red nodes in the figures. Table 24 shows the components of radial displacement rates in x-direction and y-direction for these radial displacement cases. Each

x-direction and y-direction component is represented by multiplying a constant displacement rate (0.0208 mm/sec) by a trigonometric function. The angle used for the trigonometric function is the counter-clockwise angle from the direction of x-axis to the direction of displacement rate for the corresponding radial displacement case. For example, 30 degrees is used for the trigonometric function for load case p1. In this case, p1 represents 0.0208 mm/sec of displacement in the direction that is 30 of counter-clockwise degrees apart from the x-direction. In Figure 73b, p1, p2, p3, p4, p5 and p6 displacement cases respectively move the inner boundary of element E1, E2, E3, E4, E5 and E6 in radial directions with such constant displacement rate (0.0208 mm/sec). The red nodes, of which displacement directions were specified by the radial displacement cases, are not able to move in other directions. Therefore, the relative displacement between matrix and rebar is restrained in circular direction. Such type of restrain also exists in the rebar pull-out model in [59].

(a)   (b)
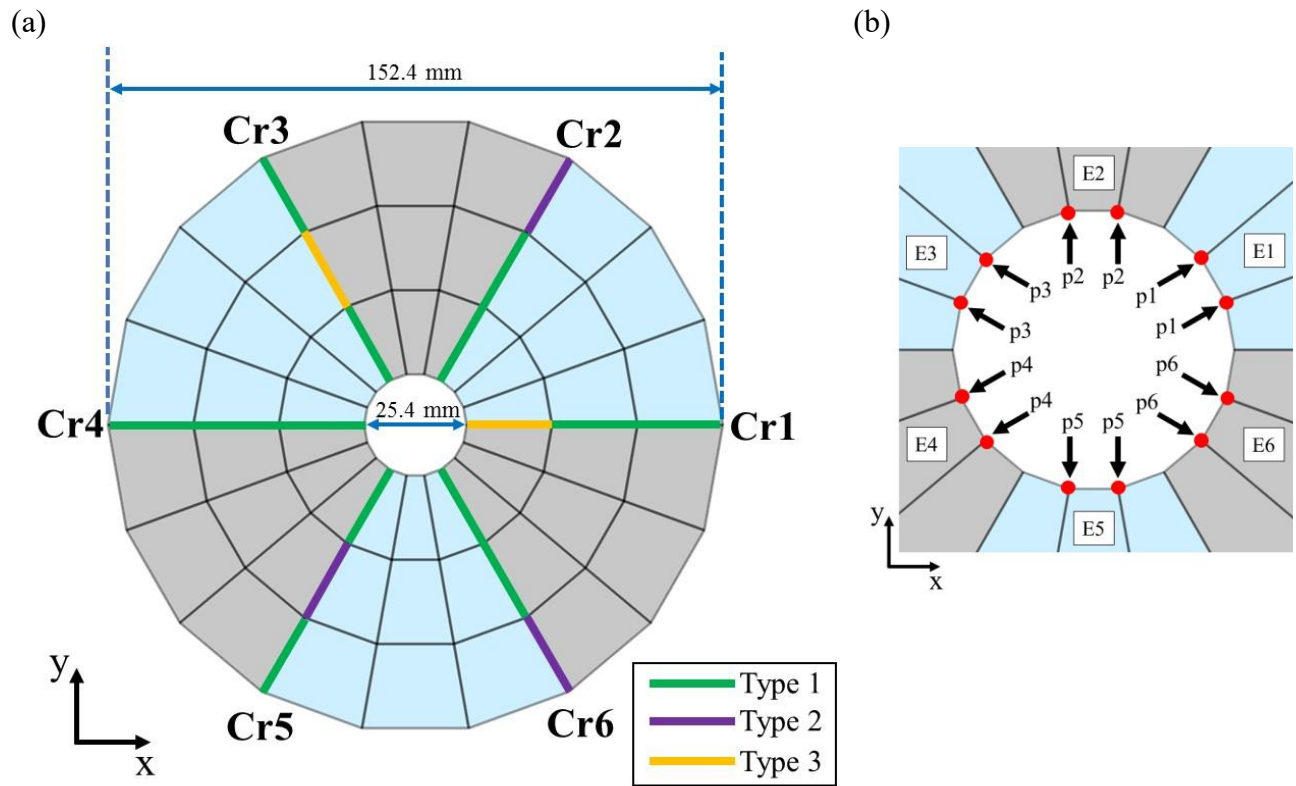
Figure 73: Rebar bond model under (a) overall view (b) local view around the rebar/matrix interface

Table 24: Information for assigned radial displacement cases

Name of radial displacement case	Displacement rate in x-direction	Displacement rate in y-direction
p1	$(0.0208\ mm/sec) \times \cos(30°)$	$(0.0208\ mm/sec) \times \sin(30°)$
p2	$(0.0208\ mm/sec) \times \cos(90°)$	$(0.0208\ mm/sec) \times \sin(90°)$
p3	$(0.0208\ mm/sec) \times \cos(150°)$	$(0.0208\ mm/sec) \times \sin(150°)$
p4	$(0.0208\ mm/sec) \times \cos(210°)$	$(0.0208\ mm/sec) \times \sin(210°)$
p5	$(0.0208\ mm/sec) \times \cos(270°)$	$(0.0208\ mm/sec) \times \sin(270°)$
p6	$(0.0208\ mm/sec) \times \cos(330°)$	$(0.0208\ mm/sec) \times \sin(330°)$

To simplify the model, only six of radial splitting cracks were used. Line interface elements with plane strain configuration were generated at the boundaries of gray and light blue meshes to represent these radial splitting cracks, which are labeled as Cr1, Cr2, Cr3, Cr4, Cr5 and Cr6.

Along each crack, there are three of such interface elements and the different interface element color in Figure 73a represent type 1, 2 and 3 of crack interface. Different types of line interfaces were used along most of the cracks in the model (Figure 73a) to simulate a more realistic crack resisting behavior of HyFRC. Within a HyFRC, the concrete matrix is not perfectly homogeneous and fiber distributions/orientations are slightly different at different regions in the matrix. Take Figure 74 as an example for hooked-end steel macrofibers. The fiber distributions and orientations are different in sections Cr-A, Cr-B and Cr-C along a splitting crack which propagates from the rebar to the free surface of the matrix. Under same crack widths, the Cr-A section exhibits a higher crack closure stress compared to Cr-B because less fibers are located in Cr-B. Although the Cr-C section has the same amount of fiber as Cr-A, it is less effective in providing a high crack closure stress because some of the fibers are oriented less favorably. In addition, different PVA microfiber distributions/orientations and concrete matrix compositions along a crack also lead to different tensile strength and crack resisting abilities at different crack sections. To reflect the different tensile properties along a crack, different types of line interfaces are induced in the FEA model.

Different types of interfaces have common material parameters, which are summarized in Table 25, while different tensile strengths and multilinear tension softening behaviors, which are characterized by crack width-crack closure stress curves in Figure 75, were assigned to different interface types. The key data points on these curves are summarized in Table 26.
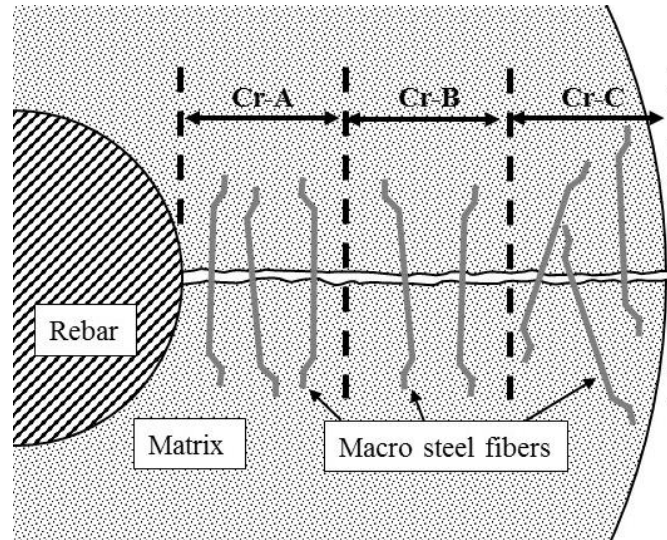
Figure 74: Different fiber distributions and orientations along a crack

Table 25: Common material parameters for line interface elements

Parameter name		Parameter selections or values
Interface nonlinearities		Discrete cracking
Normal stiffness modulus		900 N/mm^3
Shear stiffness modulus		90 N/mm^3
Mode-I model	Model type	Multilinear tension softening
	Unloading type	Secant
Mode-II model	Model type	Brittle
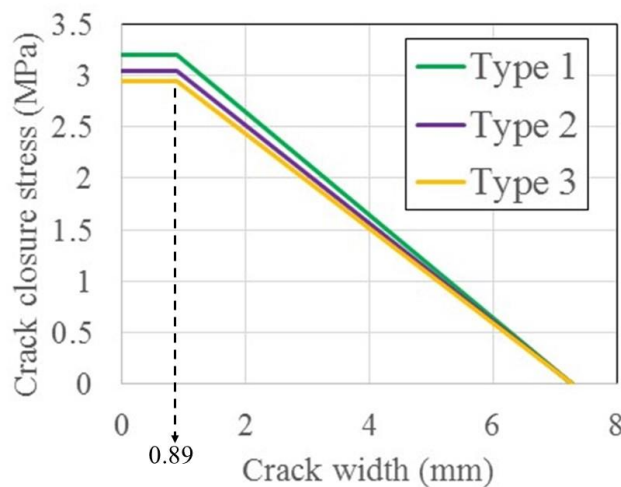
Figure 75: Crack width-crack closure stress curves for different line interface types

Table 26: Values of crack width-crack closure stress curves for different line interface types

Crack width (mm)	Crack closure stress (MPa)		
	Type 1	Type 2	Type 3
0	3.2	3.04	2.944
0.89	3.2	3.04	2.944
7.29	0	0	0

The crack width-crack closure stress curve for the type 1 interface was obtained from [70], in which a cohesive crack law was utilized to investigate the same type of HyFRC as in this thesis. Such curve consists of a plateau following by a linear descending branch. The tensile strength of type 1 interface is selected as the stress value (3.2 MPa) on the plateau. When load is applied to the interface in the normal direction, the interface opening is controlled by its normal stiffness modulus (900 N/mm^3) until the tensile strength (3.2 MPa) is achieved. In fact, the crack closure stress within the interface can be viewed as a tensile stress that is being transferred across such an interface. After achieving the tensile strength, the type 1 interface carries constant stress (3.2 MPa) until additional 0.89 mm of opening, which corresponds to the start point of the descending curve for crack width-crack closure stress relation. Beyond the plateau region, crack closure stress along the interface follows the crack width-crack closure stress relation as shown in Figure 75.

Many fibers pass through the location of each 2D line interface element, which actually simulates the splitting crack surface passing through the entire matrix heights which are 304.8 and 196.9 mm for d1 (Figure 19) and d2 (Figure 40) specimen, respectively. Therefore, it is assumed that the differences of averaged tensile properties induced by different fiber orientation and distribution on each segment of splitting crack are relatively small. In this case, the crack width-crack closure stress curves for type 2 and 3 interfaces were determined by scaling down the crack closure stresses on the curve for type 1 interface with 95% and 92% of percentages, respectively, rather than smaller values. The values of crack closure stresses on the plateaus of the type 2 and 3 curves were used as the tensile strength for type 2 and 3 interfaces, respectively. In this case, type 2 and 3 interfaces have 3.04 and 2.944 MPa of tensile strengths, respectively. Type 2 and 3 interfaces behave similarly as type 1 interface except for their different tensile strengths and closure stresses.

4.2.2 Model for HyFRC specimen with transverse steel reinforcement

In addition to unconfined HyFRC model, FEA was also conducted to a model for HyFRC with transverse steel reinforcement to investigate the effect of spiral reinforcement in HyFRC matrix during rebar pull-out. The transverse-steel-confined HyFRC model have identical geometric properties and material parameters as the unconfined model, which is introduced in the previous section, except that the confined model includes a steel hoop model as well as shown in Figure 76a. The steel hoop model has 18 truss elements forming a polygon shape which is identical to the perimeter shape of the matrix mesh. Point interfaces were created between the truss elements at points Sp1, Sp2, Sp3, Sp4, Sp5 and Sp6. The steel hoop model utilized rigid links to interact with the matrix mesh. To visualize the rigid links, element groups at different sides of line interfaces (located along Cr1, Cr2, Cr3, Cr4, Cr5 and Cr6) or point interfaces (located at Sp1, Sp2, Sp3, Sp4, Sp5 and Sp6) are moved apart in Figure 76b. Each red line in the figure represents a rigid link connecting a node on matrix mesh perimeter to a node at corresponding location on the steel hoop. In this case, a matrix node on one end of a red line is the master node and the steel hoop node on the other side of the red line is a slave node, of which the displacement is forced to be same as its master node assigned by the rigid link. The dashed line in Figure 76b corresponds to the line and point interfaces.

A typical linear-elastic steel material model with 200,000 N/mm^2 of elastic modulus and 0.3 of Poisson's ratio was assigned for the truss elements in the steel hoop model. 0.288 mm^2 was used for both cross section areas for the truss elements and interface surfaces for the point interfaces. Such parameter setting is equivalent to 0.75 vol.% of transverse steel in a cylindrical specimen with 152.4 mm of diameter. Such amount of transverse steel reinforcement is also used in spiral-confined HyFRC specimen for the no. 8 rebar pull-out experiment reported in this thesis.

(a)

Matrix mesh

Steel hoop model

Cr3 Cr2

Cr4 Cr1

Cr5 Cr6

x
y

Type 1
Type 2
Type 3

Sp3 Sp2

Sp4 Sp1

Sp5 Sp6

(b)

Matrix mesh

Steel hoop model

Cr3 Cr2

Cr4 Cr1

Cr5 Cr6

Sp3 Sp2

Sp4 Sp1

Sp5 Sp6
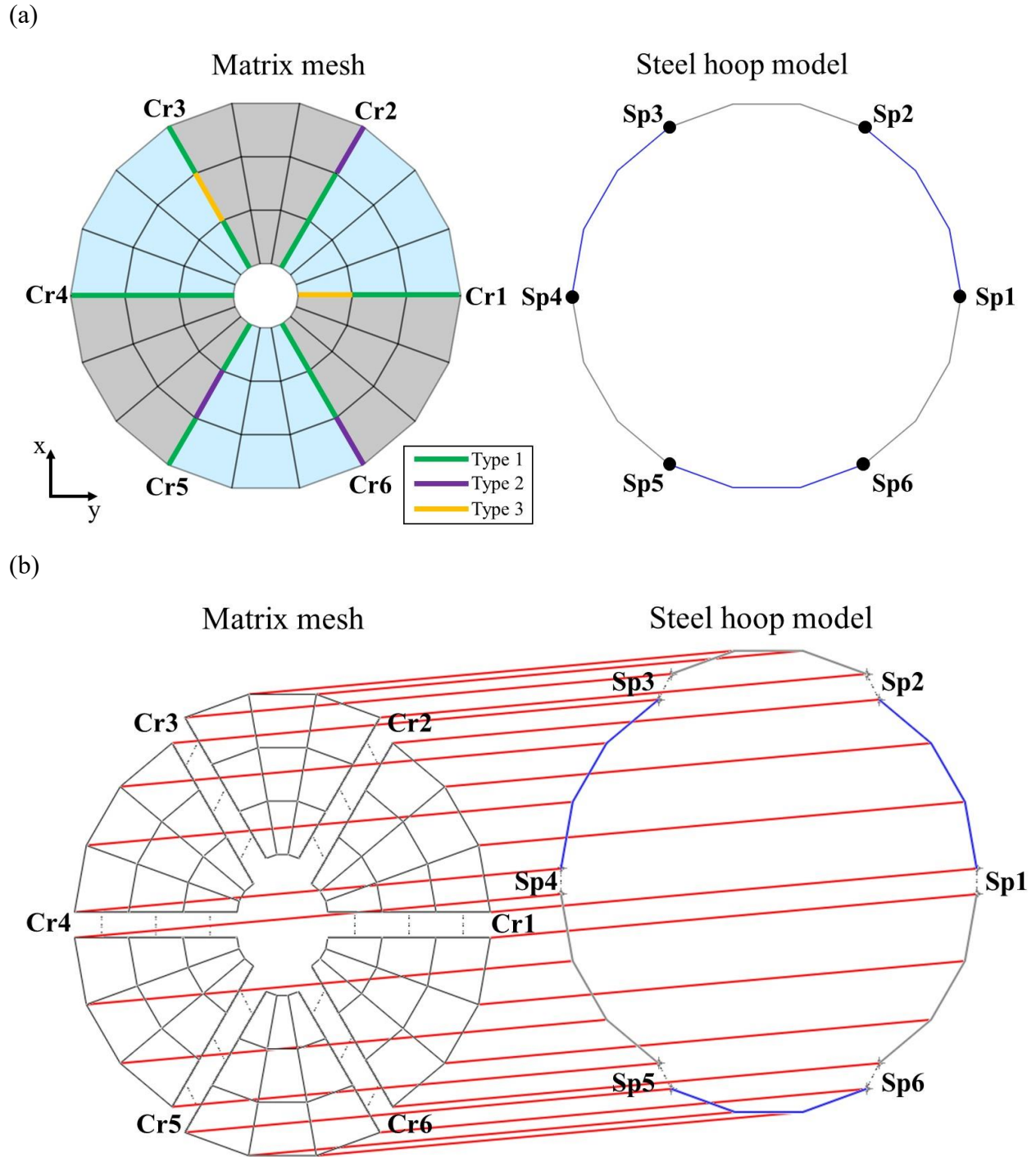
Figure 76: Rebar bond model for transverse-steel-confined HyFRC (a) Overall view (b) Rigid connection between matrix mesh and steel hoop model

The point interfaces are allowed to open in circular directions of the hoop under a linear relation between interface opening and stress across such interface. The point interfaces Sp1, Sp2, Sp3, Sp4, Sp5 and Sp6 directly resisting the opening of crack interfaces Cr1, Cr2, Cr3, Cr4, Cr5 and Cr6 respectively by utilizing the rigid connection between nodes on point interfaces and the matrix circumference nodes on crack interfaces, as shown in Figure 76b. Such characteristic allows the point interfaces to simulate how the spiral clamps the crack at the circumference nodes of the line interfaces. To understand such idea further and determine the interface opening-stress relation for the point interface, a conceptual rebar pull-out model for transverse-steel-confined HyFRC is proposed in Figure 77. Such model has six splitting cracks, which orient 60 degrees apart from each other and have same crack pattern as the cracks (Cr1 to Cr6) in the Finite Element model (Figure 76a). The red dashed lines equally divide the conceptual model into 6 pieces and each of them have a splitting crack in the middle. Considering the low bond resistance between the matrix and smooth surface of transverse steel reinforcement, the transverse steel reinforcement slips freely against the matrix when matrix circumference elongation is induced by splitting crack developments. Simultaneously, the transverse steel hoop is elongated with a total elongation similar to the sum of crack widths for each splitting crack. If each crack is opened uniformly to a constant crack width (w), the steel hoop elongation within 79.8 mm (one-sixth of the steel hoop circumference) is approximately equal to w according to Figure 77. In this case, the steel hoop strain (ε_{sh}) can be expressed by the following equation:

$$\varepsilon_{sh} = \frac{w}{79.8\ mm} \quad\quad\quad (3)$$

By inserting above strain value to the equation representing linear-elastic relation between stress and strain in steel, the stress in steel hoop (σ_{sh}) can be calculated by following equation:

$$\sigma_{sh} = E_{steel} \times \varepsilon_{sh} = E_{steel} \times \frac{w}{79.8\ mm} \quad\quad\quad (4)$$

where E_{steel}=Elastic modulus of steel

On the other hand, the stress developed at the point interface ($\sigma_{point\ int.}$) is calculated by the normal stiffness modulus (K_n) of the interface times interface opening in the circular direction. Assuming the interface opening is equal to crack width (w), the value of $\sigma_{point\ int.}$ can be calculated as follow:

$$\sigma_{point\ int.} = K_n \times w \quad\quad\quad (5)$$

To achieve same stress at point interface in the FEA model as the steel hoop stress in the conceptual model, the following equation need to be satisfied:

$$\sigma_{point\ int.} = \sigma_{sh} \qquad\qquad (6)$$

The value of normal stiffness modulus for point interfaces can be calculated as equation (7), which is obtained by inserting equation (4) and (5) into equation (6).

$$K_n = \frac{E_{steel}}{79.8\ mm} \qquad\qquad (7)$$

By assuming that E_{steel} is 200000 N/mm² (a typical value of elastic modulus for steel), the K_n value is determined to be 2506 N/mm³ for the FEA model. On the other hand, 20000 N/mm³, which is a relative large value, is used as the shear stiffness modulus for the point interface to prevent pronounced opening of such interface in radial direction.
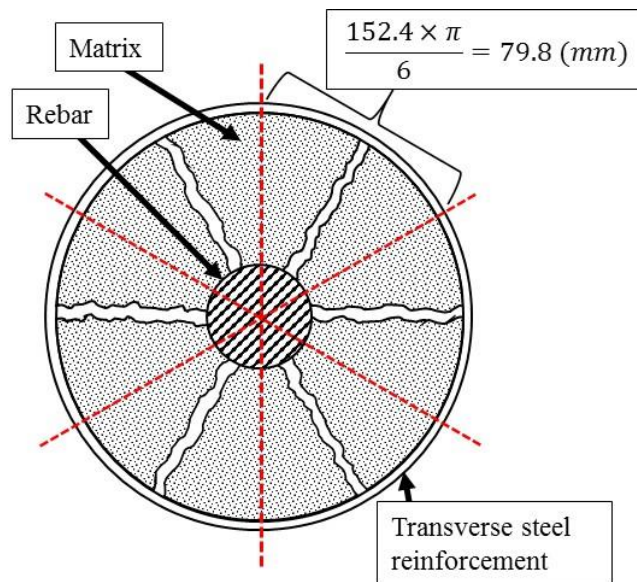
Figure 77: Ideal model for transverse-steel-confined HyFRC during rebar pull-out

4.3   Analysis, results and discussion

Nonlinear structural analysis was performed for the FE models for unconfined and transverse-steel-confined HyFRC. The tensile stresses and relative displacements at the crack interfaces (Cr1, Cr2, Cr3, Cr4, Cr5 and Cr6) at different times are shown in Figure 78 and 79, respectively. In the figures, the analysis results are visualized at 1, 2, 4, 9 second, which respectively correspond to 0.0208, 0.0417, 0.0833 and 0.1875 mm of rebar/matrix interface node displacements induced by each radial displacement cases (p1, p2, p3, p4, p5 and p6).

92

By averaging the strain gauge measurements from the "M" strain gauges at different sides reported in Figure 47b, the maximum value of circular elongation on the matrix circumference with same height as the middle bond region can be estimated for HyFRC-C(0.75)-d2-1 specimen, the spiral-confined HyFRC specimen for no. 8 rebar pull-out test with DIC. That is to say, experimental results showed that rebar pull-out induced a circular elongation for HyFRC with transverse steel reinforcement that was always lower than such maximum value. On the other hand, increasing time gradually increased the averaged circular strain on the matrix mesh circumference of the FE models and a similar value of such averaged circular strain was achieved at 9 second of time in the analysis for the model with transverse-steel-reinforcement. Because further increasing time for such model led to unrealistic value of such averaged circular strain that is higher than the maximum circular elongation obtained from the experiment, the stage corresponding to 9 second of time is the last stage presented in Figure 78 and 79.

At 1 second, the FEA model analysis results reveal how the splitting cracks initiated in close vicinity of the rebar in both confined and unconfined HyFRC specimens as shown in Figure 78 and 79. In this case, higher tensile stresses and crack openings can be observed at the region closer to rebar, and all of the cracks developed uniformly. Because the crack widths at the outside matrix is minimal at such an early stage, the point interfaces, which represent the transverse steel reinforcement, haven't been mobilized yet. Such characteristic explains the very similar analysis results for unconfined and transverse-steel-confined HyFRC models at 1 second.

After 2 seconds, the tensile stresses across all cracks reach the maximum tensile capacities which are 3.2, 3.04 and 2.944 MPa for type 1, 2 and 3 crack interfaces respectively. If no transverse steel reinforcement was used, non-uniform crack width distributions among the radial cracks develop beyond this stage due to the non-homogeneous tensile properties induced by different crack interface types. For example, the outside crack widths of Cr6 and Cr3 become relatively wide after 2 and 9 second, respectively (see Figure 79 for HyFRC-NC). On the other hand, the model with transverse steel hoop exhibits uniform crack width distributions among all cracks at all stages. The transverse steel hoop is more effective in resisting the cracks at the circumference region, in which additional crack closure stress is applied by the point interface on the steel hoop model. As a result, the steel hoop leads to finer crack width at the outside matrix compared to the crack width in close vicinity of the rebar.

Figure 78: Tensile stress across crack interface during rebar pull-out

Time (sec)	HyFRC-NC	HyFRC-C	Color bar for tensile stress (N/mm²)
1			
2			
4			
9			
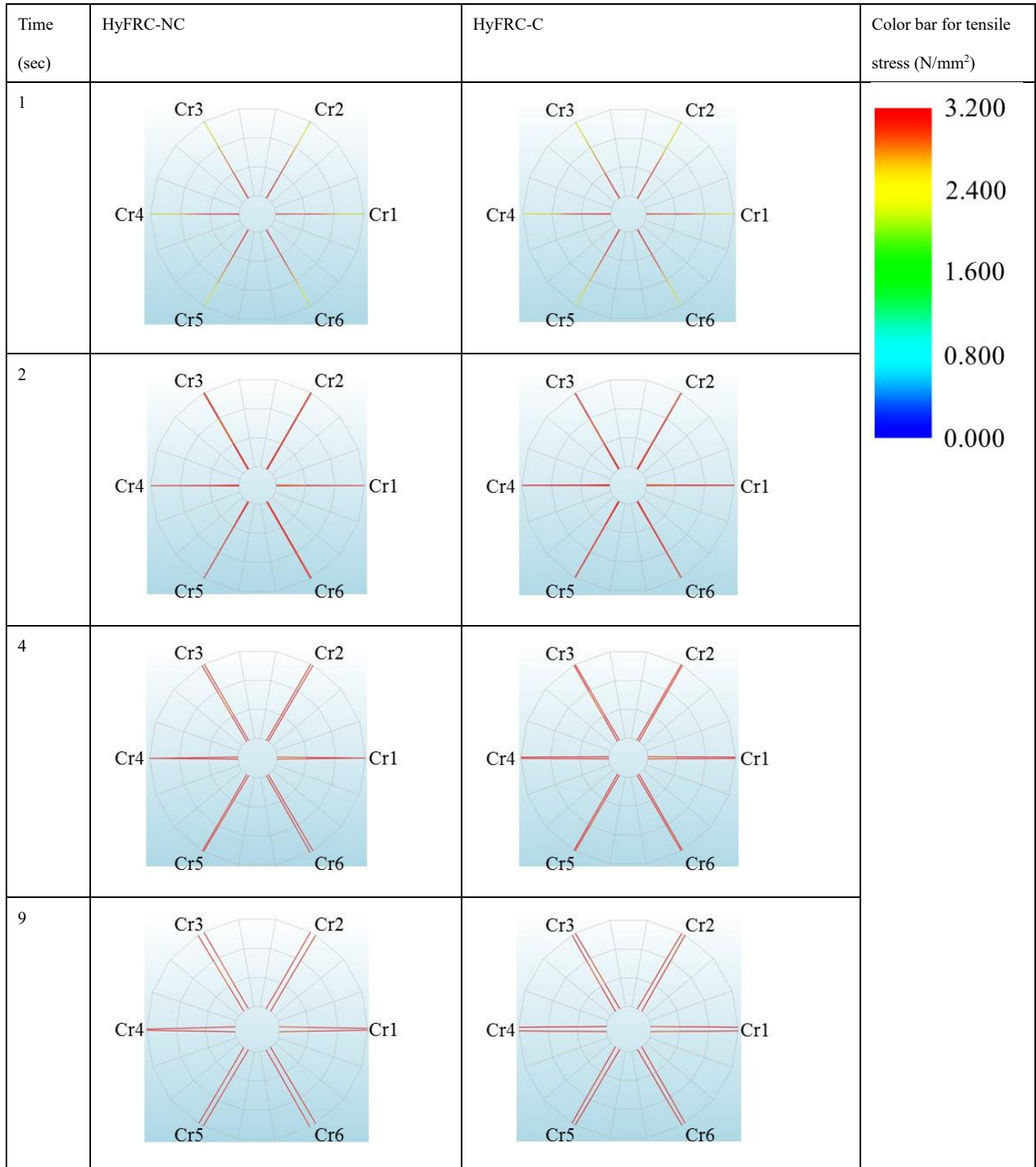
Figure 79: Crack interface opening during rebar pull-out

Time (sec)	HyFRC-NC	HyFRC-C	Color bar for relative displacement (mm)
1			
2			
4			
9			
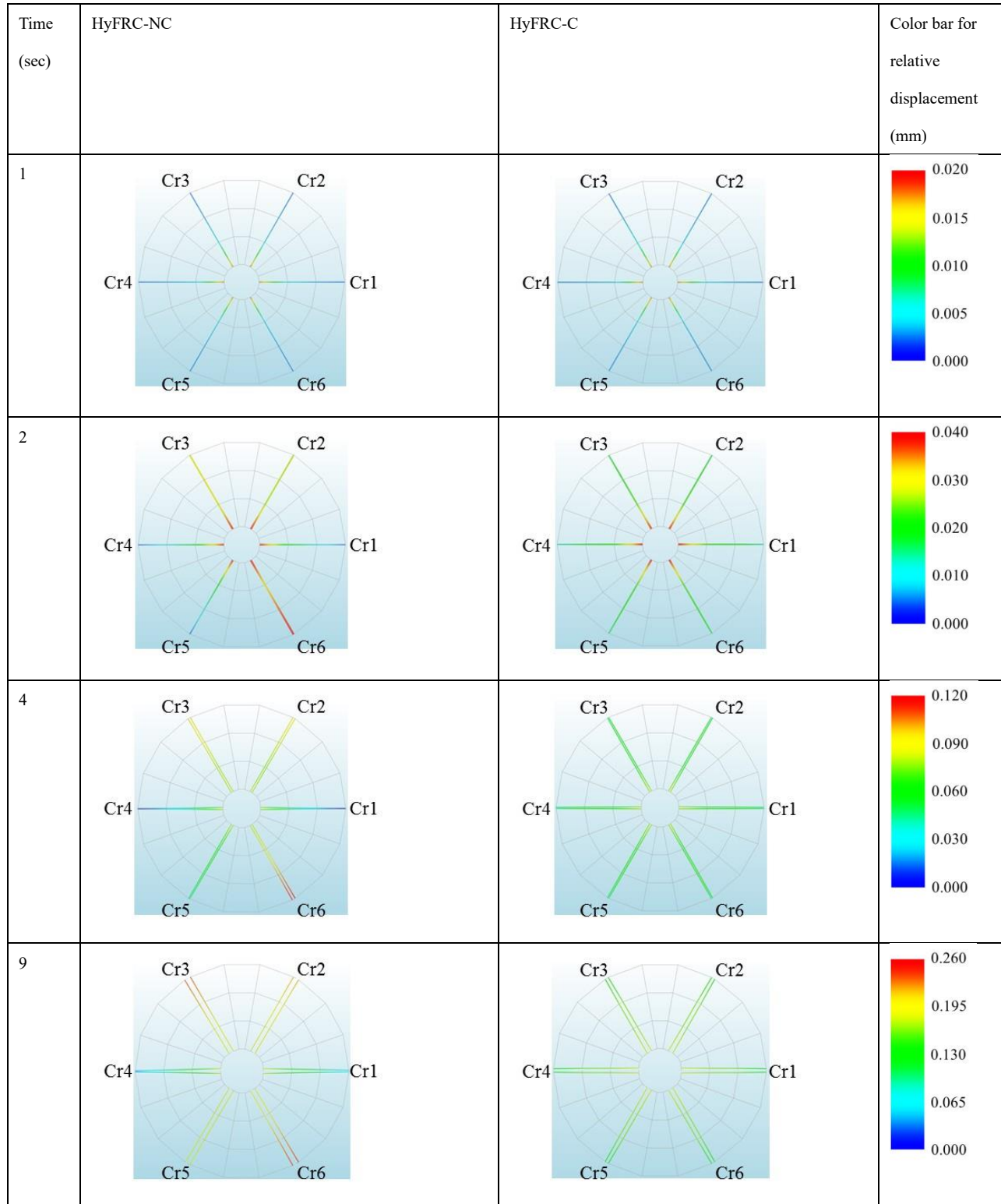
4.3.1 Comparing analysis results from rebar pull-out model to the experimental results

from rebar pull-out test with DIC

As mentioned in section 2.3.4.4, the rebar pull-out experiment with DIC shows that the transverse steel reinforcement lead to a more uniform crack width distribution. Herein, the FEA results reveal the same effect due to the transverse steel reinforcement, despite the fact that this analysis represents the crack distribution in the middle bond region and not at the top surface as in the DIC measurements. Hence for the confined HyFRC cases the DIC and FEA results are in agreement. However, a slight deviation between the FEA and DIC results was observed for the unconfined HyFRC. Whereas the DIC results for unconfined HyFRC reveal a more non-uniform crack distribution, the FEA model reveals a less non-uniform crack width distribution. In the unconfined HyFRC model, radial displacements applied at the rebar/matrix interface restrains the relative displacement between rebar and matrix in circular direction, and hence, make the non-uniform crack width distribution less pronounced. In this case, such constrain in FE model makes the crack width distributions of HyFRC without transverse steel reinforcement more similar to the crack width distributions in the FE models of HyFRC with transverse steel reinforcement, which is very uniform. However, the FEA results still show that HyFRC without transverse steel reinforcement have relatively non-uniform crack width distribution compared to HyFRC confined by transverse steel reinforcement. The crack width characteristic from the FEA models may be useful to explain how crack propagation processes along the specimen height lead to different crack characteristics in the middle bond regions compared to the top surfaces for rebar pull-out specimens. During rebar pull-out tests, the splitting cracks need to be wide enough in the middle bond region to propagate to and be visible at the top surface. In the middle bond region of the unconfined HyFRC specimen, the crack width is not as uniform as for the confined HyFRC and some relatively fine cracks may not able to propagate to the top specimen surface. Therefore, less cracks were observed on the top specimen surface of unconfined HyFRC by DIC compared to the top surface of confined HyFRC although unconfined HyFRC exhibits more cracks in the middle bond region compared to spiral-confined HyFRC according to Table 8, which shows the crack numbers on saw cut cross sections from the middle bond regions.

5 Summary and concluding remarks

The pull-out tests revealed that rebars embedded in HyFRC matrices exhibit a higher pull-out resistance compared to the rebar embedded in control OC matrices. This superior pull-out resistance is due to the effectiveness of HyFRC in resisting splitting cracks which leads to a noticeable rebar/matrix bond enhancement compared to OC material. When the splitting failure of an unconfined OC matrix is guaranteed by a low c/d_b ratios and a high rib height/rib spacing ratio, such an enhancement becomes more significant because the HyFRC matrix prevents the rebar/matrix detachment by transforming the failure mode from a splitting to a frictional pull-out. Compared to a spiral-confined OC, such an unconfined HyFRC provides higher or comparable peak/residual rebar pull-out resistance and leads to a more significant slip stiffening behavior as revealed by the bond stress-slippage curves prior to reaching the peak bond stress.

The rebar pull-out tests provide local bond stress-rebar slippage relations which can be used to characterize the overall rebar/HPFRCC composite behavior that is essential for the mechanical response of a steel-rebar-reinforced HPFRCC structural member. Therefore, the local bond information indicates possible applications of new types of HPFRCC in practice and provides a guideline for developing building code for these materials. According to the rebar pull-out test results, the HyFRC can be applied to the structural member where superior rebar anchorage and bond resistance is required. Compared to transverse steel reinforcement, the fiber reinforcement in HyFRC especially improved the slip stiffening behavior of longitudinal steel rebar before the bond stress achieves the maximum bond resistance. Therefore, the HyFRC starts to provide significant rebar bond enhancement when relatively low load is applied to a structural member while the transverse steel reinforcement is not effective in improving rebar/matrix bond until a much higher load is applied. The results from rebar pull-out tests also indicate how the rebar bond resistance in HPFRCC is affected by the amount of transverse steel reinforcement, rebar size and c/d_b ratio, which are typical parameters used to evaluate bond strength and development length of rebar in the building code. The experimental investigation indicates that combining transverse steel confinement with HyFRC matrix can improve the bond performance considerably while transverse steel reinforcement induced minimal improvement for ECC. Such behavior indicates that the effect of transverse steel reinforcement in HyFRC and ECC needs to be treated differently in the building code.

In order to obtain superior rebar pull-out performances in HPFRCC matrices, the material not only requires to have significant hardening behavior but also needs coarser aggregates to ensure

higher interlocking/friction at rebar/matrix interface and higher crack resistance for matrix keys between rebar ribs. Based on the experiments performed in this study, the HyFRC matrix without fly ash exhibits higher pull-out resistance compared to the ECC specimens which does not incorporate coarse aggregates. Among different types of HyFRC under investigation, the HyFRC without fly ash exhibits a better performance compared to the HyFRC where 50% of cement was replaced by fly ash.

The confining effect from spiral in the HyFRC material was investigate by applying vibration tests and DIC techniques to the rebar pull-out test program. Vibration tests results indicate comparable matrix shearing and crushing degrees after pulling out the rebars from the unconfined and spiral-confined HyFRC matrix. The DIC measurements for rebar pull-out tests show that some relatively large crack openings developed in unconfined HyFRC which slightly decreased the normal compressive stress that grips the rebar. On the other hand, DIC measurement confirmed that the spiral in HyFRC not only provides additional rebar gripping stress but also prevents the relatively wide cracks from forming. The improvement of rebar pull-out resistance in confined HyFRC is due to the spiral providing additional crack closure stress across the splitting cracks. However, the increase in rebar pull-out resistance of HyFRC with spiral is not very pronounced compared to its unreinforced HyFRC counterpart because the relatively wide cracks in unconfined HyFRC are still too fine to weaken the rebar bond resistance significantly.

During rebar pull-out, spiral-confined HyFRC specimen had more uniform distribution of splitting crack widths compared to unconfined HyFRC. Such difference of crack width distribution in the top matrix surface and middle bond region were observed by DIC measurements and FEA results, respectively. The DIC measurements showed that using transverse steel reinforcement in HyFRC led to a much uniform crack width distribution. On the other hand, the FE model had a constraint for the relative displacement between rebar and matrix in circular direction and such constraint made the crack width distribution more uniform in the model of unconfined HyFRC. Therefore, the transverse steel reinforcement improved the uniformity of crack width distribution in a less significant manner in the FE model compared to the improvement observed from DIC measurements. According to the observation of the saw cut cross section from rebar pull-out specimens, spiral-confined HyFRC exhibited less splitting cracks in the middle bond region compared to unconfined HyFRC. However, the DIC measurements captured more cracks on the top surface of confined HyFRC specimen compared to the unconfined one. The different characteristics for crack amounts on different specimen heights is explained by a crack propagation process from the middle bond region to the top

specimen surface. The analysis results from the model indicated that more cracks in unconfined HyFRC may be too fine to propagate to the top specimen surface. Such mechanism reduced the amount of crack on the top surface of unconfined HyFRC more significantly and hence, affected the crack amount comparison results for top surfaces of unconfined and spiral-confined HyFRC specimens.

The multi-scale crack control mechanism and micro/macro fiber synergy in HyFRC lead to hardening behavior at relatively low fiber volume fraction, and are responsible for the superior rebar pull-out performance in such material. The micro/macro fiber synergy between same types of fibers used in the HyFRC is confirmed by the single fiber pull-out test program. The macrofiber pull-out performances are considerably improved by the PVA microfibers additions.

According to the fiber pull-out test results, replacing cement with high volume fly ash makes the PVA microfibers less effective in resisting macrofiber pull-out. Such mechanism decreases the ability of macrofibers to resist cracks induced by rebar slippage and therefore, during rebar pull-out tests, the HyFRC with high volume fly ash exhibited lower rebar pull-out resistance compared to HyFRC without fly ash. On the other hand, slag improves the macrofiber pull-out resistance by densifying the macrofiber/matrix interface. When the steel macrofiber was pulled out from UHPC matrix, almost no microcracks were induced by macrofiber slippage due to the extremely high matrix strength. In such UHPC, the steel microfibers didn't improve the macrofiber pull-out performance because the steel microfibers are only functional when sufficient microcracks exist.

For a material-based study, it is suggested that future research focuses on more different types of HyFRC in which cement is replaced by various amount/types of supplementary materials. The effects of supplementary materials on the mechanical behaviors for rebar/concrete interface, steel macrofiber/concrete interface and PVA microfiber/concrete interface need to be considered because the rebar pull-out behavior in HyFRC is dominant by friction/interlock at rebar/matrix interface, pull-out performance of macrofibers and effectiveness of microfibers. Rebar pull-out and fiber pull-out tests can be conducted to investigate if a more significant multi-scale pull-out behavior improvement is achieved by the new types of HyFRC. Full-scale structural member such as different types of beam, column and beam-column joints can also be tested to investigate the degree of structural response improvement induced by the enhanced rebar bond performance provided by HyFRC.

The fiber pull-out tests provide the relations between pull-out load and displacement of steel macrofibers in matrices with various compositions and microfiber types/contents. These relations indicate how crack bridging stress provided by a steel macrofiber is affected by matrix material types. Hence, such relations can be utilized to develop crack models with crack closure stress provided by fibers in various cementitious matrices. On a larger scale, these crack models can be extended to two-dimensional and three-dimensional models with various types of HyFRC matrices to simulate the behavior of splitting cracks induced by rebar slippage.

6   Reference

1.   Goto, Y. *Cracks formed in concrete around deformed tension bars*. in *ACI Journal Proceedings*. 1971. ACI.

2.   Mitchell, D., H.H. Abrishami, and S. Mindess, *The effect of steel fibers and epoxy-coated reinforcement on tension stiffening and cracking of reinforced concrete.* Materials Journal, 1996. **93**(1): p. 61-68.

3.   Abrishami, H.H. and D. Mitchell, *Influence of splitting cracks on tension stiffening.* ACI Structural Journal, 1996. **93**(6): p. 703-710.

4.   Abrishami, H.H. and D. Mitchell, *Influence of steel fibers on tension stiffening.* ACI structural journal, 1997. **94**(6): p. 769-775.

5.   Bischoff, P.H., *Tension stiffening and cracking of steel fiber-reinforced concrete.* Journal of materials in civil engineering, 2003. **15**(2): p. 174-182.

6.   Moreno, D.M., W. Trono, G. Jen, C. Ostertag, and S.L. Billington, *Tension stiffening in reinforced high performance fiber reinforced cement-based composites.* Cement and Concrete Composites, 2014. **50**: p. 36-46.

7.   Plizzari, G.A., M.A. Deldossi, and S. Massimo, *Transverse reinforcement effects on anchored deformed bars.* Magazine of Concrete Research, 1998. **50**(2): p. 161-177.

8.   Fang, C., K. Lundgren, L. Chen, and C. Zhu, *Corrosion influence on bond in reinforced concrete.* Cement and concrete research, 2004. **34**(11): p. 2159-2167.

9.   Ichinose, T., Y. Kanayama, Y. Inoue, and J. Bolander, *Size effect on bond strength of deformed bars.* Construction and building materials, 2004. **18**(7): p. 549-558.

10.   Eligehausen, R., E.P. Popov, and V.V. Bertero, *Local bond stress-slip relationships of deformed bars under generalized excitations*. Earthquake engineering research center Report. 83/23. University of California, Berkeley, 1983

11.   Xing, G., C. Zhou, T. Wu, and B. Liu, *Experimental study on bond behavior between plain reinforcing bars and concrete.* Advances in Materials Science and Engineering, 2015. **2015**.

12.   Lee, B. and M. Mulheron, *Fluctuation of bond stress–slip behaviour of deformed bar under displacement control.* Magazine of Concrete Research, 2012. **64**(10): p. 863-875.

13.   Lundgren, K., *Pull-out tests of steel-encased specimens subjected to reversed cyclic loading.* Materials and Structures, 2000. **33**(7): p. 450-456.

14.   Afefy, H.M. and E.-T.M. El-Tony, *Bond Behavior of Embedded Reinforcing Steel Bars for Varying Levels of Transversal Pressure.* Journal of Performance of Constructed Facilities, 2016. **30**(2): p. 04015023.

15. Leibovich, O., A. Dancygier, and D. Yankelevsky, *An Innovative Experimental Procedure to Study Local Rebar-Concrete Bond by Direct Observations and Measurements.* Experimental Mechanics, 2016. **56**(5): p. 673-682.

16. Wu, F., H.-L. Chan, and F.-K. Chang, *Ultrasonic guided wave active sensing for monitoring of split failures in reinforced concrete.* Structural Health Monitoring, 2015. **14**(5): p. 439-448.

17. Chen, H.-J., C.-H. Huang, and Z.-Y. Kao, *Experimental investigation on steel-concrete bond in lightweight and normal weight concrete.* Structural Engineering and Mechanics, 2004. **17**(2): p. 141-152.

18. Lin, H., Y. Zhao, J. Ožbolt, and R. Hans-Wolf, *The bond behavior between concrete and corroded steel bar under repeated loading.* Engineering Structures, 2017. **140**: p. 390-405.

19. Zhao, J., G. Cai, and J. Yang, *Bond-slip behavior and embedment length of reinforcement in high volume fly ash concrete.* Materials and Structures, 2016. **49**(6): p. 2065-2082.

20. Torre-Casanova, A., L. Jason, L. Davenne, and X. Pinelli, *Confinement effects on the steel–concrete bond strength and pull-out failure.* Engineering Fracture Mechanics, 2013. **97**: p. 92-104.

21. Lowell Yerex, I., T.H. Wenzel, and R. Davies. *Bond Strength of Mild Steel in Polypropylene Fiber Reinforced Concrete*. in *ACI Journal Proceedings*. 1985. ACI.

22. Rostásy, F.S. and K. Hartwich, *Bond of deformed reinforcing bar embedded in steel fibre reinforced concrete.* International Journal of Cement Composites and Lightweight Concrete, 1988. **10**(3): p. 151-158.

23. Ezeldin, A. and P. Balaguru, *Bond behavior of normal and high-strength fiber reinforced concrete.* ACI Materials Journal, 1989. **86**(5).

24. Ganesan, N., P. Indira, and M. Sabeena, *Bond stress slip response of bars embedded in hybrid fibre reinforced high performance concrete.* Construction and Building Materials, 2014. **50**: p. 108-115.

25. Krstulovic-Opara, N., K.A. Watson, and J.M. LaFave, *Effect of increased tensile strength and toughness on reinforcing-bar bond behavior.* Cement and Concrete Composites, 1994. **16**(2): p. 129-141.

26. Siva, H. and E.N. Antoine, *Bond Stress-Slip Response of Reinforcing Bars Embedded in FRC Matrices under Monotonic and Cyclic Loading.* ACI Structural Journal, 1997. **94**(5): p. 525-536.

27. Shih-Ho Chao, A.E.N. and J.P.-M. Gustavo, *Bond Behavior of Reinforcing Bars in Tensile Strain-Hardening Fiber-Reinforced Cement Composites.* ACI Structural Journal, 2009. **106**(06): p. 897-906.

28.   Chao, S.-H., *Bond Characterization of Reinforcing Bars and Prestressing Strands in High Performance Fiber Reinforced Cementitious Composites under Monotonic and Cyclic Loading*, PhD dissertation. University of Michigan, Ann Arbor. 2005

29.   Asano, K. and T. Kanakubo, *Study on size effect in bond splitting behavior of ECC.* High Performance Fiber Reinforced Cement Composites 6, 2012: p. 137-144.

30.   Huang, L., Y. Chi, L. Xu, P. Chen, and A. Zhang, *Local bond performance of rebar embedded in steel-polypropylene hybrid fiber reinforced concrete under monotonic and cyclic loading.* Construction and Building Materials, 2016. **103**: p. 77-92.

31.   Saleem, M.A., A. Mirmiran, J. Xia, and K. Mackie, *Development length of high-strength steel rebar in ultrahigh performance concrete.* Journal of Materials in Civil Engineering, 2013. **25**(8): p. 991-998.

32.   Jansson, A., I. Löfgren, K. Lundgren, and K. Gylltoft, *Bond of reinforcement in self-compacting steel-fibre-reinforced concrete.* Magazine of Concrete Research, 2012. **64**(7): p. 617-630.

33.   Markovich, I., J. Van Mier, and J. Walraven, *Single fiber pullout from hybrid fiber reinforced concrete.* HERON, 2001. **46**: p. 191-200.

34.   Cunha, V.M., J.A. Barros, and J.M. Sena-Cruz, *Pullout behavior of steel fibers in self-compacting concrete.* Journal of Materials in Civil Engineering, 2009. **22**(1): p. 1-9.

35.   Abu-Lebdeh, T., S. Hamoush, and B. Zornig, *Rate effect on pullout behavior of steel fibers embedded in very-high strength concrete.* American Journal of Engineering and Applied Sciences, 2010. **3**(2): p. 454-463.

36.   Abdallah, S., M. Fan, and X. Zhou, *Pull-Out Behaviour of Hooked End Steel Fibres Embedded in Ultra-high Performance Mortar with Various W/B Ratios.* International Journal of Concrete Structures and Materials, 2017: p. 1-13.

37.   Mehta, P.K. and P.J.M. Monteiro, *Concrete: microstructure, properties, and materials*. 3 ed. 2006: McGraw-Hill, New York.

38.   Blunt, J.D. and C. Ostertag, *Deflection Hardening and Workability of Hybrid Fiber Composites.* ACI Materials Journal, 2009. **106**(3): p. 265-272.

39.   Naaman, A. and H. Reinhardt, *Proposed classification of HPFRC composites based on their tensile response.* Materials and structures, 2006. **39**(5): p. 547-555.

40.   Lin, A. and C.P. Ostertag, *Multi-scale Pull-Out Resistance of Steel Reinforcing Bar embedded in Hybrid Fiber Reinforced Concrete (HyFRC)*, in *Fibre Concrete 2017*. 2017: Prague, Czech Republic.

41.   Tepfers, R., *Cracking of concrete cover along anchored deformed reinforcing bars.* Magazine of concrete research, 1979. **31**(106): p. 3-12.

42. Söylev, T., *The effect of fibers on the variation of bond between steel reinforcement and concrete with casting position.* Construction and Building Materials, 2011. **25**(4): p. 1736-1746.

43. Gambarova, P.G. and G. Rosati, *Bond and splitting in reinforced concrete: test results on bar pull-out.* Materials and Structures, 1996. **29**(5): p. 267-276.

44. Pan, B., K. Qian, H. Xie, and A. Asundi, *Two-dimensional digital image correlation for in-plane displacement and strain measurement: a review.* Measurement science and technology, 2009. **20**(6): p. 1-17.

45. Ouglova, A., Y. Berthaud, F. Foct, M. François, F. Ragueneau, and I. Petre-Lazar, *The influence of corrosion on bond properties between concrete and reinforcement in concrete structures.* Materials and Structures, 2008. **41**(5): p. 969-980.

46. Jansson, A., M. Flansbjer, I. Löfgren, K. Lundgren, and K. Gylltoft, *Experimental investigation of surface crack initiation, propagation and tension stiffening in self-compacting steel–fibre-reinforced concrete.* Materials and structures, 2012. **45**(8): p. 1127-1143.

47. Lárusson, L.H. and G. Fischer. *Bond slip and crack development in FRC and regular concrete specimens longitudinally reinforced with FRP or steel under tension loading.* in *Bond In Concrete 2012.* 2012.

48. Godfrey, D.E. and N.R. Kuchar, *Method of testing the integrity of installed rock bolts.* 1977, United States Patent.

49. Ivanović, A. and R.D. Neilson, *Modelling of debonding along the fixed anchor length.* International Journal of Rock Mechanics and Mining Sciences, 2008. **46**(4): p. 699-707.

50. Ivanovic, A., R. Neilson, and A. Rodger, *Lumped parameter modelling of single-tendon ground anchorage systems.* Proceedings of the ICE-Geotechnical Engineering, 2001. **149**(2): p. 103-113.

51. Milne, G.D., *Condition monitoring & integrity assessment of rock anchorages*, PhD Thesis. University of Aberdeen (United Kingdom). 1999

52. Lowes, L.N., J.P. Moehle, and S. Govindjee, *Concrete-steel bond model for use in finite element modeling of reinforced concrete structures.* Structural Journal, 2004. **101**(4): p. 501-511.

53. Pepe, M., H. Mazaheripour, J. Barros, J. Sena-Cruz, and E. Martinelli, *Numerical calibration of bond law for GFRP bars embedded in steel fibre-reinforced self-compacting concrete.* Composites Part B: Engineering, 2013. **50**: p. 403-412.

54. Ožbolt, J., S. Lettow, and I. Kožar, *Discrete bond element for 3D finite element analysis of reinforced concrete structures.* 2002, Proceedings of the 3rd International Symposium:

Bond in Concrete-from research to standards. Budapest: University of Technology and Economics. p. 1-11.

55.   Lettow, S., J. Ožbolt, R. Eligehausen, and U. Mayer, *Bond of RC members using nonlinear 3D FE analysis.* Fracture mechanics of concrete structures. IA-FraMCoS, 2004: p. 861-868.

56.   Ožbolt, J., Y. Li, and I. Kožar, *Microplane model for concrete with relaxed kinematic constraint.* International Journal of Solids and Structures, 2001. **38**(16): p. 2683-2711.

57.   Lundgren, K. and K. Gylltoft, *A model for the bond between concrete and reinforcement.* Magazine of Concrete Research, 2000. **52**(1): p. 53-63.

58.   Lundgren, K., *Bond between ribbed bars and concrete. Part 1: Modified model.* Magazine of Concrete Research, 2005. **57**(7): p. 371-382.

59.   Lura, P., G. Plizzari, and P. Riva, *3D finite-element modelling of splitting crack propagation.* Magazine of Concrete Research, 2002. **54**(6): p. 481-494.

60.   Kayali, O., *Effect of high volume fly ash on mechanical properties of fiber reinforced concrete.* Materials and Structures, 2004. **37**(5): p. 318-327.

61.   Li, V.C., *On engineered cementitious composites (ECC).* Journal of advanced concrete technology, 2003. **1**(3): p. 215-230.

62.   Moreno, D., W. Trono, G. Jen, C. Ostertag, and S. Billington, *Tension-stiffening in reinforced high performance fiber-reinforced cement-based composites under direct tension*, in *High Performance Fiber Reinforced Cement Composites 6*. 2012, Springer. p. 263-270.

63.   Wang, S. and V.C. Li, *Engineered cementitious composites with high-volume fly ash.* ACI Materials Journal, 2007. **104**(3).

64.   Bandelt, M.J. and S.L. Billington, *Bond behavior of steel reinforcement in high-performance fiber-reinforced cementitious composite flexural members.* Materials and Structures, 2014: p. 1-16.

65.   Hossain, K., K. Sennah, and A. Hamoda, *Bond Strength of Ribbed GFRP Bars Embedded in High Performance Fiber Reinforced Concrete.* Journal of Multidisciplinary Engineering Science and Technology (JMEST), 2015. **2**(6).

66.   Barthes, C. 2014, http://www.optecal.com/.

67.   Aghdasi, P., A.E. Heid, and S.-H. Chao, *Developing Ultra-High-Performance Fiber-Reinforced Concrete for Large-Scale Structural Applications.* ACI Materials Journal, 2016. **113**(5).

68.   Habel, K., E. Denarié, and E. Brühwiler, *Time dependent behavior of elements combining ultra-high performance fiber reinforced concretes (UHPFRC) and reinforced concrete.* Materials and structures, 2006. **39**(5): p. 557-569.

69. *DIANA-Finite Element Analysis: User's Manual release 10.0*. 2016, TNO DIANA, Delft, Netherlands.

70. Blunt, J.D., *The effect of fiber reinforcement on the corrosion controlled degradation of reinforced concrete flexure elements*, PhD dissertation. University of California, Berkeley. 2008